JOURNAL OF AEROSPACE TECHNOLOGY AND MANAGEMENT

ENRICHED PUBLICATIONS PVT. LTD

Journal of Aerospace Technology and Management

Aims and Scope

The Journal of Aerospace Technology and Management (JATM) is an open-access journal devoted to research and management on different aspects of aerospace technologies.

For all accepted manuscripts, the correspondence author will be asked to contribute with the Article Processing Charge, which will be applied to editorial services that support the publishing process, like editing, proofreading, indexing and dissemination.

The value is fixed per article, independent of its length and is R$ 800,00 (in Brazilian reais) or U$300,00 (in American dollars). In exceptional cases, the editorial board may waive a contribution upon reasonable request.

JATM accepts manuscripts already published in preprint, considered reliable by the editorial committee, and must be informed in the Open Science Compliance Form that must be submitted as a supplementary file to the Manuscript.

Journal of Aerospace Technology and Management

EDITORS IN CHIEF

Antônio F. Bertachini	**Elizabeth da Costa Mattos**
Instituto Nacional de Pesquisas Espaciais - INPE, São José dos Campos/SP, Brazil	Instituto de Aeronáutica e Espaço - IAE, São José dos Campos/SP, Brazil

Journal of Aerospace Technology and Management

Contents

The Wind Environment Interactions Relative to Launch Vehicle Design

Dale L. Johnson1, William W. Vaughan2,*

A B S T R A C T

Since atmospheric winds play the most critical natural enviroment (NE) role as input into the design and development of an aerospace launch vehicle, this paper provides a more detailed description of the wind environment and its interaction with engineering design in launch and space vehicle development applications at Kennedy Space Center (KSC).

KEYWORDS: Terrestrial Environment, Wind Characteristics, Ground Winds, Winds Aloft, Vehicle Design.

INTRODUCTION

This is the third historical paper which concludes what the previous two papers (Johnson and Vaughan, 2019 and Johnson and Vaughan, 2020) presented, dealing with the subject of the role of the Earth's terrestrial and space natural environment involvement in launch vehicle design and development.

The response of a launch vehicle to wind disturbances is very complicated because the vehicle's response depends on and interacts with the characteristics of the wind-magnitude, shear, gust, etc., the vehicle dynamics (rigid body, elastic body, propellant oscillations, etc.), and the control system.

The determination of a launch vehicle's response to atmospheric disturbances cannot be reduced to the analysis of one discrete set of response criteria, such as vehicle loads, but must include many response parameters dependent upon the vehicle configuration and specific mission. It is not practical to use only one type of NE design criteria input for all phases of vehicle design. Different approaches and methods of evaluation must be used as the particular phase demands. The phases include preliminary design, final structural design, guidance and control (G&C) system design and optimization – preliminary and final, and establishment of limits (constraints) and procedures for launch and flight operations.

Vehicle design phases interact, as well as launch and flight operations. In each phase, the following must be considered. The choice of the methods for NE analysis and the choice of an analytical dynamic model to describe the vehicle characteristics relevant to a particular design phase must be determined. For example, a rigid body analysis may be adequate for preliminary structural design, and full elastic simulation (generating loads envelopes) could be used for the final design. Likewise, the Vector Wind Profile (VWP) model or a discrete synthetic wind profile may be adequate for preliminary design, while final design and flight operations capability may require individual detailed Jimsphere measured winds. Johnson (2008) provides an extensive overview of the different NE design criteria guidelines for use in aerospace vehicle development.

The main perturbing forces for launch vehicles, both on the launch pad and in flight, are the aerodynamic loads produced by winds. Because the wind loads are a major structural consideration, they greatly influence the design of the vehicle's flight control system. Since wind is the most important atmospheric parameter influencing the design of a launch vehicle, wind as input has been selected here as an example to illustrate the importance of the terrestrial environment considerations in the launch vehicle design and development process.

GROUND WINDS

Ground or surface winds are generally defined here as < 150 m. In-flight (or aloft) winds are from 150 to ~80 km altitude. A launch vehicle exposed to surface winds for more than a few hours while erected on the launch pad may be subjected to critical wind loads, elevating the risk for vehicle damage as exposure time increases. Since wind is a vector quantity that varies both in space and time, the wind loads should be considered as a dynamic input to the vehicle structure. From an aerodynamic point of view, the problem falls in the category of viscous separated flow around a bluff body. Although such flows have been studied for years, an adequate approximation to aerodynamic transfer functions to relate the dynamic wind vector to the dynamic load on the body does not exist. Therefore, quasi-steady assumptions must be used. To further simplify the problem, the near-surface wind profile is broken down into steady-state (mean) and unsteady components (Fig. 1), with resulting static and dynamic loads
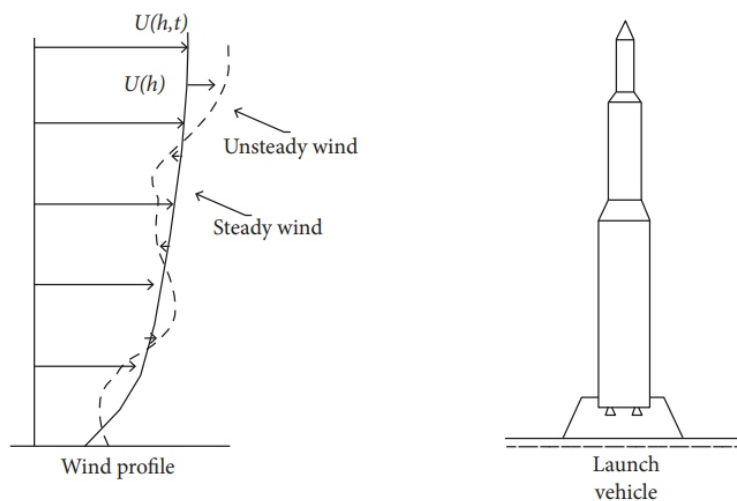
Figure 1. Launch vehicle exposed to steady state (mean) and unsteady component for ground winds (Geissler, 1970).

superposed (Geissler 1970). The second-order loads resulting from the interaction of the static and dynamic wind components can be neglected in the present state of the art.

Low-Level Wind Profile. Since the Earth's surface exerts a frictional force on the lower layers of the atmosphere, this causes a decrease in the average wind speeds near the surface. Assuming that stress is

proportional to the vertical wind shear, and that the proportionality constant varies linearly with height, the steady-state wind speed profile may be represented by a logarithmic function of height. This representation turns out to be approximately valid during neutral to slightly unstable stability conditions, which usually include high wind speeds. An empirical representation of this function (Eq. 1) that has been widely used in scientific and engineering work, is called the power law:

$$U = U_1 \, (h/h_1)^p \tag{1}$$

where U = wind speed at height h; U1 = wind speed at a reference height h1; exponent p = function of wind speed, ground roughness, stability, etc., and increases as the wind speed decreases.

Once p is known, the wind speed needs only to be measured at the reference height to define the entire profile envelope to a height of ~150 m. For purposes of establishing design envelopes, especially for the moderate ground roughness conditions that exist for KSC, a value for p of 0.20 is usually employed when the 3-m height, steady-state wind speed is between 7 and 15 m/s. A KSC p value of 0.14 has been used when the steady-state wind speed is between 22 and 30 m/s. Therefore, using the power law profile, wind measurements at any height may be translated to any other height. See Johnson (2008) and Smith and Adelfang (1998) for application.

Wind Shear. Structural loading exists on the vehicle while it is anchored on the launch pad. A symmetric vehicle behaves as a cantilevered beam with wind pressures producing bending moments that increase continuously from zero at the vehicle's nose to a maximum at the base as do the vehicle's axial dead weight loads.

Wind shear near the surface, for design purposes, is a shear that acts on a launch vehicle free standing on the pad or at the time of lift-off. This design wind shear was initially computed from the selected design percentile wind speed envelope by using the peak wind speed at the top of the vehicle and the quasi-steady-state wind speed at the base of the vehicle with respect to height of the base above the true ground. In some cases, the base of the vehicle will be elevated above the ground, which must be taken into account.

Gust. For design purposes, the discrete gust shape for the higher surface wind conditions and in-flight wind conditions is represented by a wedge shape, with linear increase to the peak wind in 2 s and then linear decay to the steady-state value in 1 s. The gust factor is known to be a function of the steady-state wind speed, time average of the wind speed, stability conditions, terrain features, and height. A gust factor of 1.4 has been used at KSC to obtain the design peak wind speed.

Turbulence Spectra. The spectra of the lateral, longitudinal, and vertical wind velocity components are, in general, different, and a function of stability and local terrain features. For most engineering applications, it appears desirable to compute the spectra of turbulence for the specific location of interest. See Power Spectral section for a more thorough description.

Wind Loads Rules of Thumb. A customary practice during the preliminary design phase of a vehicle is

to estimate the steady drag bending moment corresponding to the expected peak wind, allowing a 50% margin for dynamic loads. This estimate can be un-conservative for some vehicle configurations. The static and dynamic loads are then finalized by testing an aeroelastic model in the wind tunnel after the structural design of the vehicle is nearly finalized. Wind azimuth is also a primary input variable, especially for a nonsymmetrical vehicle like the Space Shuttle.

Unsteady drag and lift resulting from a steady wind can be attributed to three sources: (1) Vortex shedding, (2) buffeting, and (3) galloping excitation. Power spectral concepts have been used to describe the fluctuating wake velocities and pressures and the forces on a bluff body.

Static and dynamic loads due to winds can be combined vectorially to obtain the final load, and is believed to provide a conservative estimate. Since most of these loads can be determined to some extent in the design phase, the structural integrity of the vehicle will be, in general, jeopardized only by unexpectedly large vortex shedding loads. In this case, a study should be made of launch pad operations to determine the timeframe of vehicle exposure and the associated risk of structural damage, or launch delay. Extended exposure to the wind field of the unprotected vehicle should be avoided and the risk associated with any proposed on-pad stay time schedule should be established. This risk includes not only structural damage but also the possibility of schedule slip or failure to obtain a desired launch date or time. This entire ground wind loads problem and solution is discussed in chapter 3 of Geissler (1970).

A damper connecting the vehicle to the umbilical tower generally reduces the vortex shedding loads along with the dynamic loads caused by atmospheric turbulence, but does not reduce the effect from steady-state winds. Therefore, the risk of wind damage to the vehicle can be significantly decreased for a reasonable on-pad exposure time, e.g., to < 1% for Saturn-type symmetrical vehicle configuration, for a pad stay time of 30 days.

Vortex Shedding/Stop Sign Flutter for Symmetric and Nonsymmetric Launch Vehicles. A symmetrical launch vehicle has been analyzed for classical vortex shedding using both analytical and scale model testing. Being essentially a cylinder, the vehicle showed clear vortex shedding problems, particularly since it must spend up to 30 days on the pad exposed to ground winds. As a result, wind velocity criterion was then used which required installation of a damper when above critical wind levels were being predicted, or during any free-standing time on the pad. Bending moment capability is a function of maximum ground wind speed. Pearson et al. (1996) present these bending effects versus wind speed.

A nonsymmetrical launch vehicle configuration may not be susceptible to classical vortex shedding, but falls into the arena of the classical stop sign flutter (named from road signs fluttering at certain critical frequency wind speeds). Scale model wind tunnel tests are usually needed to verify the stop sign flutter potential. The flutter limit may be determined relative to the pad vehicle interface stiffness. Final design may show no stop sign flutter problem due to the naturally large torsional stiffness arising from the

vehicle configuration and the hold-down/supports.

Lift-Off Aerodynamics: Vehicle Drift/Twang Loading. Wind has a significant effect on the launch vehicle during the period from just before release of the hold-down mechanism until the vehicle has completely cleared the launch tower structure. The major wind problem during launch is that of vehicle drift just after release and during initial ascent. It is assumed for these analyses that the vehicle at lift-off is in an undeflected state such that its initial motion is vertical. Under these conditions, bending moments induced on the vehicle are smaller than those experienced at later flight times, or in the hold-down position before launch, when ground winds may surpass the allowable values for launching. Very large forces and moments can be induced in the vehicle if it collides with the tower or vehicle hold-down mechanism. Nonuniform wind velocity profiles exist over the vehicle length before and at lift-off. After clearing the towers, a more uniform cross-flow velocity and angle-of-attack distribution exist.

A related phenomenon at lift-off that needs to be considered, commonly called twang loading, is an effect (force) on the vehicle caused when the vehicle base is released to the free mode. A wind-loaded, bent vehicle will tend to snap straight at the instant of release. Although longitudinal shock loading on the vehicle from the release of the hold-down mechanism is important, it is essentially independent of wind conditions.

IN-FLIGHT WINDS

As stated earlier, in-flight (or aloft) winds are normally defined as occurring and being applied from 150 m to ~80 km altitude. Winds and wind load effects on an airframe structure, on vehicle G&C, etc. are needed for launch vehicle flight capability design and operability. Mission analysis simulations, wind models, wind profiles, and power spectral analyses can be used to simulate wind flow, wind shear, gust, and turbulent effects on a vehicle in flight, while wind monitoring and load relief systems can help alleviate various wind-associated engineering problems in flight. These areas are discussed within this subsection.

Structural/Airframe Design. Wind-induced forces and bending moments are the basis for the design of the vehicle (structure), since there is a large impact of the wind effects upon vehicle configuration design. Rigid body flight loading accounts for the gross overall motions of the vehicle as it responds to wind forces during flight. The vehicle can rotate, translate, and depending on the G&C scheme philosophies, may allow it to drift, to turn into the wind, or maintain the original trajectory. Since the choice of control philosophy is so important in determining the loads on the vehicle, rigid body analyses should be performed early in preliminary design before vehicle flexibility is introduced. However, structural loading due to ground winds before and during lift-off is also important. Analyses of elastic body motions of the vehicle, and that of propellant sloshing, are important in the final configuration, especially for propellant tank locations and airframe.

Wind Load Effects on Structure. Upper-level winds in the high dynamic pressure (max-q) region, typically between 10 and 15 km altitude, is the most significant terrestrial environment element affecting structural design. In-flight elastic body deformations whose magnitudes and resultant bending moments are strongly dependent on the relative frequencies of wind gusts and turbulence, as well as on the modes of body bending, propellant slosh, control, and engine. Vehicle system stability depends on the spacing of these influences and modal frequencies.

The total elastic response of the vehicle to in-flight winds is generally considered in terms of the three main bending moments. Moments due to angle of attack are direct wind load moments. The others are those due to engine-deflected thrust (as the control system gimbals the engines in response to the rigid body motions of the vehicle), and those due to those induced by the dynamic elastic response of the vehicle airframe and the sloshing of propellants. The response of the vehicle to distributed and randomly varying wind forces, as well as engine forces, is much more complex in terms of vehicle response characteristics.

During flight, the maximum bending moment and lateral shear load resulting from wind effects occur shortly after launch. The maximum bending moment, combined with the associated axial compression loads, constitutes the critical design condition (critical loading at max $q\alpha$). Beyond this altitude, the wind effects diminish.

Guidance and Control Systems. The G&C systems of a launch vehicle act together to cause the vehicle to fly a desired flight path, with each system having its own particular requirements. The guidance system determines the flight path to achieve desired end conditions, whereas the control system is to enforce the correct attitude of the vehicle in order to achieve the desired flight path. The guidance system must also correct for anomalies in the vehicle and in its environment, such as variations in air density and disturbances such as winds. The control system is to provide correction for anomalies and disturbances that affect the control system operation. Anomalies include variations in predicted structural bending characteristics, while the major disturbances are thrust misalignments and wind, with wind being by far the more significant of the two.

Wind Effects on Guidance System. The ascent wind profile effects come into play when the guidance system attempts to meet the objective of maximizing payload. There are two ways to accomplish this. One is the flight-mechanical effect of optimizing the lift-drag-direction relationship for a trajectory through the Earth's atmosphere and gravitational field. The second factor on which the wind has a direct influence is the effect of flight path on vehicle bending moment, and hence on structural weight. Bending moment is caused by control forces, i.e., engine gimbaling, and by aerodynamic side forces induced by side winds and vehicle maneuvering. Therefore, in choosing the optimal flight path, the guidance system must consider not only the flight mechanical aspects, but also the wind-induced bending moments.

While the vehicle is within the sensible atmosphere, the bending moment considerations are much more significant than the other flight mechanical effects. Vehicle guidance can be accomplished by a zero-lift tilt program, which commands the control system in attaining a zero-lift trajectory.

Since there is a large variation in probable wind magnitude and azimuth from month to month, it has been common practice to assume that the expected wind is zero (zero mean for launches throughout the year) in order to minimize the bending moment. This assumes that the tilt program assumes no wind disturbances and the guidance system output commands a trajectory that will produce zero side force if the nominal wind is actually encountered. If the actual wind encountered is equal to the nominal wind, and if the control force exerted is negligible, the zero-lift trajectory is the minimum bending moment trajectory. But if the launch is narrowed to one or two months, then the mean wind may be nonzero. Then it may be advisable to incorporate the mean wind information as a bias in the tilt program.

The biased tilt program will then ensure that a zero-lift trajectory is flown if the nominal wind is encountered. This procedure is called wind biasing. Many vehicle guidance systems today have gotten away from using monthly mean wind profiles as input, but currently use the real-time measured wind profile as input into their tilt programs. This allows for a wind bias of a much shorter time period than a month, thereby reducing the region of uncertainty about the nominal wind, and reducing the possible bending moment values for the vehicle. This would hold true if wind persistence prevailed throughout the countdown. The winds also have an influence through its effect on the terminal trajectory dispersion of first-stage flight for a multi-staged vehicle. Today, many launch vehicle guidance systems use a real-time, measured wind profile within its guidance algorithms for its commands. An example is the DOLILU (day of launch ILOAD update) used for the Space Shuttle.

Wind Effects on Control System. Upper-level winds in the high dynamic pressure (max-q) region, typically between 10 and 15 km altitude, is the most significant terrestrial environment element affecting control system design. Since the control system functions primarily to maintain a prescribed flight path as generated by guidance on preprogrammed attitude tilt commands, both off-nominal values of vehicle parameters and the presence of winds will cause the flight path to differ from that anticipated by the guidance system. Ideally, the control system should minimize this difference. However, there is a cost incurred in attempting to respond precisely to the guidance commands. The cost appears in terms of bending moments and resulting structural loading on the vehicle plus drift, and later thermal loads when the vehicle corrects for flight path deviations. The fact that winds are acting on the vehicle could make this cost excessive.

Winds aloft are frequently of such a large magnitude, especially in the max-q region, that large dispersions in guidance system prescribed attitude and flight path angles occur. In order for the control system to decrease these dispersions, large bending moments are imposed on the vehicle. If a controller is being designed for an already designed vehicle structure, these loads can be so large that the vehicle

If a controller is being designed for an already designed vehicle structure, these loads can be so large that the vehicle would exceed its design loads and break up.

On the other hand, if the control system design is for a vehicle in the preliminary design stage so that structural requirements are yet to be established, the large bending loads can result in excessively complex, heavy, or expensive structural configurations. Consequently, because of the in-flight winds, bending moments on the vehicle become the overriding consideration in controller design. Structural bending (involving winds) affects the control system's roles in two ways – through both forward loop and feedback loop coupling.

• Control Frequency. A factor affecting the control frequency is vehicle bending moment. High frequencies cause the control system to react fast to wind disturbances, resulting in large gimbal angles. Also, low frequencies produce a more sluggish gimbal response, thereby permitting larger values of angle of attack when a wind is encountered. The best frequency depends on the relative contributions of aerodynamic and thrust forces to vehicle bending moment. Thus, whether aerodynamic or thrust forces dominate, the bending moment depends upon an additional factor, the characteristic of the wind disturbance. Winds with high shear and gust content usually cause large transients in the control loop, and consequently large gimbal angles. On the other hand, winds low in shear and gust content cause a slow buildup in angle of attack and usually bring small gimbal angle requirements.

• Wind Models Used for Control Studies. Since winds are a dominant factor in system design, what wind models should be used in designing an acceptable control system? Several wind models are available and the particular one chosen depends on several factors, including the particular design philosophy. Should the system be designed for a low probability of failure due to winds, or a greater risk of failure be accepted? A second but important factor is the particular phase of the launch vehicle design problem under consideration. The first phase usually uses simplified mathematical models of the physical system being studied, while subsequent phases use models with increasing detail and accuracy. With the reference attitude being vertically upward in yaw-plane motion, the wind (U) is assumed to act transverse to the pitch plane. Initially, the way of representing the wind for use in control system design studies has been by using the synthetic wind profile (wind speed and wind shear values) as a function of altitude for different probability levels. Currently, the VWP model is frequently employed (Smith and Adelfang 1998; Adelfang et al. 1994; Smith 1976; Adelfang 1999).

• Wind gust/turbulence. Wind gust data used in control system design offers simplified rectangular-, triangular-, or sinusoidal-shaped gusts, since a good statistical representation of the fine structure of the wind is lacking. However, control design analysis also uses simplified representations for gusts, such as altitude duration, wavelength, versus amplitude of gust for different probability levels. For the Saturn example, in using vehicle trajectory data relating altitude to time, histories of the wind can be constructed from the wind profile and shear values given, resulting in a synthetic wind speed versus time

profile.

• Rule of thumb. A rectangular gust shape can then be superimposed at the time of peak wind speed, thereby producing a synthetic wind profile used in control design that combines the largest shear values with the highest gust at the point of peak wind speed. Since a design based on such a wind is very conservative, shear and gust values have been reduced by a percentage (15% in the Saturn case) based on engineering judgment since the largest shears and largest gusts are not likely to occur at the same time or altitude (Fig. 2). A less conservative approach can use a lower probability level wind speed and wind shear curves. Stochastic models of the wind have also been used in synthesizing control systems, and for analyzing the performance of an already designed system. Of course, as a less conservative design approach is employed, the risk for launch delay due to adverse wind effects in the maximum dynamic pressure (max-q) region increases. See section Description of Wind Shear, Gust, and Turbulence Models for further discussion on applications of turbulence and gusts to launch vehicles.

• Wind Examples and Risk:

• Shuttle. The solid rocket boosters (SRBs) on a nonsymmetrical Shuttle launch vehicle configuration initially had no control capability. As a result, the solid rocket motor nozzle flex bearing was redesigned and baselined. Two factors were used very early in the design and development period to take out conservatism, save weight and cost, and improve performance. They were as follows: (1) monthly mean wind biasing was instituted as part of criteria change for generating environments and performance, etc.; and (2) prior programs used the worst month reference period 95% wind speed in conjunction with the 99% wind shear and 99% gust as a conditional probability approach. The new launch vehicle configuration used 95% wind speed in combination with one-half the shear and gust 99% levels, then root sum squaring the other half with the other vehicle response parameters, again reducing margins.
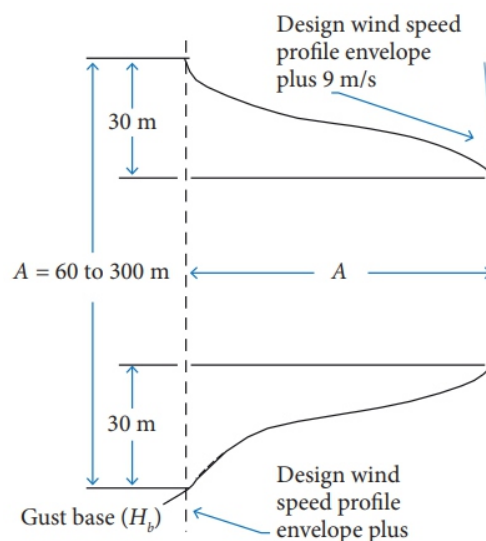
In addition, prelaunch monitoring of the ascent wind loads provided added assurance of a safe transition through the max-q region relative to wind loads. However, what these actions did was take out margins for flexibility, operations, and unknown vehicle effects.

• Worst wind. For linear control systems, the worst month reference period wind used in deter- mining loads for structure design is the wind which causes the vehicle to experience maximum structural loading. For linear control systems, design experience has led to the selection of wind values such as 95% wind speed and 99% wind shear and gusts in constructing a synthetic wind profile that serves as the design worst month reference period wind. When nonlinear feedback systems are employed, such as load relief, winds must still satisfy the statistical stated constraints, but the wind profile constructed using extreme values will not necessarily be the worst wind. Techniques are needed to help determine what the worst disturbance will be for any particular control law. Today, this synthetic wind profile method has been supplemented in most analyses with the MSFC VWP model (Smith and Adelfang 1998; Adelfang et al. 1994; Smith 1976; Adelfang 1999).

• Stochastic methods. The use of a synthetic, deterministic wind profile as a design wind estimates a given probability level of wind disturbance, which may not precisely represent the desired percentile wind that results in applying a conservative and more robust design approach in defining uncertainties in wind effects. But if the wind could be treated as a statistical quantity, one can design to the desired probability level, if the vehicle model and wind model are both sufficiently restricted. The wind assumption is that the wind can be described as a Gaussian, time-varying random process with known characteristics. The two drawbacks in control system design are that the wind may not be Gaussian and the wind statistics need to consist of a sufficient quantity of accurately measured wind data.

• Wind monitoring:

• Day of launch. Launch vehicles are designed to accommodate a high percentage of occurrences of in-flight winds, minimizing the risk for launch delay. But there still is a finite possibility of winds occurring that will exceed the structural or control capability of the vehicle. Therefore, winds aloft can be closely monitored during the last 6 to 12 h before launch in order to minimize the risk involved at launch. Concerted efforts towards adequate design of airframe and control system should be made to reduce such risks. The limited launch windows for some launch vehicle missions illustrate this need.

• Test and operational. Knowledge of the terrestrial environment is also necessary for establishing launch vehicle test requirements, and is used in the design of associated support equipment. Such data are required to define the fabrication, storage, transportation, test, and preflight design conditions and should be considered for both the whole system and the components which make up the system. For vehicle test and operations, areas of the terrestrial environment that need to be more carefully monitored prior to and during these events will benefit from the assessment of the terrestrial environment within the early design stages of the new launch vehicle development program.

• Advanced Load Relief Systems. Advanced control methods for load relief can also reduce vehicle bending moment. Since bending moment depends on the form and magnitude of the wind disturbance, it is reasonable to consider advanced load relief systems that adapt to changes in disturbance force (input adaptive systems). Input adaptation to wind may be thought of as a general extension of the concept of wind biasing used for the guidance system. It attempts to compensate for the actual wind disturbances as they are encountered. The problems in designing such a system are sensing the wind value and determining what action to take in adjusting the control law for the measured wind value. Although the maximum bending moment within the class of winds considered can be reduced by the switched integral controller, there can still be an undesirable sensitivity to the wind magnitude. Wind shear reversal in the maximum dynamic region is an issue for adaptive control systems.

In the pre-Saturn and early Saturn days, for wind load alleviation, launch vehicles used adjustment of first-stage guidance in the pitch-plane relative to the monthly mean pitch-plane wind. During later Skylab and Apollo launches, adjustment of the guidance in both the pitch and yaw planes relative to the monthly mean pitch and yaw plane wind components were used to achieve additional wind loads relief. During Shuttle, further reductions were accomplished by selecting launch guidance from trajectory runs which produced the minimum loads using a day of launch (DOL) measured wind profile.

More recently, Shuttle first-stage guidance is derived based on analysis of a trajectory simulation using a measured Jimsphere wind profile obtained at T-4.5 h. This produces the smallest ascent loads dispersions achieved to date. It is called day-of-launch ILOAD update or DOLILU, where ILOAD represents ascent guidance. When DOLILU is used, it is the wind profile perturbations of approximately < 6,000-m wavelength that force control system responses to maintain the guidance path. Therefore, even the largest wavelengths in a wind profile could contribute to load indicator dispersions because these large wavelengths could deviate from the monthly mean component (vector) wind profile that was previously used to establish ascent guidance.

Wind-Vehicle Aerodynamic Loads Analysis. In principle, it is possible to compute the responses of a launch vehicle to a large number of high-resolution wind profiles and to evaluate the results in a Monte Carlo-type statistical analysis. However, this is both expensive and time consuming, especially if one wants to assess the influence of various system and control parameters on the vehicle responses. The statistical techniques of dynamic analysis attempt to avoid the disadvantage of the Monte Carlo approach by relating the statistics of the input (wind) to the statistics of the output (loads) of a dynamical system (launch vehicle). In preliminary load analyses, the launch vehicle is normally regarded as a rigid body.

Three descriptions of wind disturbances have been used in calculating aerodynamic loads on a vehicle in powered flight through the atmosphere.

Measured Wind Profiles. Using detailed, individual measured (Jimsphere type) wind profiles as a function of altitude and wind direction are required. However, this realistic method requires the analysis

of a large number of representative wind profiles in a Monte Carlo manner. Two other quasi-realistic wind profile schemes have also been used:

• Generating a wind profile by properly filtering the output of a white noise generator to obtain the variance and turbulence portion, which is then added to the monthly mean wind.

• Using rawinsonde wind profiles and adding the turbulence to these profiles by filtering the output of a white noise generator.

Refer to Johnson (2008) and Geissler (1970) for details of applying winds to the various elements and phases in engineering design studies.

Synthetic Wind Profiles. Disturbances represented by a single synthetic (or discrete) wind profile contain several statistical properties of the in-flight wind field (steady-state wind, shear, gust). However, this older method does not completely define the aerodynamic loads over a large class of vehicle systems once the aerodynamic characteristics are well defined.

Statistical Wind Profiles. Statistical wind profiles give a stochastic type of statistical representation. However, this older method generally restricts the analysis to be a Gaussian, stochastic wind process with linear dynamical systems.

Nonstationary Statistical Methods. With the restrictive power spectrum assumptions, it is necessary for a more accurate analysis to employ nonstationary methods for the structural load analysis. These methods assume a linear time-varying system and a Gaussian distribution of the wind input. It is standard in engineering applications to assume that the nonstationary stochastic wind process can be adequately approximated by a linear time-varying differential system, a shaping filter, excited by white noise. This assumption results in a considerable simplification in the mathematical analysis. There are basically two methods of analysis – the State Space Representation and the Impulse Response Representation – both discussed in Geissler (1970).

Ascent Structural Loads Analysis. In 1988, the introduction was made of extreme value (Gumbel) statistics as a methodology for the analysis of aerospace vehicle ascent structural loads and the establishment of wind load increments for protection of the commit-to-launch decision for the Shuttle program. Extreme value analysis and development of methods for Shuttle go and no-go joint and conditional probabilities for various DOL wind biasing scenarios.

Since the Shuttle decision to launch is based on trajectory and loads simulations using a wind profile measurement taken 4.5 h prior to launch, load increments that protect for 99% of the load change during the 4.5-h period are calculated for all wind profile sensitive load indicators.

For the Shuttle, there is an advantage in reducing the ascent wind loads by biasing the ascent trajectory in the pitch and yaw planes to the DOL measured wind profile using either the Day-of-Launch I-LOAD Biasing System (DIBS) or FIBS (a modified DIBS) steering command techniques. The analytical statistical techniques using extreme value statistics have advantages over empirical statistical

techniques using extreme value statistics have advantages over empirical statistical techniques for aerospace programmatic management decisions for design, trade studies, design assessments, and redesign, and in the DOL go/no-go decision process.

Monthly Vector Wind Profile Model. Range and cross-range wind speed (scalar) profiles, along with idealized (synthetic) wind profiles, were used for many years in the design of launch vehicles for answering questions such as: What is the probability that a given wind speed aloft will occur in the pitch and yaw planes with a given launch azimuth? Or, what winds aloft are not expected to be exceeded for a given month? However, since the advent of the MSFC monthly VWP model, for a given site, it has replaced many of these percentile profile procedures.

The monthly VWP model was constructed to provide VWPs based on a statistical model for the launch vehicle engineering design community that has wide application in establishing realistic estimates of the dispersions of critical vehicle design parameters related to wind profile dispersions, mainly in vehicle load/guidance design studies. See Smith and Adelfang (1998).

An improved monthly vector wind profile model was developed in 1992 that is more complete, has no simplifying assumptions, and was proposed for all future launch vehicle development programs (Smith and Adelfang 1998). This enveloping version uses the same approach in defining the given wind vectors on the monthly enveloping probability ellipse at a reference altitude.

Details concerning the application of the five MSFC-developed synthetic scalar and VWP models can be found in Johnson (2008) and Smith and Adelfang (1998). The development of wind profile models for aerospace vehicle design applications has been an evolutionary process, and as aerospace engineering science advancements are made, there will be requirements for more advanced wind models. The recommended model for a particular vehicle must be tailored to meet specific program requirements and vehicle mission objectives in the vehicle development phase.

Background. The primary application of wind profile modeling is for establishing dispersions of launch vehicle aerodynamic load indicators. In the past, program managers were reluctant to establish ascent wind loads alleviation techniques during the initial design phase of an aerospace vehicle. Therefore, the synthetic scalar wind profile model was initially used. With technological advancements in vehicle design, along with insight in wind modeling, less conservative wind load alleviation techniques based on vector wind profiles were then readily incorporated into the design and operation phases of aerospace vehicle systems. However, wind dispersions produced by wind profile models may not be highly correlated with the dispersions of the aerodynamic load indicators estimated with a trajectory model for a specific vehicle.

Application. The most useful engineering design application of any wind profile model is the establishment of preliminary design ranges for angle of attack (α), angle of sideslip (β), aerodynamic pressure (q), and two aerodynamic load rigid body load indicators, the products, $q\alpha$ and $q\beta$. These and

other flight variables are derived from ascent flight 6-degree of freedom trajectory simulations using wind model profiles.

Elastic body loads are determined from flutter and vibration analyses using model wind profiles augmented to include smallscale wind perturbations.

Another useful application is the estimation of flight performance reserve for propellant to ensure orbital insertion by protecting for flight dispersions attributable in part to wind profile dispersions.

Rule of Thumb – The VWP model is suitable for applications in launch vehicle design studies that require assessments of vehicle trajectory and aerodynamic load dispersions attributable to monthly wind profile dispersions. Launch vehicle ascent guidance and control system (autopilot) steering commands are programmed for flight through the profile of monthly mean wind. Various vehicle programs have used different terms for the programmed steering commands, i.e., the chi-tilt and later the wind-biased trajectory (Saturn) and the I-Load (Shuttle). During initial studies, a number of months are normally used to establish the model profiles that produce the largest monthly dispersions of ascent vehicle aerodynamic load indicators, qα and qβ. Since the largest monthly dispersions for wind normally occur during the winter's high-wind months, it is appropriate to use the worst month from the winter season for establishment of the design reference, qα and qβ, dispersions.

Following the preliminary vehicle design using a synthetic or VWP wind profile model, trade studies are made to establish a requirement to bias steering to reduce wind loads. The usual procedure is to establish first-stage steering based on the profile of monthly mean winds in the pitch and yaw planes. Wind engineering data are established, and structural loads and performance assessments are made using samples of high-resolution wind profile measurements.

Description of Wind Shear, Gust, and Turbulence Models. The small-scale motions (turbulence) associated with vertical detailed wind profiles are characterized, in general, by a super- position of discrete and mostly irregular gusts containing random frequency components. Turbulence is defined as a series of irregular gusts. Two methods are available for determining the vehicle response (loads) due to atmospheric turbulence and discrete gusts – the discrete (step) gust concept and the power spectral concept. In both methods, the larger resulting loads are added to the loads resulting from the analysis given in the previous section for winds.

Discrete Gust. Loads resulting from penetration of a discrete gust can be calculated from the immersion gust concept, which considers the vehicle as being a point, and static loads are calculated as the reference point traverses the gust. Vehicle length is used as a reference length only when the aerodynamic load is distributed over the entire vehicle. A better method for typical launch vehicles is that of quasi-steady gust penetration. Aerodynamic inertia effects are neglected and the steady-state load appropriate to a given body station is obtained as the gust front passes the station. The time lag associated with lift buildup therefore corresponds to the length of a given lifting area rather than the vehicle length. This method would not be suitable for a body, like a cone, which generates lift over the

entire length.

• Gust Models for Launch Vehicle Ascent. Assessments of elastic body and buffeting response to in-flight atmospheric disturbances or gusts are important in establishing vehicle design structural requirements and operational capability. Even though rigid body loads simulations are done on DOL using Jimsphere-measured wind profiles, it is not practical to perform elastic body loads analyses on DOL because gusts are transient with time duration measured in seconds. Thus, the commit-to- launch decision must be protected for gust uncertainty contribution to elastic body loads uncertainties. Therefore, discrete gust models have been established for this DOL design purpose. The details and applications concerning these models are presented in Johnson (2008) and NASA (n.d.).

• Classical NASA 9-m/s discrete gust model. Since one cannot monitor short (gust) wavelengths, this gust model was derived as a direct vehicle design requirement to help establish the design of vehicle structure and control systems. This was intended to produce a minimum risk flight capability taking into account, from a systems engineering point of view, the aerodynamic and other uncertainties. It was originally taken from aircraft gust studies.

The original quasi-square wave gust model was developed by NASA in 1963 and has an amplitude of 9 m/s, with a gust width from 60 to 300 m, as shown in Fig 2. It is used by NASA for elastic body loads and is based on established methods (and aircraft turbulence data) that are included in MIL-F-8785B.40 When used in conjunction with the synthetic wind and wind shear model for Shuttle ascent design, the design gust model amplitude is reduced to 7.65 m/s (0.85 of its value). However, although small, it is not known exactly what probability of occurrence should be attached to this gust model. Also, there is no relationship between gust magnitude and gust half width (between 30 and 150 m). Inferred evidence from aircraft vertical gust measurements to support application of the 9 m/s discrete gusts with half-widths as small as 30 m.

• Improved discrete gust model. The improved discrete gust model was introduced in 1997 (Smith and Adelfang 1998), and is also established with methods originally developed for MIL-F-8785B (Department of Defense 1969). However, it is a gust model that includes variation of gust amplitude (magnitude) with gust width (half width). It is also a function of altitude and reflects the severity of turbulence.

Power Spectral. The power spectral approach provides a more realistic description of the continuous nature of atmospheric turbulence on a vehicle. The turbulence power spectra are used as a forcing function, and the response spectra are obtained through use of the vehicle frequency response function. The vehicle frequency response function can be calculated numerically for a range of sinusoidal gust frequencies and used with any desired turbulence spectrum. Spectral methods have been employed to specify the characteristics of small-scale motions. Spectra of detailed wind profiles (scalar, zonal, and meridional) can be computed (with and without filtering) for engineering design studies. Energy

(variance) of the small-scale motions is not homogenous; i.e., it is not constant with altitude. The energy content over limited latitude intervals and for limited frequency bands may be much larger than that represented by the average spectra (50th percentile). The range of energy content is given approximately by the 1st and 99th percentile envelopes. This range of energy should be kept in mind when employing spectra of small-scale motions to interpret the significance of vehicle responses.

• Power Spectrum Analysis. The determination of aerodynamic loads by power spectrum analysis is restricted to linear time-invariant differential systems with stationary input processes. It is evident that the flight of the launch vehicle through the atmosphere is a strongly nonstationary process. Not only does the system parameters vary due to the rapid propellant consumption but also the atmospheric flight conditions. The difficulty can partly be circumvented by restricting the analysis to small time intervals and assuming the spatial characteristics of the wind process to have local stationarity. The latter condition is approximately satisfied for the wind turbulence. A widely used power spectrum model for the turbulence is that of H. Press, containing the scale of turbulence (L) and the variance of the turbulence (σt). At altitudes below 50,000 ft, this power spectrum seems to be an acceptable model for the atmospheric turbulence, with the scale of turbulence ranging from 500 to 1,000 m, depending on the altitude and the variance of the turbulence from 1 to 4 m2/s2. Other possible forms of power spectra can be used. The Press turbulence model approximates only the variance of wind but poorly approximates that of the wind shear (wind shear variance becomes infinite). This presents a problem in calculating the number of exceedances (becoming infinite) for a vehicle with angle of attack feedback. This difficulty can be avoided by using a power spectrum model that conforms to specified wind and wind shear variances.

Sometimes it is advantageous in statistical simulation studies to construct a random signal as the output of a dynamical system excited by an independent Gaussian stochastic process – white noise, since white noise is characterized by a constant power spectrum.

Deterministic vehicle dynamic analysis involving wind and atmospheric parameters.

Aerodynamic Forces and Moments. In addition to the gravity force, the atmosphere exerts pressure on the launch vehicle, resulting in aerodynamic forces and moments. Various models of the atmosphere (Standard and Range Reference Atmospheres) have been used, which should provide acceptable accuracy in determining aerodynamic loads for any launch site. For axially symmetric vehicles, the absolute angle of attack is sufficient in calculating aerodynamic forces and moments for a boost trajectory. It is desirable to have the capability to break the launch vehicle down into several aerodynamic sections in order to incorporate the effects of gradual gust penetration. The buoyancy due to the air displaced by large Saturn-type vehicles is » 0.1% of the total thrust and can be neglected.

The NASA MSFC Global Reference Atmospheric Model (Leslie and Justus 2008) is a worldwide model from surface through orbital altitudes that can be used to calculate monthly mean atmospheric

thermodynamic (and wind) properties, and the variability of these properties about the monthly mean, for any global location or along any given trajectory. A schematic illustration of the atmospheric regions within the GRAM-07 program, and sources for the models and data on which the mean monthly GRAM-07 values are based is presented in Fig. 3.

Thrust. Thrust for a given propellant and rocket motor geometry depends not only on the mass flow rate and effective exhaust velocity but also on the ambient atmospheric pressure and thus the altitude of the vehicle. Since the atmospheric pressure is the only thrust parameter that goes through significant changes during booster flight, the use of a single-entry table is sufficient for the calculation of the thrust force. The key is to specify the reference atmosphere that is used for this input, i.e. US76, etc.Atmospheric moisture has also been a parameter to consider in the design and in calculating the performance of various vehicle engines, such as in the National Aero Space Plane (NASP) program (Johnson 1994).

Engine Inertia. The swivel engines, in responding to commands from the G&C computer, can be deflected at substantial angular accelerations, which gives rise to inertia forces and moments caused by the engine inertia. Although the engine inertia effect can be of importance for high wind shear conditions, it is often overshadowed by lag effects of servo-actuator engine compliance and shaping networks.
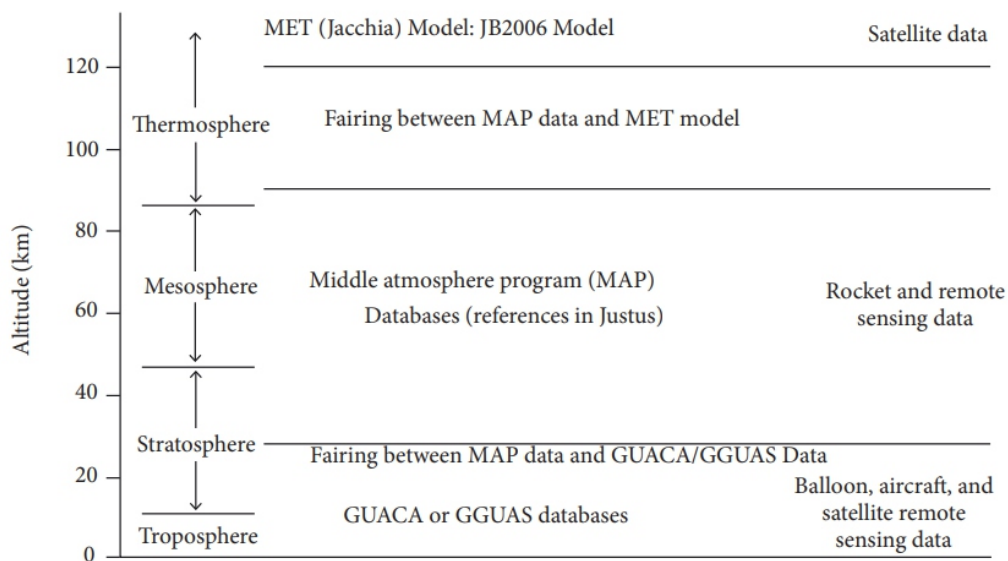
Figure 3. Schematic summary of the atmospheric regions versus altitude in the GRAM-07 program, and sources for the models/data on which the mean monthly GRAM-07 values are based (Johnson, 2008).

Statistical Terrestrial Environment Mission Analysis. Most standard statistical summaries of terrestrial environment variables are tabulated for single variables or a combination of a few variables,

such as cloud ceilings and visibilities, and they require parametric statistical summaries. Interest is not only in the probability of each of the several terrestrial environment variables taken separately, but also in the probability that at least one of several variables will be of concern for a launch vehicle's particular operational phase or several phases. For example, if there is a launch constraint due to several terrestrial environment parameters of which any one will constitute a no-go condition, then the probability of interest is the probability that any one of the constraints will occur. The purpose of a statistical terrestrial environment mission analysis is to address the following questions relative to assumed or assigned natural environmental constraints for the operational phases of a new launch vehicle:

• What is the probability that the designated natural environmental constraints will (will not) occur during a particular monthly reference period?

• What is the probability that the designated natural environmental constraints will (will not) occur for N consecutive days at a particular time of day during a monthly reference period?

• Once the designated natural environmental constraint has occurred (has not occurred) for 1, 2, 3, … N consecutive days at a particular time of day, what is the probability that the given constraints will continue for N additional days?

Valid answers to these questions have practical applications to any new launch vehicle program development in the following LV mission interrelated areas:

• Establishing terrestrial environment design criteria.

• Operational planning.

• Establishing launch and flight operational rules.

• Program decisions on cost-trade assessments.

CONCLUSION

Terrestrial and space environments associated with the design and development of new launch or space vehicles are presented here and in the previous two JATM papers. These papers also address the basis for the NE guidelines presented, the interpretation of the guidelines, and application to the development of launch/space vehicle design requirements. Any new launch vehicle program or project should consider, early in its development stages, the NE guideline applications suggested in this paper. A better understanding and application of the NE and its effect on launch vehicles will enable engineering and program management to more effectively minimize program risks and costs, optimize design quality, and successfully achieve mission objectives.

AUTHOR'S CONTRIBUTION

Conceptualization, Johnson DL; Methodology, Johnson DL; Investigation, Johnson DL; Writing – Original Draft, Johnson DL; Writing – Review and Editing, Vaughan WW; Resources, Johnson DL and

and Vaughan WW; Supervision, Johnson DL and Vaughan WW and Vaughan WW; Supervision, Johnson DL and Vaughan WW

REFERENCES

Adelfang SI (1999) User's guide for monthly vector wind profile model. (CR-1999-209759). NASA Technical Report.

Adelfang SI, Smith OE, Batts GW (1994) Ascent wind model for launch vehicle design. J Spacecraft and Rockets 31(3):502-508. https://doi.org/10.2514/3.26467

Bowman BR, Tobiska WK, Marcos FA, Valladares C (2008) The JB2006 empirical thermosphere density model. Journal of Atmospheric and Solar-Terrestrial Physics 70(5):774-793. https://doi.org/10.1016/j.jastp.2007.10.002

Department of Defense (1969) Military Specification Flying Qualities of Piloted Airplanes. (MILF-8785B). US Airforce Technical Report.

Geissler ED (1970) Wind effects on launch vehicles. Slough: Technivision Services.

Leslie FW, Justus CG (2008) The NASA MSFC Earth global reference atmospheric model – 2007 Version. (TM-2008-215581). NASA Technical Memorandum.

Johnson DL (1994) National aerospace plane (NASP) X-30 natural environment requirements document (Rev. 1.0). (TM-108451). NASA Technical Memorandum.

Johnson DL (2008) Terrestrial environment (climatic) criteria guidelines for use in aerospace vehicle development, 2008 Revision. (TM2008-215633). NASA Technical Memorandum.

Johnson DL; Vaughan WW (2019) The Role of Terrestrial and Space Environments in Launch Vehicle Development. J Aerosp Technol Manag, 11: e4719. https://doi.org/10.5028/jatm.v11.1088

Johnson DL; Vaughan WW (2020) Key Terrestrial And Space Environment Sources. J Aerosp Technol Manag, 12: e0120. https://doi.org/10.5028/jatm.v12.1089

[NASA] National Aeronautics and Space Administration (n.d.) NASA space vehicle design criteria SP-8000. NASA. http://library.msfc.nasa.gov/cgi-bin/lsp8000>Pearson SD, Vaughan WW, Batts CW, Jasper GL (1996) Importance of the natural terrestrial environment with regard to advanced launch vehicle design and development. (TM-108511). NASA Technical Memorandum.

Smith OE (1976) Vector wind and vector wind shear models 0 to 27km altitude for Cape Kennedy,

Florida and at Vandenberg AFB, California. (TM-X-73319). NASA Technical Report.

Smith OE, Adelfang SI (1998) A compendium of wind statistics and models for the NASA space shuttle and other aerospace vehicle programs. (CR-1998-208859). NASA Technical Report

Study of Design Modification Effects through Performance Analysis of a Legacy Gas Turbine Engine

Gantayata Gouda1,2, Balaji Sankar,1,* Venkat Iyengar1,2, Jana Soumendu1,2

A B S T R A C T

Modifications to the critical parameters, such as the exhaust nozzle area, are sometimes done during maintenance of aircraft engines. These modifications are done either to increase the design thrust or to compensate for the reduction of thrust due to leakage in the variable area jet nozzle. There is a trade-off between several performance parameters when such critical parameters are changed during maintenance. A tuned aerothermodynamic simulation model that agrees well with the experimental data from the original engine is required to study the effect of these changes. In the present work, a multipoint map scaling approach and a parameter estimation method are used to develop a simulation model that agrees well with the experimental data from the original turbojet engine. The design modifications are then incorporated in the model, and the effect of the modification on the various performance parameters is studied. The effect of leakage in the nozzle flaps and the corresponding reduction required in the nozzle throat area are calculated. It is shown that the tuned model developed with experimental testbed data enables the identification of ancillary effects of a change in a design parameter, such as the nozzle throat area.

KEYWORDS: Aerothermodynamic model, Twin spool turbojet engine, Multipoint map scaling, Compressor characteristics map

INTRODUCTION

Aerothermodynamic simulation models predict gas path parameters at different stations along the engine.In these models, only a single pressure or temperature value can be calculated at a station on the engine. They do not account for the radial or circumferential variation of gas path parameters. These models are typically used in the design and development phases of engines,as well as during performance evaluation of legacy engines. They also find use in the Engine Health Monitoring systems, which monitor the overall performance characteristics of gas turbines in terms of component performance parameters.

In this study, an in-house aerothermodynamic simulation model (design point and off-design point) has been modified to simulate a legacy twin spool gas turbine engine. These engines are periodically overhauled after being used in the field. As part of the overhaul procedure, engines are tested to check if they meet the performance standards. Testbed data is available for many engines of the same variant from theground-based static test bed. This data is available with the overhauling agency. Since both the engines and the testbed are old (1970), there is no provision for continuous time series monitoring of various parameters. They are noted down manually from testbed instrumentation. This type of data set is shown in the normalized form in Table 1. The data set provides gas path temperatures and pressures

along the engine. Using these measurements, the characteristics maps of an engine very similar to this one have been tuned, and are used to simulate the performance of the engine at cruise, nominal and max dry rating. Because of the use of a tuned characteristics map in simulation, the simulation model agrees well with the experimental data. This model is used to study the effect of a small reduction made in the exhaust area of the nozzle at full reheat rating. It is shown that, in addition to increasing the thrust of the engine, which was the original goal, the reduction of nozzle area also causes the high pressure spool of the twinspool turbojet to overspeed. It is hoped that the multipoint scaling techniques for compressor maps presented in this work will help in better tuning of engine models when testbed data is available.

Saravanamuttoo (1992) has described the use of aerothermodynamic simulation models in engine control system design and engine health monitoring. Details of engine performance and health monitoring models using steady state and transient performance prediction methods have been presented in by Isaac (1992). An adapted performance model has been used in the performance evaluation of the LM2500 industrial gas turbine, in the work reported by Bechini (2007) and Tsoutsanis (2010). A detailed review of the use of simulation models in performance analysis of gas turbines has been made by Li (2002). Limited information about the effect of various component degradations on the performance of the engine is available in the open literature, such as those given by Fasching (1982) and Kerrebrock (1992). In Sankar et al. (2015), the degradation that occurs in a turbojet engine during an extensive ground test over hundreds of hours is described. Several resources that detail the methodology of off- and on-design performance modeling of gas turbines are available, such as Mattingly (2006),Walsh et al. (2004), and Cohen et al.(2001). A significant hurdle in the development of these models for a legacy engine is the non-availability of realistic component characteristic maps and design data, such as bleed schedules, inter-duct losses, power off-take, and component geometry. Optimization-based and non-linear gas path analysis-based methods for the estimation of these component parameters have been presented by Li et al.(2006). For legacy engines, even design point parameters are often not available or the engine has degraded in such a way that the original design parameters are no longer achieved. Estimation of design point parameters from test bed data in such cases is presented in Sankar et al. (2016).

In the first place, this paper presents a brief description of the engine for which the model is being developed, followed by the characteristic map tuning process adopted to increase the accuracy of the simulation. An example of duct pressure loss and afterburner efficiency estimation is presented next. Using these component maps and estimated efficiencies, the off-design model is developed. After validation, the effect of reduction of exhaust area of the nozzle is simulated, and the results are plotted. The reason for the increase in RPM of HP spool is discussed in the conclusion.

ENGINE DESCRIPTION

The section view of the engine studied in this paper is shown in Fig. 1. The compressor of the engine is made up of a three-stage axial low pressure compressor and a five-stage axial high pressure compressor. The compressor does not have any provisions for variable inlet
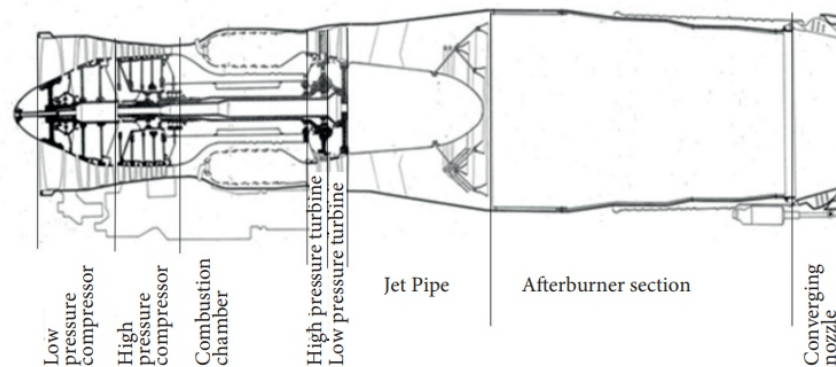

Figure 1. Section view of the turbojet engine showing major turbomachinery components.

or stator vanes. However, special perforated casing is provided for the low pressure spool to increase the surge margin at the low flow rates in off-design ratings. The compressor also has blown-off valves at the end of HPC (high pressure compressor) to further increase the surge margin during the starting of the engine. The combustor is a ten tube can-annular combustor of a straight flow type. The turbine sare axial and use reaction type blading, which are cooled in the HPT (high pressure turbine). The exhaust nozzle area does not change during the dry ratings of the engines. During the reheat ratings, the area increases in proportion to the increase in specific volume to the flow.

AVAILABLE EXPERIMENTAL DATA

The available experimental data has been collected at max dry rating and two additional off-design ratings. Furthermore, data is also available at the three reheat ratings with different afterburner fuel flow levels and the exhaust nozzle area. The available data has been tabulated in the normalized form in Table 1. The normalization is done with respect to the max dry rating, which is the design point of this engine. For AB (afterburner) fuel flow rate, the actual value in kg/s is given as the AB fuel flow rate in dry max rating is zero.

Table 1. Normalized experimental data available.

Parameter	Full reheat	Partial reheat	Minimum reheat	Max dry rating	Nominal rating	80% of nominal rating
N1	1.00	1.00	1.00	1.00	0.94	0.89
N2	1.03	1.01	1.01	1.00	0.96	0.92
Thrust	1.68	1.52	1.34	1.00	0.88	0.70
Thrust specific fuel consumption	2.21	2.02	1.60	1.00	0.93	0.91
LPC outlet total pressure	0.97	0.98	0.98	1.00	0.96	0.87
HPC outlet total pressure	1.05	1.02	1.02	1.00	0.92	0.80
HPT outlet total pressure	1.04	1.01	1.01	1.00	0.92	0.80
LPT outlet total pressure	1.14	1.07	1.07	1.00	0.93	0.82
Jet pipe static pressure after AB pressure loss	1.17	1.09	1.09	1.00	0.94	0.90
LPC outlet total temperature	0.99	0.99	0.99	1.00	0.96	0.93
HPC outlet total temperature	1.02	1.00	1.00	1.00	0.95	0.90
HPT outlet total temperature	1.10	1.03	1.03	1.00	0.91	0.83
LPT outlet total temperature	1.11	1.04	1.04	1.00	0.91	0.83
AB outlet total temperature	2.22	2.02	1.62	1.00	0.91	0.83
Combustor outlet temperature	1.10	1.03	1.03	1.00	0.91	0.82
Mass flow rate of air	1.00	1.00	1.00	1.00	0.96	0.88
Mass flow rate of fuel	1.20	1.07	1.07	1.00	0.81	0.63
Throat area	1.40	1.40	1.22	1.00	1.00	1.00
Mass flow rate of fuel AB	2.63	2.08	1.13	0.00	0.00	0.00

LPC = low pressure compressor; HPC = high pressure compressor; LPT = low pressure turbine; HPT = high pressure turbine; AB = afterburner.

METHODOLOGY

The compressor characteristics map is the most influential input required for the off-design modeling of the engine. The characteristics map, along with the inlet performance map, determines the errors in the simulation output to a large extent. When engine is tested in ground based test beds, they are typically equipped with smooth-contoured bell mouth intakes. Since the experimental data set for this engine is available from ground test bed, the inlet total pressure loss is very low. The methodology adopted to tune the compressor characteristics map is given in the next section

CHARACTERISTIC MAP TUNING

Characteristic performance maps of both low and high pressure compressors of an engine very similar to the current engine were available in Akhmedzjanov (2000), and were digitized and scaled to the current engine specifications. Scaling laws for compressor and turbine maps are given by Jones (2007). An improved scaling method that enhances the accuracy of the simulation in an overall least squares sense was presented in Sankar et al. (2014). In this approach, instead of using single point scaling of component maps, as given by Jones (2007), the maps are scaled in a way that the sum of squares of errors in static pressure and total temperature at the HPC and the LPT exits are minimized. In the present work, instead of scaling the maps based on a single point (typically design point), the maps are scaled over the

required operating range, using a scaling function, which operates on the original map to give the scaled map. The turbine maps are not tuned as they operate at a relatively constant pressure ratio in choked condition near the design point, as shown in Sankar et al. (2019)

The normalized map of LPC is displayed in Fig. 2 and a HPC map is shown in Fig. 3. The design beta value of both maps was found using an error minimization routine, though which, on the 100% RPM line, the beta value that gave the design pressure ratio was chosen as the design beta.
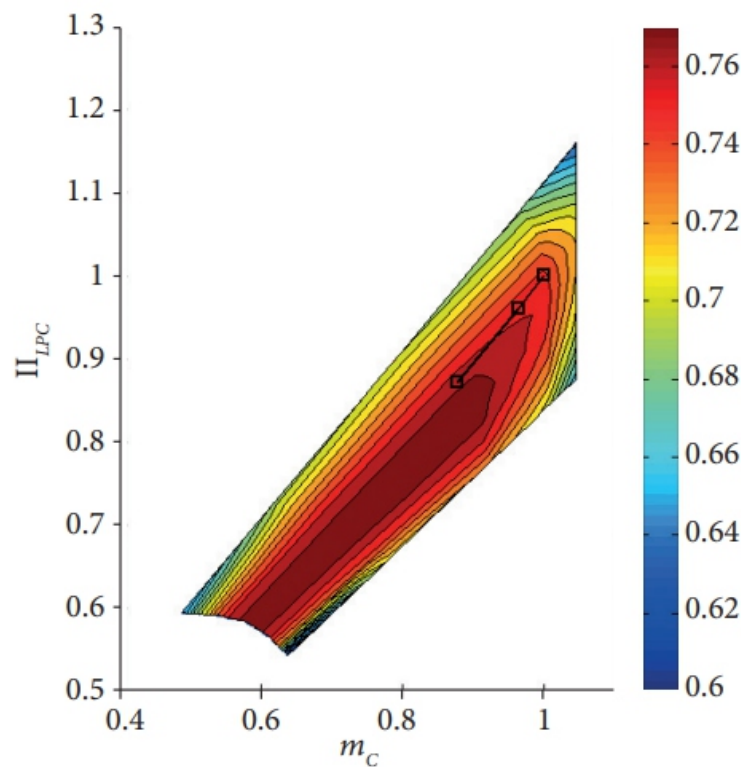
Figure 2. Original normalized LPC characteristics map. The markers indicate the location of design point, nominal rating, and 80% nominal rating.
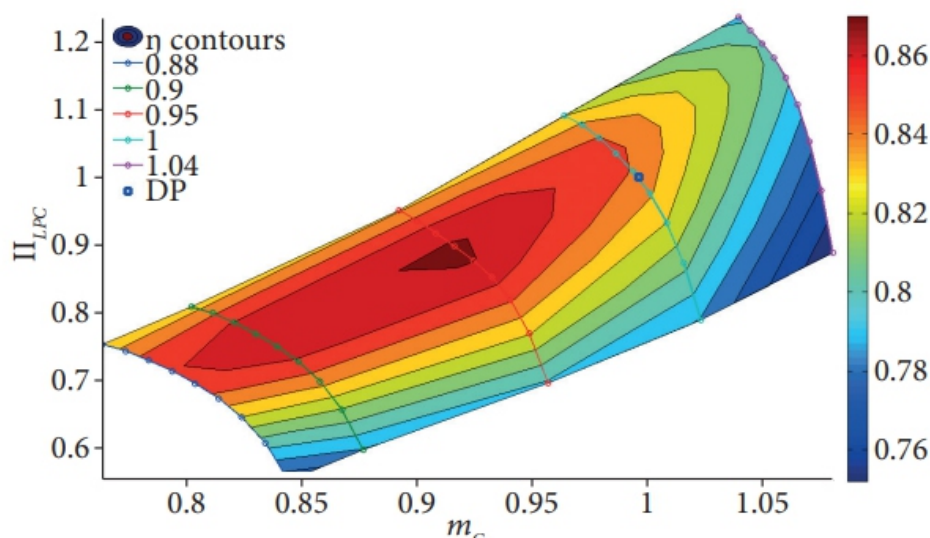
Figure 3. Original normalized HPC map.

The multipoint tuning process is described for the efficiency contours of the LPC map. Similar process has been applied for HPC map so that it is consistent with the experimental data available. The points on the LPC map for the three off-design ratings can be identified using the mass flow rate and the pressure ratio of the LPC corresponding to these three ratings. The efficiencies for these operating points can be obtained from the efficiency contours of this map using interpolation techniques. Also, from inlet and exit gas properties of the LPC, (presented in Table 1), the isentropic efficiencies of the LPC can be calculated for these three off-design ratings. The two sets of efficiency values, one from characteristics map and one from the experimental data are compared in subplot of Fig. 4a, where the red markers indicate the efficiency values obtained from the map, in which an only single design point scaling has been applied. Hence, there is an exact match only at the design point and a marked difference in efficiencies at other two off-design ratings. A scaling function needs to be applied to the characteristics map to make it agree with the data at the other two off-design ratings. This scaling function is computed with RPM as the input argument and is plotted in Fig. 5. After the application of this scaling function on the single point scaled map, the resulting map agrees well with the experimental data as shown in the subplot of Fig. 4b. The efficiency contours on the LPC map after applying the multipoint scaling function are displayed in Fig. 6.
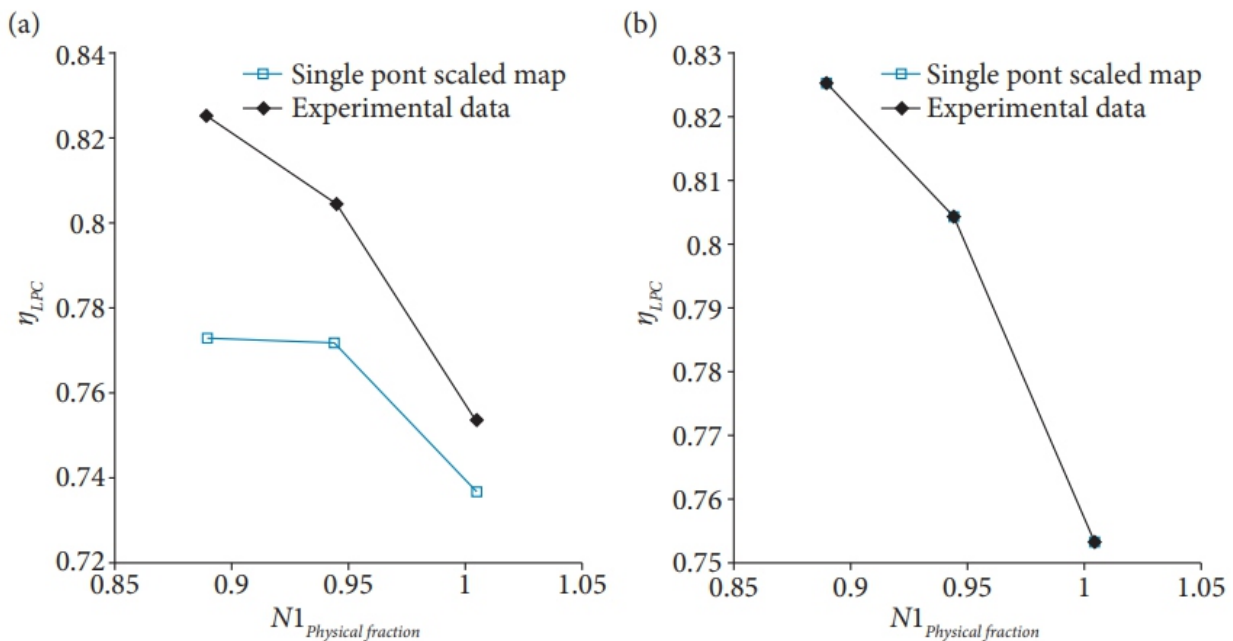
Figure 4. Comparison of efficiency values from characteristics map and experimental data before multipoint scaling (a) and after multipoint scaling (b).
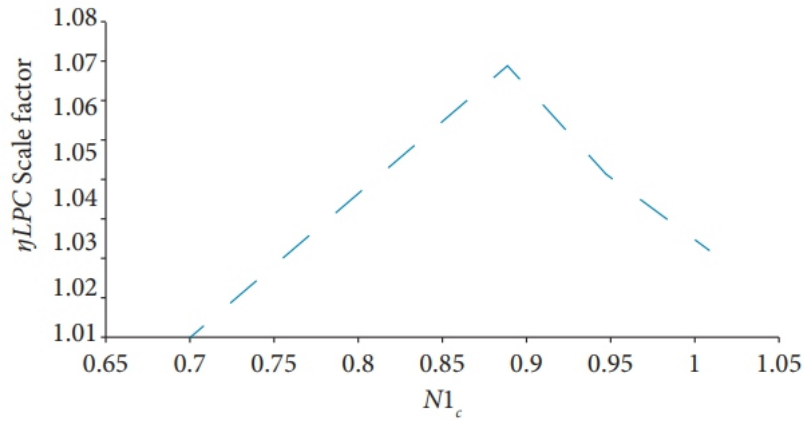
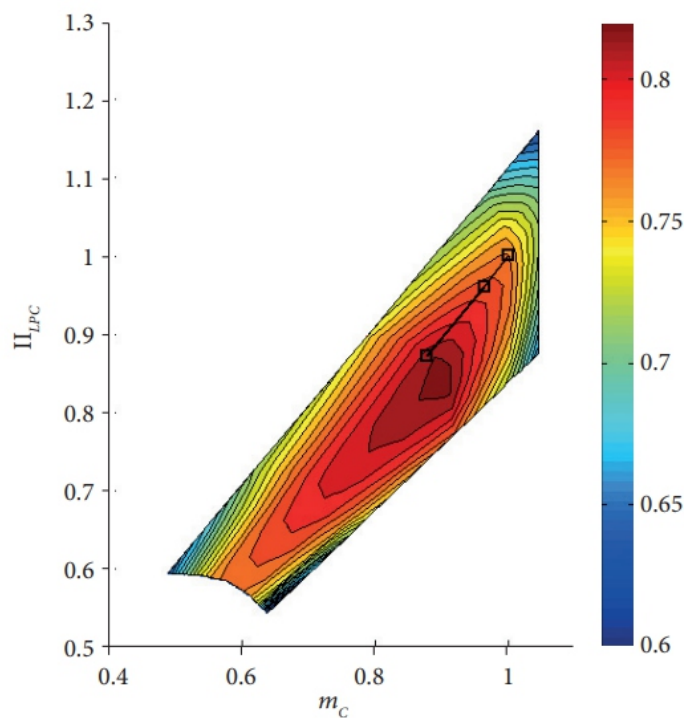**Figure 5.** Scale factor to be applied to LPC efficiency map.

Figure 6. Multipoint scaled LPC map.

In addition to scaling of the efficiencies, it has to be ensured that the mass flow rate and the pressure ratio combinations of all the operating points occur at the respective RPM of the HPC. This is important since one of the significant effects of the reduction in the exhaust nozzle area is the change of N2 RPM for the same rating. The experimentally obtained operating line has been plotted on the HPC map presented in Fig. 7. The physical RPM corresponding to the off-design rating is typically available from the test bed, and is compared to the RPM from the HPC map in Table 2.
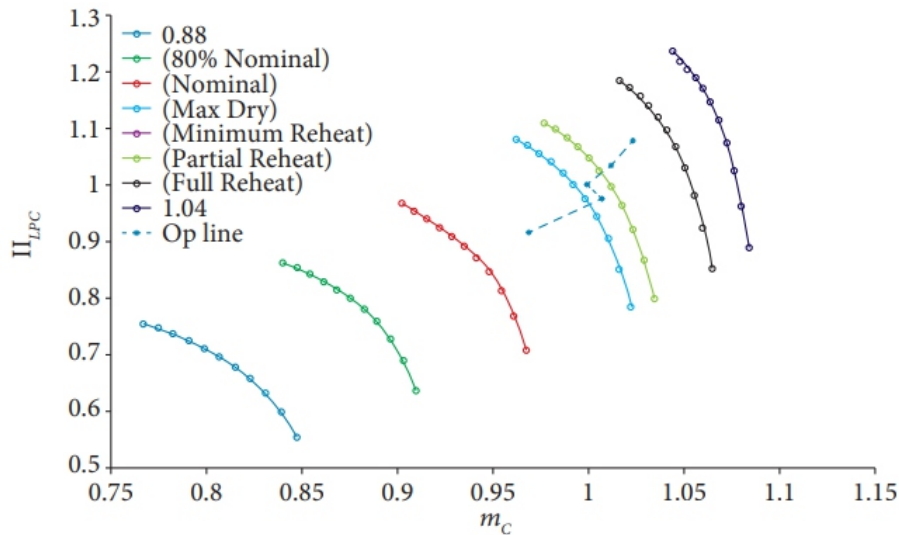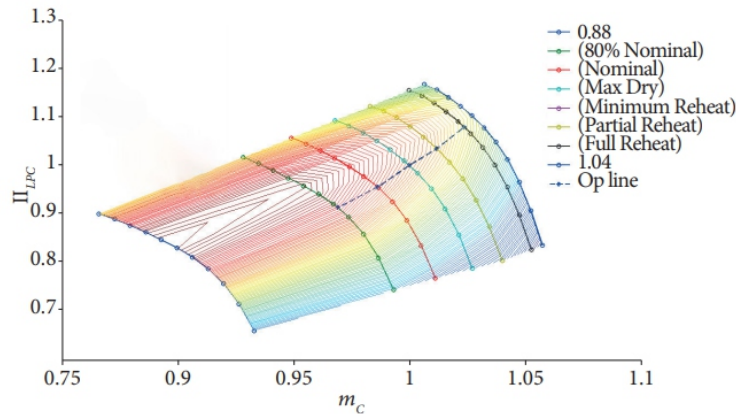
Figure 7. HPC map with experimentally obtained operating line before application scaling function on map. The figure shows that the experimental mass flow rate and pressure ratio do not lie on the respective RPM lines of the characteristics map.

Table 2. N2 RPM (revolutions per minute) corresponding to off-design ratings from map and from experiments.

Rating	Full reheat	Partial reheat	Minimum reheat	Max dry	Nominal	80% of nominal
Experimental RPM (corrected)	1.008	1.006	1.006	1.000	0.974	0.954
RPM that matches pressure ratio and mass flow rate from the map	1.017	1.008	1.008	1.000	0.993	0.970

A scale factor function similar to the LPC efficiency scaling function is applied to the HPC map to make the operating points fall on the respective constant RPM lines. This scale factor is plotted in Fig. 8. The HPC maps before and after application of the scaling function is displayed in Fig. 7 and Fig. 9, respectively. After tuning to match RPM, the map is again tuned to match efficiency values from test data, similar to the way LPC map was tuned. The tuned HPC map is presented in Fig. 10.
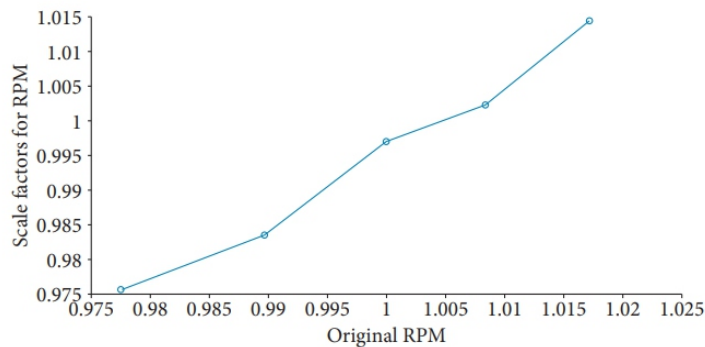
Figure 8. Scale factor to be applied to the HPC map RPM.

Figure 9. HPC map with experimentally obtained operating line after application scaling function on map. The figure shows that the experimental mass flow rate and the pressure ratio lie on the respective RPM lines of the characteristics map.
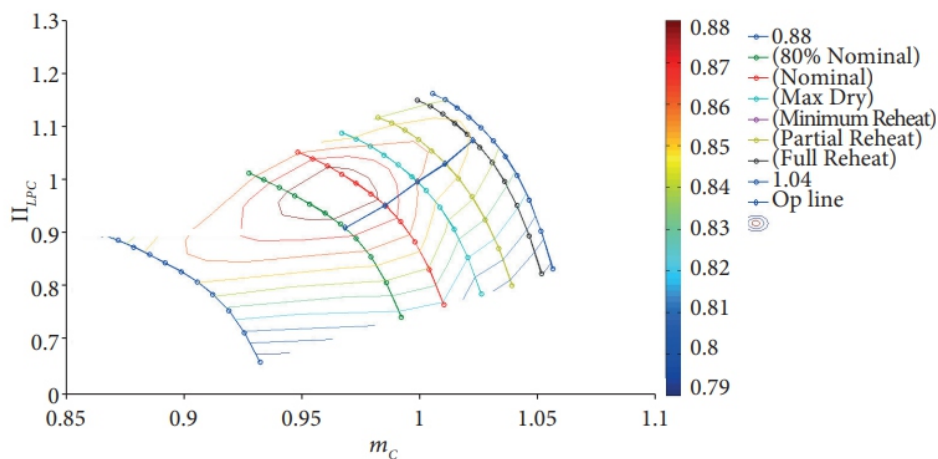

Figure 10. HPC map with efficiency contours scaled using multipoint scaling, so that efficiencies from the map agree with experimental data

DUCT PRESSURE LOSS FACTOR AND AB EFFICIENCY:

Apart from tuning the component characteristics map of LPC and HPC using the available inlet and exit conditions of both the components, several duct pressure loss factors need to be estimated. These inter-component duct pressure losses are calculated using pressure measurements at various stations given in Table 1. AB pressure loss variation as a function of air mass flow rate is displayed in Fig. 11. Also, since AB fuel flow rate and temperature rise are known, the efficiency of AB can be calculated for a known lower heating value of fuel. The estimated combustion efficiency is shown in Fig. 12.
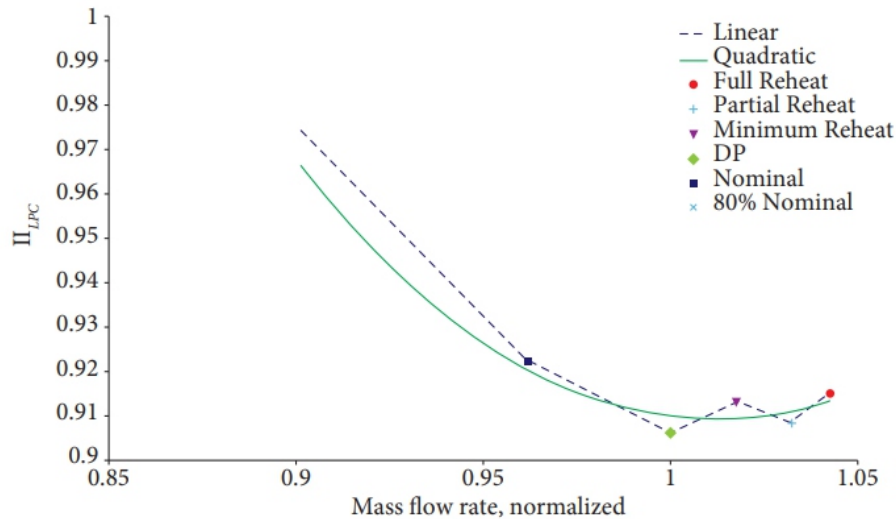
Figure 11. AB pressure loss factor estimated as a function of normalised mass flow rate.
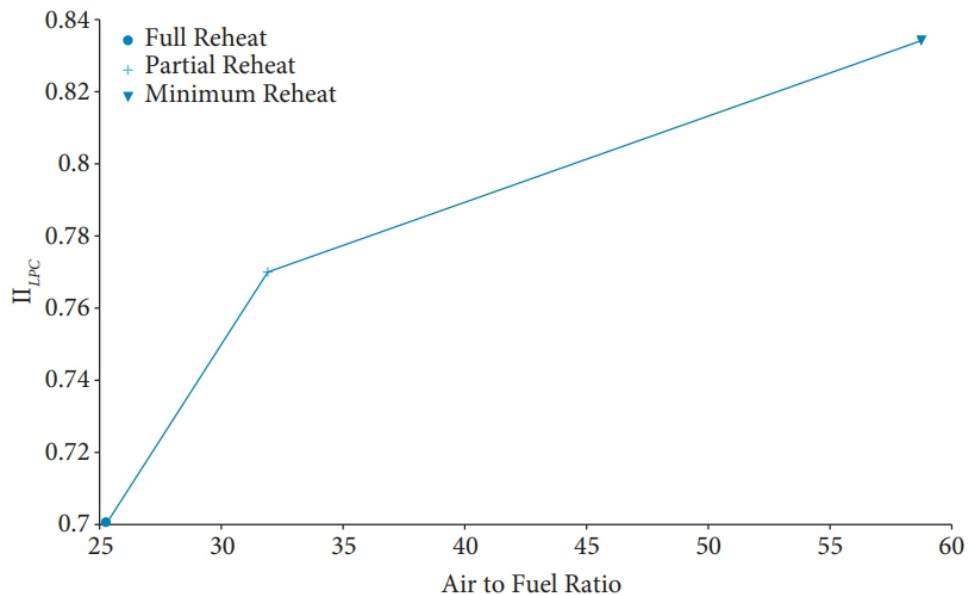

Figure 12. AB efficiency as a function of air-to-fuel ratio.

PERFORMANCE ANALYSIS USING SIMULATION MODEL

The methodology followed in this work for off-design simulation is based on the matrix iterative technique detailed in Walsh and Fletcher (2004). This approach of simulation model development has earlier been applied to a single spool engine, as detailed in Sankar et al. (2013). This approach accounts for the variation of properties of the gas along the engine by appropriately changing the specific heat. This method can, hence, simulate different composition of gases along the engine, as done in Sankar et al. (2017). A brief summary of this approach is given as follows. The three parameters that determine the operating point of a

twin spool engine are the operating point of low pressure and high pressure compressor (βlpc, βlpc) and

the main burner fuel flow rate $\acute{m}f$. This operating vector is given a $\begin{bmatrix} \beta_{lpc} \\ \beta_{hpc} \\ \acute{m}_f \end{bmatrix}$ .The engine has to satisfy mass and energy balance at all operating points at steady state ratings:

• Work extracted by the HPT = work consumed by the HPC;

• Work extracted by the LPT = work consumed by the LPC;

• Mass flow from combustor = mass flow into the HPT;

• Mass flow from HPT = mass flow into the LPT;

• Mass flow from LPT = mass flow into the convergent nozzle throat.

The energy balance is inherently satisfied at the two turbines as their pressure ratios are calculated from energy balance only. However, mass flow rate across the turbine for this pressure ratio may not be the mass flow rate pushed into it by the preceding component. In case mass balance is not satisfied, errors in mass flow occur at two turbines and at the nozzle. These errors have to be made nearly zero. The three errors that have to be minimized in order to obtain the operating vector are mass flow errors at high pressure and low pressure turbines $\left(\acute{m}_{hpt}^{error}, \acute{m}_{lpt}^{error} \right)$ and nozzle $\acute{m}_{nozzle}^{error}$. This error vector is given as $\begin{bmatrix} \acute{m}_{hpt}^{error} \\ \acute{m}_{lpt}^{error} \\ \acute{m}_{nozzle}^{error} \end{bmatrix}$.

Each term of the Jacobian matrix is a partial derivative of a single error with respect to a single independent variable. This is calculated with the same simulation model by using small perturbation technique. Once the full matrix has been computed, a damped Newton-Raphson iterative scheme is used to find the operating vector in order to minimize the error vector. The Jacobian matrix, which gives the variation of error with respect to operating vector, is re-evaluated during each iteration due to the non-linearity of the problem. The change in guess of the operating vector is then calculated by solving Eq.1:

$$
\begin{bmatrix}
\dfrac{\partial \acute{m}_{hpt}^{error}}{\partial \beta_{lpc}} & \dfrac{\partial \acute{m}_{hpt}^{error}}{\partial \beta_{hpc}} & \dfrac{\partial \acute{m}_{hpt}^{error}}{\partial \acute{m}_f} \\
\dfrac{\partial \acute{m}_{lpt}^{error}}{\partial \beta_{lpc}} & \dfrac{\partial \acute{m}_{lpt}^{error}}{\partial \beta_{hpc}} & \dfrac{\partial \acute{m}_{lpt}^{error}}{\partial \acute{m}_f} \\
\dfrac{\partial \acute{m}_{nozzle}^{error}}{\partial \beta_{lpc}} & \dfrac{\partial \acute{m}_{nozzle}^{error}}{\partial \beta_{hpc}} & \dfrac{\partial \acute{m}_{nozzle}^{error}}{\partial \acute{m}_f}
\end{bmatrix}
\begin{bmatrix}
\beta_{lpc} \\
\beta_{hpc} \\
\acute{m}_f
\end{bmatrix}
=
\begin{bmatrix}
\acute{m}_{hpt}^{error} \\
\acute{m}_{lpt}^{error} \\
\acute{m}_{nozzle}^{error}
\end{bmatrix}
$$

For a given off-design point, once the errors have reduced to a value specified by the convergence limit, the operating vector for this error condition is saved as the operating vector for the particular operating

point, which is usually at a lower RPM, the values from the current operating point are used as a starting guess.

The results of the simulation are presented in Fig. 13. This figure shows the operating line of the LPC and the HPC on their respective maps. It can be seen, from the operating line slope that the HPC moves closer to surge at higher ratings of the engine. The constant RPM lines are shown in multiple colors from 70 to 110% of design speed. The operating line obtained from the simulation is shown as a continuous black line. As the engine accelerates from cruise rating to max dry rating through the nominal rating, pressure ratio and mass flow rate increase almost in a linear fashion. After reaching 100% of design speed, when the reheat is engaged in the after burner, the RPM is maintained constant while there is a small dip in the pressure ratio. The LPC operating point for both minimal reheat rating and partial reheat rating
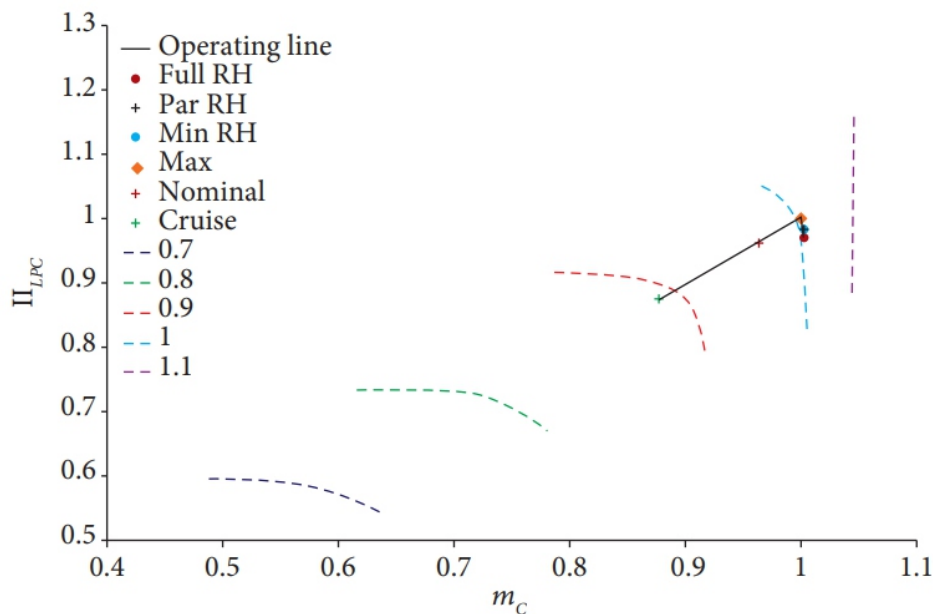
Figure 13. Characteristic maps with simulated operating line(shown in black). Also experimental operating points corresponding to different ratings are shown with markers.

is the same, since there is no change in the corrected gas path parameters up stream of the choked LPT NGV during these two ratings. However, during the full reheat rating, the main burner fuel flow rate is slightly increased from its value at partial reheat, resulting that the main burner exit temperature and the specific volume increases, which causes the HP spool to accelerate further to pass the mass flow coming in from the combustor. This acceleration of HP spool at the full reheat rating can be clearly seen in Fig.14. In this plot, operating points for minimum and partial reheat are coincident, but full reheat is at a higher RPM.
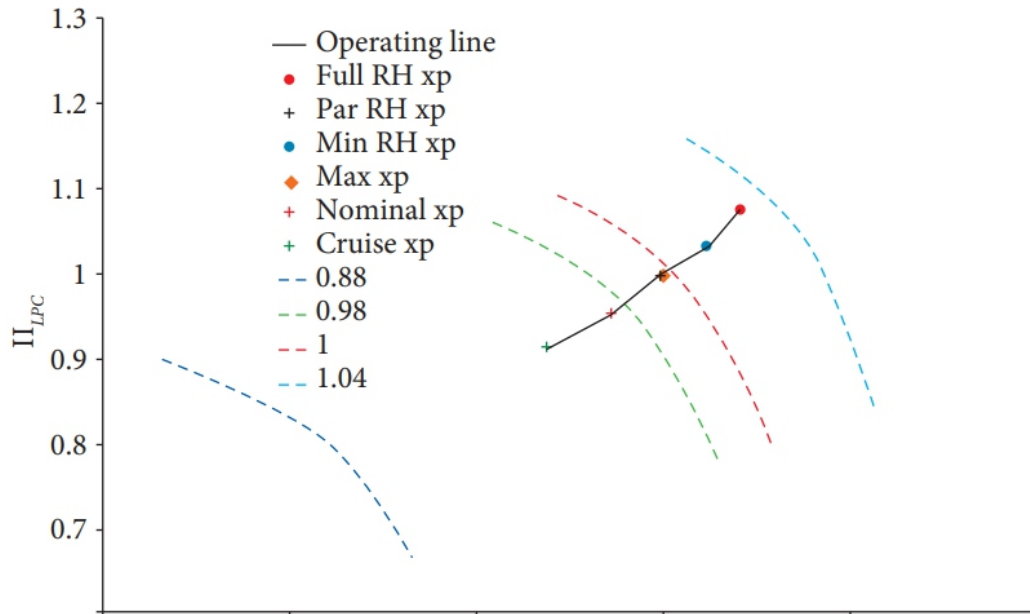
Figure 14. Characteristic maps with simulated operating line (shown in black). Also experimental operating points corresponding to different ratings are shown with markers.

The gas path temperatures and pressures from the simulation along the engine are also validated with experimental data. Pressures and temperatures are normalized using the design point LPC exit conditions. From the plots shown in Figure 15, it is evident that the agreement is very good between simulation and experimental data, which was ensured by using the experimental data for tuning component characteristic maps. The thrust and the fuel flow rate from simulation are depicted in Figure 16. In this plot, it can be seen that the main burner fuel flow rate also increases for full reheat rating over the partial reheat rating, which matches the increase in N2 RPM trend.
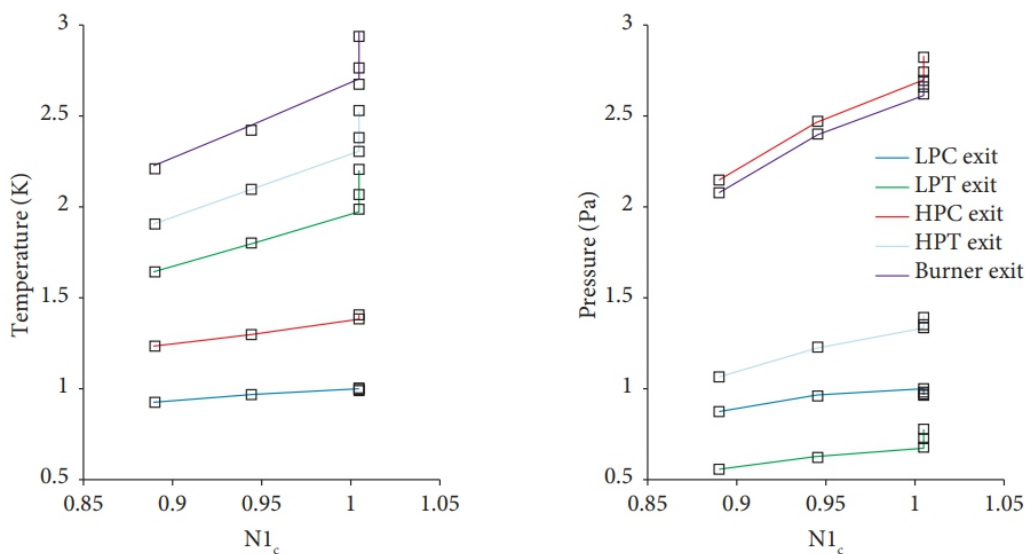
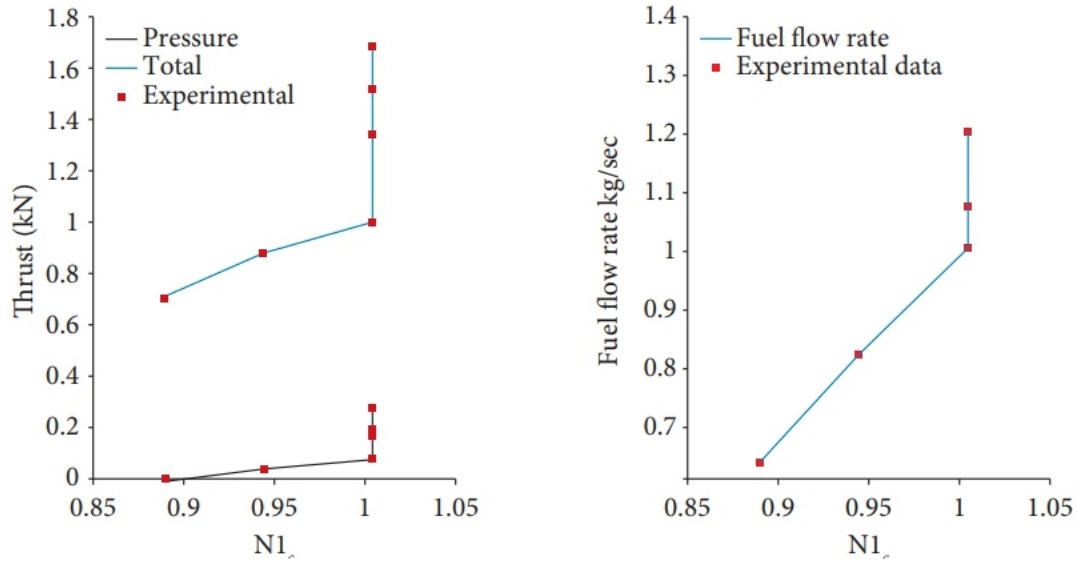**Figure 15.** Major gas path parameters from simulation, validated with test bed data.

Figure 16. Major performance parameters from simulation, validated with test bed data. Total thrust refers to summation of pressure and momentum thrust, obtained from simulation.

EFFECT OF CHANGE IN EXHAUST NOZZLE AREA IN A HEALTHY ENGINE

This validated simulation model is now used to study the effect of reduction of the exhaust nozzle area in a healthy engine. Said area is the throat for convergent nozzles. When the exhaust nozzle area is reduced by 1% in all reheat ratings, the main burner fuel flow rate and thrust is increased, as presented in the Fig. 17. The increased fuel flow rate leads to a higher combustor exit temperature, which requires higher N2 RPM to satisfy mass balance at the HPT. The N2-corrected RPM increase is seen in Fig. 18.

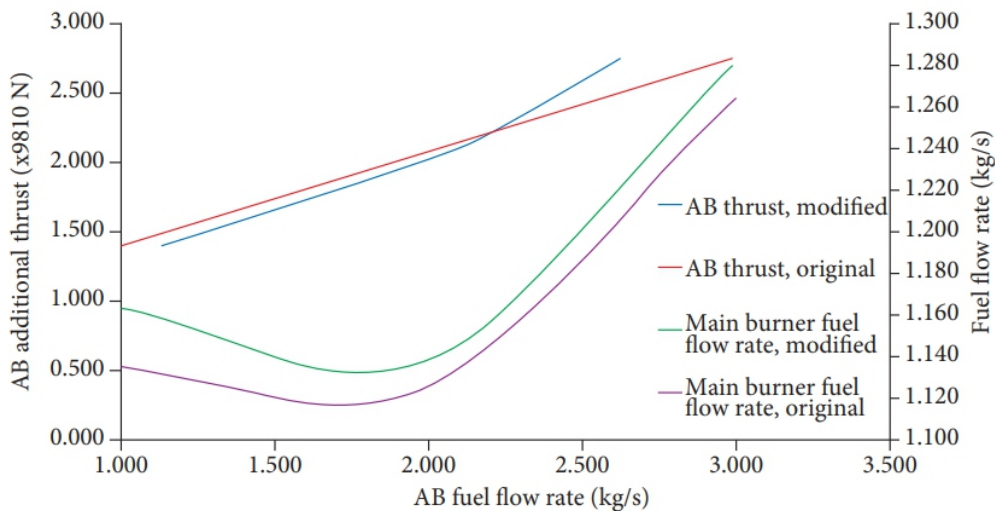**Figure 17.** Thrust and main burner fuel flow rate variation with AB fuel flow rate when default and modified area schedules are used.
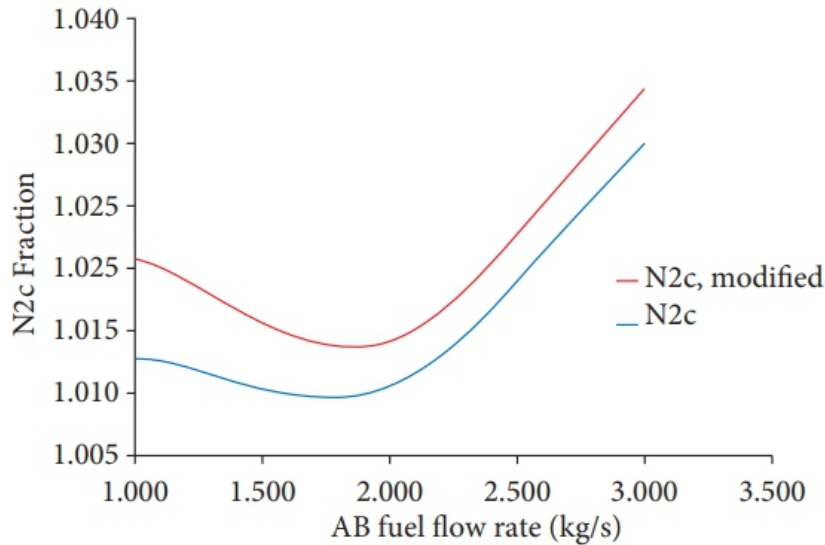
Figure 18. N2c variation with AB fuel flow rate when default and modified area schedules are used.

EFFECT OF CHANGE IN EXHAUST NOZZLE AREA IN A LEAKY ENGINE

The nozzle flaps are provided for varying the exhaust area during reheat operation, and slide over each other during convergence. Due to warping at high temperatures in reheat rating, the nozzle flaps do not seal the flow properly and cause leakage. From simulation using the validated model, it has been calculated that a 1% leakage of air mass flow at full reheat rating in the nozzle flaps causes reduction in thrust (–1.4%), N2-corrected RPM (–0.6%), main burner fuel flow rate (–1.9%), and combustor exit temperature (–1%). As a quick remedy in maintenance station, the exhaust nozzle area is typically reduced to compensate for the reduction of thrust. A proportionate decrease in the exhaust nozzle area brings back the LPT and HPT to their original pressure ratios. Hence, both the compressors return to their original operating points. However, simply maintaining original operating points for both compressors results in a reduced thrust, as the leaked flow does not contribute to momentum thrust from the engine. To get back the original levels of thrust, a minimal increase in fuel flow rate, N2c and combustor exit temperature are required above the healthy engine values. The trend of these increases is similar to that shown in the previous section.

CONCLUSION

Air leakage in the exhaust nozzle flaps of the convergent nozzles is often noticed during the overhaul of legacy turbojets. To correct for the leakage, the exhaust nozzle area is reduced. For quantifying the effect of this leakage and the corrective measures required, it is necessary a validated performance model, which, by its turn, requires compressor characteristics maps for LPC and HPC, not usually provided by the manufacturer. In this work, experimental data from test bed was used to tune the characteristics map

for LPC and HPC, not usually provided by the manufacturer. In this work, experimental data from test bed was used to tune the characteristics map of both compressors, using multipoint scaling methods. Using estimated duct pressure loss values and tuned characteristic maps, an engine specific performance model was developed, applying matrix-based iterative techniques. This model was validated with the original experimental data for design point and off-design ratings, along with reheat ratings. Using this model, the effect of reduction in exhaust area of the convergent nozzle was first analyzed. It was observed that reduction of exhaust nozzle area forces the high pressure spool of the engine to accelerate and go towards the surge. As a linked behavior, the HPT inlet temperature increases, which reduce the life of the hot end components. A reduction of exhaust area is often attempted to compensate for reduced turbine inlet and jet pipe temperatures, due to leaky nozzle flaps. Reducing the nozzle area to get back original design thrust with leaky nozzle flaps increases the turbine inlet temperature beyond design value, and also reduces the surge margin of the HPC. At present, the leakage of hot gases is detected using thermal imaging cameras at the overhaul station. This approach indicates only the presence of leakage and does not quantify it. Actual measurement of the inlet and exhaust mass flow will enable us to calculate the mass flow rate of leakage air and correlate it with experimentally measured thrust decrease. This activity will aid in improving the accuracy of the simulation model, by making possible to estimate the allowable nozzle area change.

AUTHOR'S CONTRIBUTION

Conceptualization, Gouda G and Sankar B; Methodology, Gouda G and Sankar B; Validation, Iyengar V and Soumendu J; Supervision, Iyengar V and Soumendu J; Writing – Original Draft, Sankar B; Writing – Review and Editing, Sankar B.

REFERENCES

Akhmedzjanov AM (2000) Design of aircraft gas turbine engines: Book for higher educational institutions. Moscow: Mashinostroenie, p. 405.

Bechini G (2007) Performance diagnostics and measurement selection for online monitoring of gas turbines (PhD thesis) Cranfield: University Cranfield.

Cohen H, Rogers G, Saravanamuttoo HIH (2001) Gas turbine theory. 5th ed. London: Longman Group Limited. https://doi.org/10.1017/S0001924000066203

Fasching WA, Stricklin R (1982) Summary report for CF6 jet engine diagnostics program. NASA contractor report. NASA CR 165582.

Isaac BD (1992) Engine performance and health monitoring models using steady state and transient prediction methods. AGARD Lecture series 183. North Atlantic Treaty Organization.

Jones SM (2007) An introduction to thermodynamic performance analysis of aircraft gas turbine engine

cycles using the numerical propulsion system simulation code. NASA/TM— 2007-214690.

Kerrebrock JL (1992) Aircraft engines and gas turbines. 2nd ed. Cambridge: MIT Press. ISBN: 9780262111621

Li YG (2002) Performance analysis based gas turbine diagnostics: A review. Proc Inst Mech Eng, Part A216(5). https://doi.org/10.1243/095765002320877856

Li YG, Pilidis P, Newby MA (2006)An adaptation approach for gas turbine design point performance simulation. J Eng Gas Turbines Power 128. doi: https://doi.org/10.1115/1.2136369

Mattingly JD (2006) Elements of propulsion: Gas turbines and rockets. Blacksburg: AIAA Education Series. https://doi.org/10.2514/4.103711

Saravanamuttoo HIH (May 1992) Overview on basis and use of performance prediction methods. AGARD Lecture Series 183. North Atlantic Treaty Organization.

Sankar B, Subramanian T, Shah B, Vanam V, Jana S, Ramamurthy S, Satpathy R, Sahoo B, Yadav S. (2013) Aerothermodynamic modeling and gas path simulation for a twin spool turbo jet engine. Paper presented ASME GT India Conference; Bangalore, India. https://doi.org/10.13140/RG.2.1.1201.8401

Sankar B, Shah B, Ramamurthy S, Satpathy RK, Yadav S (2014) Tuning of component characteristics maps in off-design simulation of gas turbines. Paper presented International Conference on Smart Materials, Structures and Systems; Bangalore, India.

Sankar B, Shah B, Satpathy RK, Gouda G, Jana S (2015) Gas path parameter degradation estimation in a turbojet during long test. Paper presented National Conference On Condition Monitoring (NCCM-2015). Naval Science and Technological Laboratory; Visakhapatnam, India.

Sankar B, Shah B, Jana S, Ramamurthy S, Satpathy RK, Gouda G (2016) Design point parameter estimation of a legacy twin spool turbojet engine for health monitoring. J AeS I68(2):101-109.

Sankar B, Shah B, Iyengar V, Jana S, Gouda G (2017) Water ingestion study in a twin spool turbojet engine. Paper presented National Conference On Condition Monitoring (NCCM-2017). IGCAR; Kalpakkam, India.

Sankar B; Danish TH (2018) Performance trends of a generic small gas turbine engine, Paper presented National Aero Propulsion Conference (NAPC 2018). IIT Kharagpur; West Bengal, India.

Tsoutsanis E (2010) Performance adaptation of gas turbines for power generation applications (PhD thesis). Cranfield: Cranfield University.

Walsh PP, Fletcher P (2004) Gas turbine performance. 2nd ed. Oxford: Blackwell Science. https://doi.org/10.1002/9780470774533

Multidecadal Cycles of the Climatic Index Atlantic Meridional Mode: Sunspots that Affect North and Northeast of Brazil

Cleber Souza Correa1,*, Roberto Lage Guedes1, André Muniz Marinho da Rocha1, Karlmer Abel Bueno Corrêa2

A B S T R A C T

Using the 1951-2017 historical series of the Atlantic Meridional Mode (AMM) index and the monthly number of sunspots, it was possible to observe a significant association between them. The use of wavelet and cross-wavelet analysis showed the presence of multidecadal cycles pronounced in eleven years, as well as cycles of 2.66 and 5.33. AMM index showed, in the part of the Sea Surface Temperature (SST), the presence of a weak signal of 21.33 years. Influence and association of sunspot variability on surface temperature in Northern and Northeastern regions of Brazil were investigated. Using a non parametric statistical correlation test, the historical series of surface temperature anomalies in five locations (Belém, São Luiz, Fortaleza, Fernando de Noronha, and Natal) were compared with the monthly solar-series anomalies. The temperature series used were the minimum monthly average, the monthly average, and maximum monthly average temperatures, with their respective anomalies in relation to the mean. However, among all the series (except for São Luiz), the analyzed minimum temperature anomalies showed a negative correlation with sunspots. As a preliminary result, the analyzed climatic indexes present an apparent degree of memory associated with the variability of sunspot activity.

KEYWORDS: Sunspots, Atlantic Meridional Mode, Multidecadal cycles.

INTRODUCTION

This work focuses on analyzing the temporal sunspot series and the AMM SST index information, in order to observe similar cycles between time series, since there is a gap between the influences of solar activity on terrestrial systems, such as in atmospheric and oceanic dynamics. This is associated with an interhemispheric gradient of anomalous SST, in which part of the dominant frequencies of turbulent processes is known at different associated timescales, varying from monthly, annual and multidecadal. It can, however, also be influenced by teleconnection processes between the planetary regions (e. g., the dynamics of the El NiñoSouthern Oscillation [ENSO] circulation).

In Corrêa et al. (2019), using wavelet and cross-wavelet analysis, multidecadal cycles were observed between the monthly number of spots and the Southern Oscillation Index (SOI) and Pacific Decadal Oscillation (DOP) indexes, showing cycles of 2.66, 5.33, 10.66 and 21.33 years. It was also compared to the average monthly rainfall in the meteorological stations of the airports of Belém, Fortaleza, São Luiz, and Natal, showing that, in North/Northeast of Brazil, the multidecadal cycles of precipitation accompanied the variability of the sunspots.

Prestes et al. (2018) showed that the araucaria tree responds to solar activity, variability, and climate in Southern Brazil. Using wavelet analysis, the researchers found periodicities in the rings of araucaria trees growth, associated with the SOI, as well as with an anomaly of the average annual temperature, between 24 and 44 ºC. It was also observed that there were periods of 2 to 7 years, possibly related to the ENSO phenomenon, and a second period, which lasted for approximately 23 years and was related to temperature variation.

Cliver (2015) discusses the cycles of solar activity and the 22-year magnetic cycle of the Sun, in which there are two characteristic migrations in the behavior of sunspots: the movement towards the solar equator and the movement towards the poles of prominence at high latitudes. The motion of spots towards the equator are defined aspects associated with Schwabe's eleven-year cycles (Schwabe 1843; Wilson 1998) and the second is associated with the 22-year magnetic cycles, otherwise known as Hale's solar cycle (22 years) (Hale and Nicholsen 1925; Babcock 1961; Echer et al. 2003).

Lassen and Friis-Christensen (1995) showed that the duration of a solar cycle in the last five centuries was associated with Earth's climate, having a well-defined activity with an eleven-year cycle in the sunspots number. Solar activity data have been used as parameters for studies addressing physical conditions variability of the high Earth atmosphere. Solar activity can vary in time, with cycles of eleven years. In addition, the duration of sunspots periods is also not fixed, varying between 80 and 90 years. Strong correlations have been observed between these changes and the long-term variations in global temperature.

There are studies that make the association between solar variability and Earth climate (Cliver et al. 1998; Reid 2000; Love et al. 2011; Wang et al. 2018), in which solar activity, such as the average number of annual sunspots and the mean global SST, and the average global temperature are associated. The changes related to the intensity of solar activity on planet Earth's temperature, and because it has different surfaces (continental and oceanic), create a global circulation, associated with the dynamic processes between continents and the oceanic surfaces. The global circulation creates turbulent dynamical structures with different associated time scales. In this regard, planetary atmospheric circulation can define (persistent) teleconnection processes, which influence, for example, the increase in the surface temperature of the Pacific Ocean that affects the meteorological circulations in different parts of the planet.

In South America, meteorological dynamics are directly influenced by the circulations occurring in both the Pacific and the Atlantic Oceans. In the Pacific, the main feature of circulation, on a global scale, is a vertical movement along the equator (west–east), defined as the Walker circulation, associated with ENSO events, which causes changes on a planetary scale. Another planetary circulation structure that extends from the equator to the latitudes of approximately 30 degrees in both hemispheres is Hadley circulation. These two planetary circulations act together, creating a complex structure. When there are

lower temperatures, below the climatological average, on North Atlantic Ocean, near the Caribbean, at the Brazilian coast there are higher average temperatures on the sea and excessive rainfall at Brazilian Northeast, with the intensification of the Intertropical Convergence Zone (ITCZ). This situation is known as the Atlantic temperature gradient, associated with Hadley circulation. SST in Equatorial Atlantic is subject to interannual variability that has impacts on the surrounding continents. (Lübbecke et al. 2018; Dippe et al.2018; Scaife et al. 2018).

The results show that these equatorial surface anomalies are responsible for the seasonal migration to the North of the ITCZ in early summer in Brazilian North and Northeast. Ferreira and Mello (2005) showed that the atmospheric circulation over the tropical region is strongly modulated and modified by thermodynamic patterns on Pacific and Atlantic basins. Thus, in the years when anomalies of positive or negative SST occur in the basins of these oceans, the Hadley cell, which acts southward (ascending branch in the tropics and descendant branches in the middle latitudes), and the Walker cell, zonal (ascending branch in the Western Pacific and descending branch in the Eastern Pacific), are disturbed, causing strong anomalies in the atmospheric circulation on the tropics. Consequently, these cells are displaced from their climatological positions.

A work by and Kossin (2007) showed the possible association between that AMM Index and hurricane activity, the dynamical "mode" of variability intrinsic to the tropical coupled ocean–atmosphere system, is strongly related to seasonal hurricane activity on both decadal and interannual timescales For the tropical Atlantic region, an index was created that represents this variability of the Atlantic temperature gradient: AMM SST index data were obtained from National Oceanic and Atmospheric Administration (NOAA; NOAA Earth System Research Laboratory – Physical Sciences Division; https://www.esrl.noaa.gov/psd/data/timeseries/monthly/AMM/), (Chiang and Vimont 2004; Kossin and Vimont 2007; Vimont and Kossin 2007).

This AMM SST index, to the tropical Atlantic region, allows performing cross-wavelet and wavelet analyzes to correlate it with the sunspot activity and analyzing multidecadal cycles in the respective series. As the historical AMM index series, it is a measure of the dynamic behavior associated with the interhemispheric gradient of the SST anomaly, which occurs over the tropical Atlantic Ocean region, between Brazilian Northeast/North and the coast of Africa. This work aims to analyze the variability of sunspots and their association to AMM Index, as well as to investigate the existence of multidecadal variabilities and their influence on the surface temperatures in Brazilian North and Northeast.

METHODOLOGY

DATAANALYZED
Monthly Climate Time series

AMM SST Index data is defined via applying Maximum Covariance Analysis (MCA) to SST and the zonal and meridional components of the 10 m wind field over the time period of 1950 to 2005, from the National Centers for Environmental Prediction (NCEP)/National Center for Atmospheric Research (NCAR) Reanalysis. To define the spatial pattern, it is needed to also define the over the region (21S-32N, 74W-15E), and spatially smooth it (three longitude by two latitude points). The seasonal cycle is removed, data are detrended, a three-month running mean is applied to the data, and the linear fit to the Cold Tongue Index (CTI), a measure of El Niño Southern Oscillation (ENSO) variability (Zhang et al. 1997), is subtracted from each spatial point. Spatial patterns are defined as the first left (SST) and right (winds) maps resulting from the singular value decomposition of the covariance matrix between the two fields. AMM time series is calculated by projecting SST or the 10 m wind field (detrended, CTI removed, but no 3-month running mean) onto the spatial structure resulting from MCA. Significant monthly average data on the sunspots number (SN) were obtained at http://www.sidc.be/silso/datafiles (data from the Sunspot of the World Data Center [Sunspot Index and Long-term Solar Observations; SILSO], Royal Observatory of Belgium, Brussels), transferring the data file SN_m_tot_V2.csv with information from 1749 to 2018, with a 267 years series. The analyses of the time series were performed using the information obtained in the two aforementioned sources.

Wavelet Analysis

The WaveletComp is an R package used for analysis based on uni- and bivariate time series wavelets. Its 1.0 version (R Foundation for Statistical Computing) (Roesch and Schmidbauer 2014), applies frequency analysis of uni- and bivariate time series using Morlet et al. (1982a, 1982b; Goupillaud et al.1984), as well as the biwavelet package by Grinsted et al. (2004). Morlet wavelet, in the version implemented in WaveletComp, is defined as the convolution of the series with a set of "daughters wavelet" generated by the "mother wavelet", using time translation by τ and defining the scale by s. The position of the daughter wavelet in the time domain is determined by the location of the time parameter τ being displaced by dt, a time increment. WaveletComp rectifies the wavelet power spectrum (cross-wavelet) according to Liu et al. (2007), in the univariate case, and Veleda et al. (2012), in the bivariate case, to avoid "biased" results in filtering and estimating the associated high frequencies or in the sense of variability estimates with short periods in time series. The analyzed phenomena and the time series would tend to be underestimated by conventional approaches. Implemented options for smoothing in a period of time and/or a direction are necessary to perform the calculation with the coherence wavelets methodology, with their multiples (Liu, 1994). The set choice of scales s determines the series wavelet coverage in the frequency domain.

Surface Weather Data

The monthly temperature data were used from five meteorological stations of the Brazilian Air Space

Control Department (DECEA; in Portuguese, Departamento de Controle do Espaço Aéreo) climate database. Minimum, average and maximum monthly mean temperature data were used at the airports of Belém, São Luiz, Fortaleza, Natal, and Fernando de Noronha. The time series were analyzed from January 1951 to September 2017, a period of 67 years. The anomalies were calculated in relation to the observed mean value of each series, in which the anomaly series of the monthly average of sunspots, and the minimum, average and maximum monthly temperatures were generated. ERA5 model reanalysis data is also used to characterize the AMM index modes. This is the reanalysis of the European Center for Medium-Range Weather Forecasts (ECMWF) – ERA5 reanalysis data. This meteorological dataset, ERA5 (Hersbach and Dee 2016), provides estimates of atmospheric parameters (such as air temperature, pressure, wind, humidity, and ozone at different altitudes) and surface parameters (such as rainfall, soil moisture, and sea-surface temperature), all at a resolution of about 31 km worldwide, and information on wave height over the global oceans. More information about the ERA5 model can be found at https://confluence.ecmwf.int//display/CKB/ERA5+data+documentation

Non-parametric Permutation Test

A non-parametric statistical test was used to evaluate the correlation of the time series. The test used employs a statistical permutation (Collingridge 2013; Konietschke and Pauly 2014; Koopman et al. 2015; Zhang et al. 2017; Derrick et al. 2017; Pauly et al. 2018). As a definition, the vectors P, with the monthly values of the series anomaly in relation to their monthly average temperature, and J (N × 1), with the observed monthly average sunspot, intend to make random permutations of J, keeping P fixed. For each permutation, it calculated the correlation between vectors P and J, resampling the series in the order of 10,000 times, thus building the distribution of correlations ®. From these distributions, the test can obtain the value that represents the confidence interval at the level of 5% of the correlations in the upper or lower tails of distribution ® critical). The time series has analyzed 801 values. It used a subroutine program in Matlab©.

The permutation test method is more robust statistically to test the correlation signal between different series that have low correlation values. The correlation between the two series will have a positive upper tail and a negative lower tail, in 10,000 times. Exchanging the same series at random, the probability distribution can be reconstructed in order to analyze the test using a command that orders the randomly calculated correlations. In 10,000 times, the correlation in 500th position and the one in 9,500th position would be critical values at the level of 5%, because, if the original series has a correlation value greater than the value obtained at the 9,500 positions, and/or less than the value in the 500th position, it could not be said that the original correlation is random. The lower critical value of the tail, in the 500th position, was estimated by the series of the minimum average monthly temperature anomaly. However, the value of the upper tail, 9,500th position, was estimated by the average maximum monthly

temperature anomaly. It can be concluded that the series must have some degree of significant correlation. There is statistical evidence that the observed correlations are significant and cannot be discarded. If the correlation falls between the critical values, nothing can be said, which characterizes randomness.

RESULTS

Figures 1a and 1b represent the wind intensity in December 2017 (a) (with a positive AMM index value of 6.14 in SST and a negative value of –2.39 in wind) and in June 2018 (b), with a negative value of –6.48 in SST and a positive value of 4.39 in wind. These figures show two modes of the AMM index in antagonistic positions. Such positions have a dynamic implication, affecting the circulation and characterizing the position of the ITCZ, which affects seasonal meteorological behavior in the North and Northeast regions of Brazil. Figure 1a shows a not well-defined position of the ITCZ, and presents a greater intensity of the wind along the Brazilian coast. However, in Fig. 1b (10ºS –15ºS), it is displayed a greater intensity southward, in the center of the Atlantic Ocean, in the Southern hemisphere, and in the coast of Africa. It also presents a greater intensity of the wind southward in the Northern hemisphere, creating a significant gradient, and positioning the ITCZ between the Brazilian Northeast and the African continent, in 5ºN.

Figures 1c and 1d show the mean temperature over the tropical Atlantic Ocean, having in ºC a range with higher temperatures in the environment at 15°N above 24 °C. Figure 1d shows lower average temperatures in the order of 20 to 22 °C at 15°N on the coast of the African continent. In South Atlantic, the temperature in 10ºS is higher, ranging between 22 to 24 ºC and 24 to 26 ºC. Figs. 1e and 1f show the total precipitation. Figure 1e depicts a strip in the coast of Africa at 5°N and 5°S, where low convective
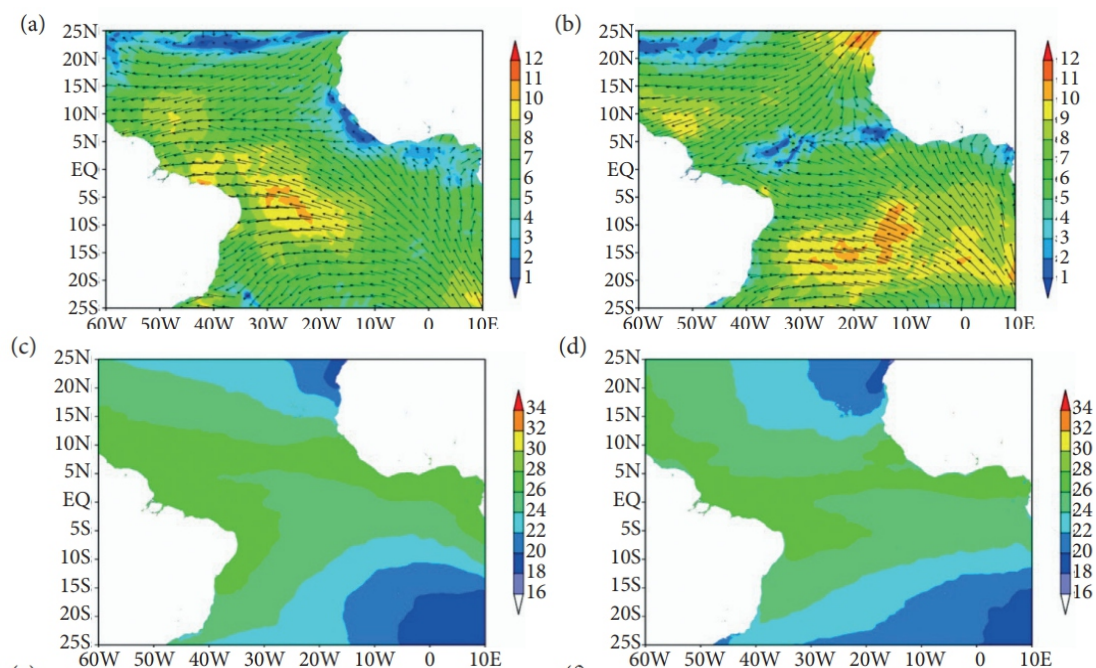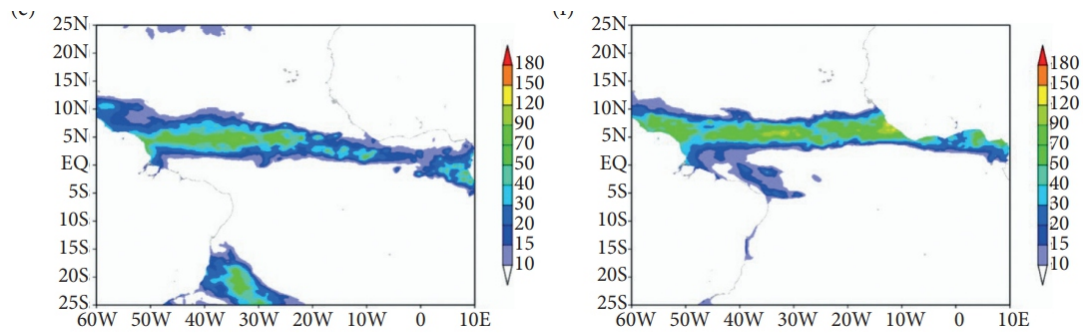
Figure 1. Reanalysis information of the ERA5 model in December 2017 (a, c and e) and June 2018 (b, d and f), where a and b are the monthly wind averages in ms-1. Figures c and d represent the monthly average temperature in °C. Figures e and f are monthly averages of total precipitation in mm.

activity and lower values of total precipitation are seen. Figure 1f shows a well-defined range of precipitation at 5°N, between American and African continents.

The behavior of the AMM Index represents the dynamic interaction between the interhemispheric in the tropical Atlantic Ocean, modulating the displacement of the ITCZ, and showing the coupling between the ocean and the atmosphere with their different temporal scales involved. Figure 2 shows in the series the AMM SST Index, in Fig. 2-A presents cycles with periods of 12 months, 32 months, 64 months and 128 months and a weak signal in 256 months. In Fig. 2-B in sunspot appear 32 months, 64 months and 128 months and 256 months, corresponding to 2.66 years, 5.33 years, 10.66 years, and 21.33 years. In Fig. 2-C in wind appear 32 months, 64 months and 128 months, corresponding to 2.66 years, 5.33 years and 10.66 years. The AMM Index Wind appears predominantly in periods less than 16 months. What the analysis allows to conclude that shows the Wind Field is associated more significantly with shorter time scales of the order of 32 months and less than 16 months, but presents a remarkable signal in 128 months, approximately eleven years.
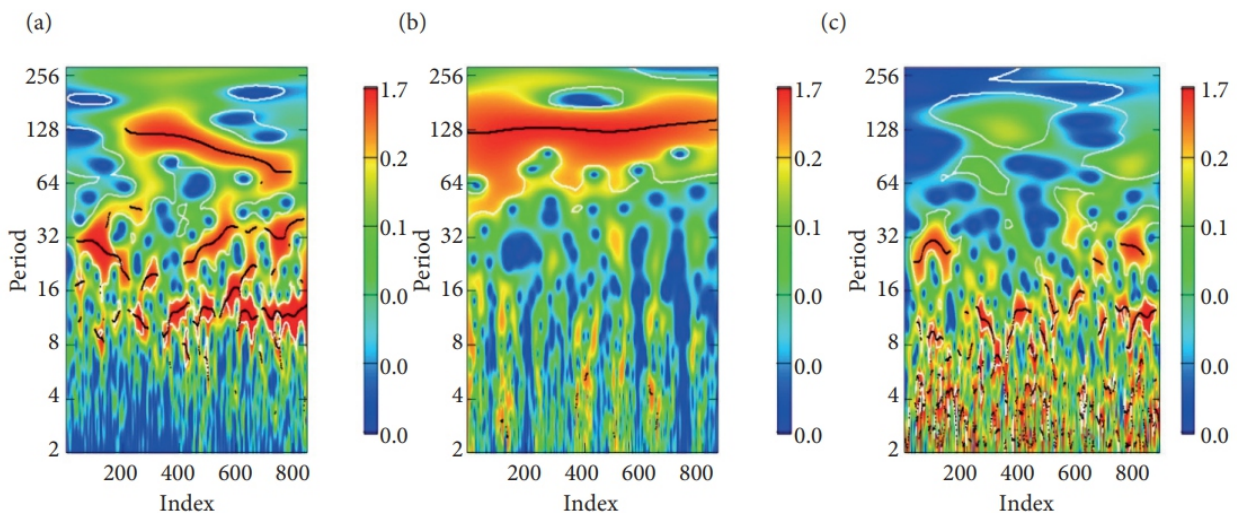

Figure 2. Wavelet analysis of AMM index time series. (a) SST; (b) sunspot; © wind.

The analysis of cross-wavelets in Fig. 3 shows that the 32-months period may be associated with the quasi-periodic oscillations of equatorial zonal wind between the easter- and westerlies, known as the quasi-biennial oscillation (QBO), in the lower stratosphere, and the tropospheric biennial oscillation (TBO), in the troposphere. Both have similar oscillation features (Kwan and Samah 2003; McCormack 2003) and have great eleven years influence in the analysis of cross-wavelet by the AMM index (AMM SST index [a] and AMM wind index [b]). In Figs. 3a and 3c, a significant signal in 21.33 years is seen, which does not appear in the same way in the AMM wind index (b and d), compared to sunspots. Table 1 presents the results of the correlations observed between the series of anomalies in the minimum, average and maximum monthly temperatures and the series of monthly sunspot anomalies. The non-parametric test method is statistically more robust than the classical test method and does not present the problems of statistical inference for its analysis and results.

Table 1 shows that the maximum temperature anomalies are correlated with the sunspot anomalies in Belém, São Luiz, Fortaleza, and Fernando de Noronha. The original correlation value is greater than the one observed in the permutation test. There is statistical evidence, at 5% level, that the series of anomalies are correlated. It cannot be ruled out that the original correlation is not random in the test of 10,000 permutations of the original series. The historical series with the highest correlation observed was in the surface station of São Luiz, said correlation being of 0.18 with the anomalies of the sunspots. However, all series of the analyzed minimum temperature anomalies showed a negative correlation when it was observed the minimum monthly average temperature anomaly, except for São Luiz, characterizing that, when the minimum temperature anomaly occurs, the maximum of the sunspot anomaly did not.
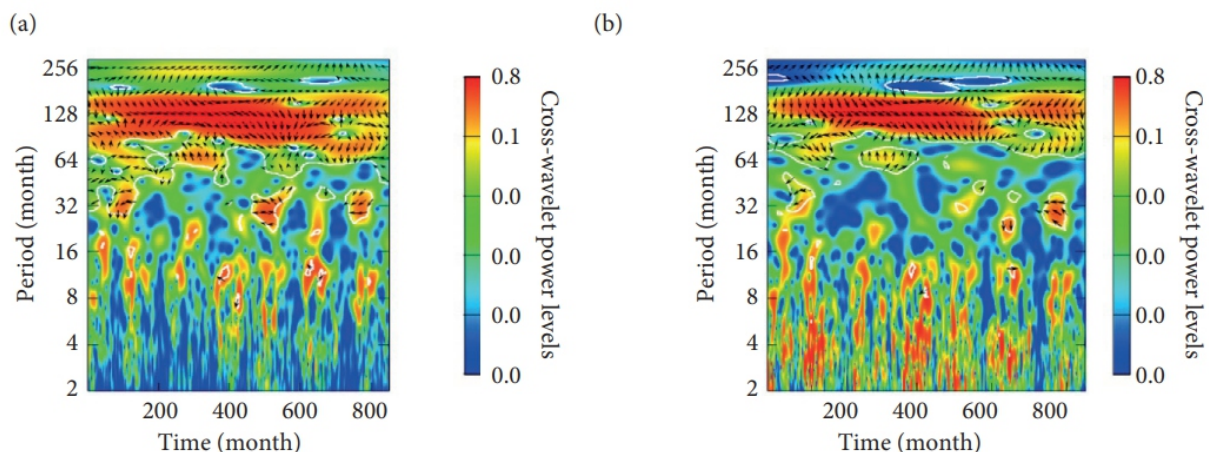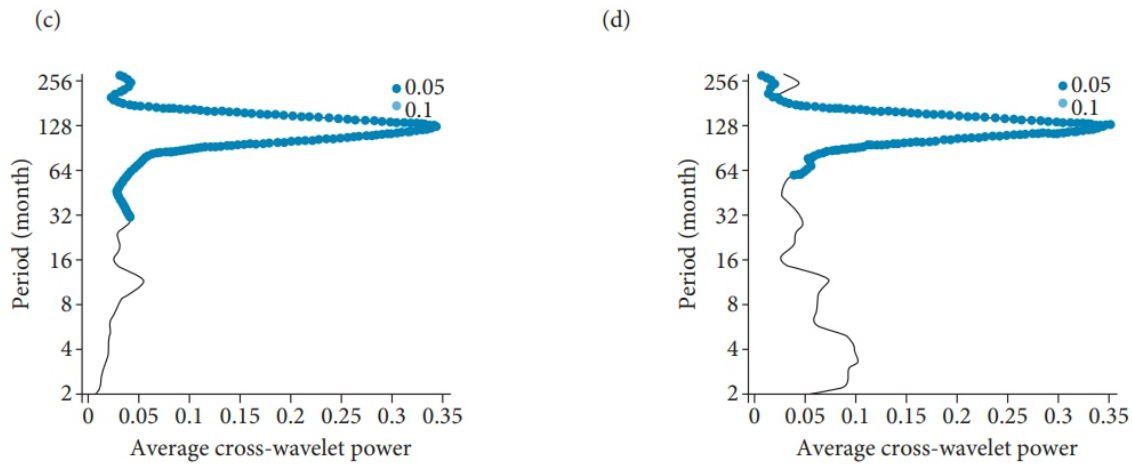
Figure 3. The bivariable energy spectrum with crossed wavelet: (a) AMM – SST and sunspot; (b) AMM – wind and sunspot. It also presents the bivariable cross-wave mean time spectrum: (c) AMM – SST and sunspot; (d) AMM – wind and sunspot.

Table 1. Result of the correlations between temperature anomalies and sunspots with the non-parametric test.

City	Minimum	Mean	Maximum	Non-parametric test	
				Lower tail	Upper tail
Belém	−0.07	0.01	0.09	−0.058	0.059
São Luiz	0.01	0.09	0.18	−0.057	0.058
Fortaleza	−0.05	0.04	0.06	−0.058	0.058
Fernando de Noronha	−0.16	−0.17	0.07	−0.060	0.060
Natal	−0.04	−0.03	0.01	−0.057	0.058

Correlation of temperature/sunspots monthly anomalies

N = 801 values.

Figure 4 shows the distributions of correlations generated by the random permutation process of the original correlation between the series of maximum temperature and sunspot anomaly. The non-parametric correlation test is a statistically robust method, because it showed that, at the 5% level, the original correlations (above the critical value of the 500th position, in the lower tail, and the 9,500th, in the upper tail, in 10,000 permutations) could not be discarded.
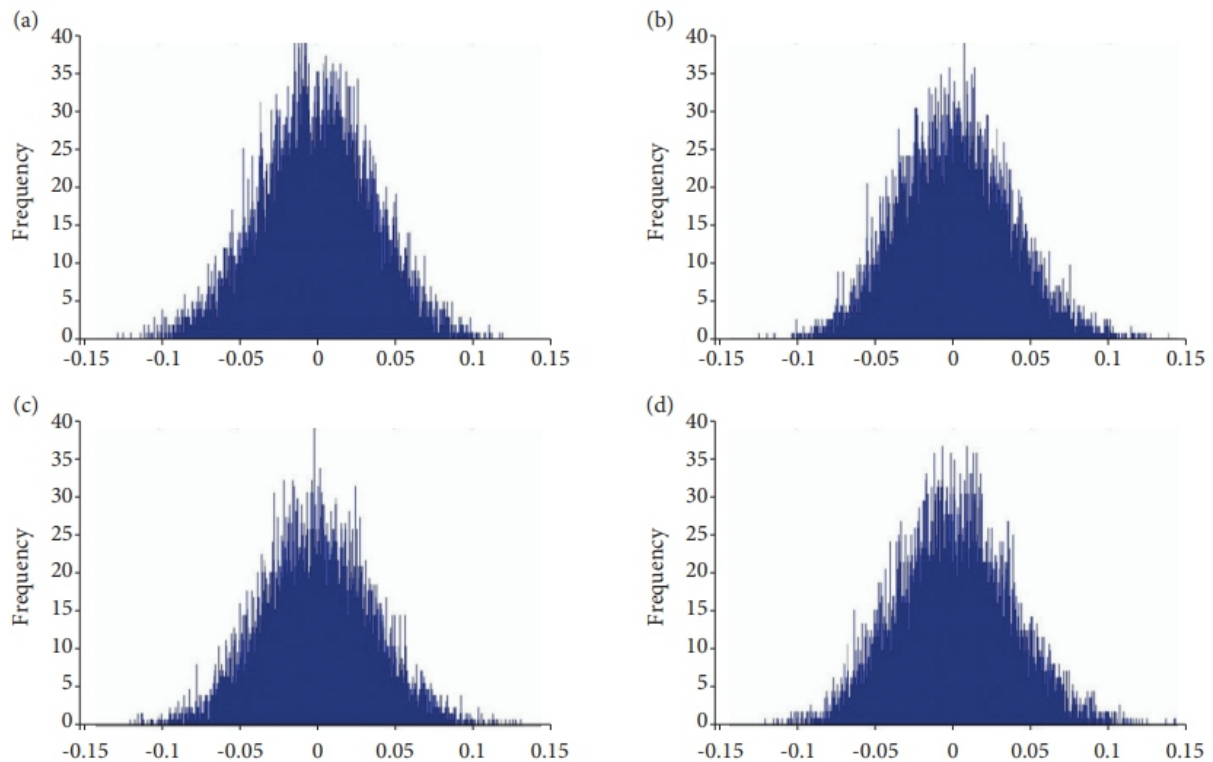
CONCLUSIONS

The AMM index consists of two parts, one associated with the SST and the other to the wind field over the tropical Atlantic region. In this aspect, the results of this work show that an association between the series of the AMM index and the sunspot time series, through the analysis of cross-wavelet, presented the existence of multidecadal cycles. In the SST index series, a well-defined eleven-year signal was found, as well as one of 21.33 years. However, in the wind section of this index, the cycle of 21.33 years did not appear to be significant, showing instead a tendency to represent periods of less than 32 months. It also presented a signal of 128 months (cycle of eleven years).

The solar activity directly affects the terrestrial magnetosphere, creating electrodynamic and hydrodynamic effects in the upper atmosphere by the solar wind (X-rays, high-energy particles, solar plasma, etc) (Kane 2005; Lundin et al. 2007; Yigit et al. 2016). These characteristics act in the stratosphere and the troposphere, affecting the surfaces of the oceans, in the value observed in their SST, and generating circulations with different temporal and spatial scales, with complex and turbulent processes. The solar activities characterize persistent cycles, with dominant frequencies, affecting significantly the terrestrial surface, and the atmosphere/ocean coupling, which reflects in planetary level, with a certain degree of memory. Therefore, the analyzes of minimum, average, and maximum temperatures in five locations of Brazilian North and Northeast showed that they accompany, with some degree of synchronism, and are correlated to the positive anomalies of the sunspots, with the maximum surface temperature (Belém, São Luiz, Fortaleza, and Fernando de Noronha). The non-parametric test

of correlation was able to show a certain degree of association between the historical series observed (1951 to 2017). This work shows a new possibility for future studies with high troposphere and stratosphere data analysis that characterize solar wind activity, associated with the multidecadal cycles of solar activity

AUTHOR'S CONTRIBUTION

Conceptualization, Correa CS; Guedes RL and Corrêa KAB; Formal analysis, Correa CS; Guedes RL; da Rocha AMM and Corrêa KAB; Supervision, Correa CS; Guedes RL; da Rocha AMM and Corrêa KAB; Writing – Original Draft, Correa CS; da Rocha AMM and Corrêa KAB; Writing – Review & Editing, Correa CS and Corrêa KAB.

REFERENCES

Babcock HW (1961) The topology of the Sun's magnetic field and the 22-year cycle. Astrophys J 133:572-587. https://doi.org/10.1086/147060

Chiang JCH, Vimont DJ (2004) Analogous meridional modes of atmosphere ocean variability in the tropical Pacific and tropical Atlantic. J Climate 17(21):4143-4158. https://doi.org/10.1175/JCLI4953.1

Cliver EW, Boriakoff V, Feynman J (1998) Solar variability and climate change: Geomagnetic aa index and global surface temperature. Geophys Res Lett 25(7):1035-103. https://doi.org/10.1029/98GL00499

Cliver EW (2015) The extended cycle of solar activity and the Sun's 22-year magnetic cycle.In: Balogh A, Hudson H, Petrovay K, von Steiger R, editors. The solar activity cycle. Space Sciences Series of ISSI 53:169-189. Springer, New York, NY. https://doi.org/10.1007/978-1-4939-2584-1_6

Collingridge DS (2013) A primer on quantitized data analysis and permutation testing. J Mix Methods Res 7(1):79-95. https://doi.org/10.1177/1558689812454457

Corrêa CS, Guedes RL, Corrêa KAB, Pilau FG (2019) Multidecadal cycles study in the climate indexes series using wavelet analysis in North/Northeast Brazil. Anuário do Instituto de Geociências – UFRJ 42(1):66-73. https://doi.org/10.11137/2019_1_66_73

Derrick B, Broad A, White P, Toher D (2017) Test statistics for the comparison of means for two samples which include both paired observations and independent observations. J Mod Appl. Stat Methods 16(1):137-157. https://doi.org/10.22237/jmasm/1493597280

Dippe T, Greatbatch RJ, Ding H (2018) On the relationship between Atlantic Niño variability and ocean dynamics. Clim Dyn 51:597-612. https://doi.org/10.1007/s00382-017-3943-z

Echer E; Rigozo NR, Nordemann DJR, Vieira LEA, Prestes A, de Faria HH (2003) Sunspot number, solar activity index. Revista Brasileira de Ensino de Física 25(2):157-163.

Ferreira AG, Mello NGS (2005) Principais sistemas atmosféricos atuantes sobre a Região Nordeste do Brasil e a influência dos oceanos Pacífico e Atlântico no clima da região. *Revista Brasileira de Climatologia*, 1(1):15-28. http://doi.org/10.5380/abclima.v1i1.25215

Goupillaud P, Grossman A, Morlet J (1984) Cycle-octave and related transforms in seismic signal analysis. *Geoexploration* 23:85-102. https://doi.org/10.1016/0016-7142(84)90025-5

Grinsted A, Moore JC, Jevrejeva S (2004) Application of the cross wavelet transform and wavelet coherence to geophysical time series. *Nonlinear Processes Geophys* 11:561-566. https://doi.org/10.5194/npg-11-561-2004

Hale GE, Nicholson SB (1925) The law of sun-spot polarity. *Astrophys J* 62:270-300. https://doi.org/10.1073/pnas.10.1.53

Hersbach H, Dee D (2016) ERA5 reanalysis is in production. *ECMWF Newsl*, 147; [accessed February 15, 2019]. https://www.ecmwf.int/en/newsletter/147/news/era5-reanalysis-production

Kane RP (2005) Sun–Earth relation: Historical development and present status – A brief review. *Adv Space Res* 35(5):866-881. https://doi.org/10.1016/j.asr.2005.03.142

Konietschke F, Pauly M (2014) Bootstrapping and permuting paired t-test type statistics. *Stat Comput* 24(3):283-296. https://doi.org/10.1007/s11222-012-9370-4

Koopman J, Howe M, Hollenbeck JR, Sin HP (2015) Small sample mediation testing: Misplaced confidence in bootstrapped confidence intervals. *J App Psy* 100(1):194-202. https://doi.org/10.1037/a0036635

Kossin JP, Vimont DJ (2007) A more general framework for understanding Atlantic hurricane variability and trends. *Bull Amer Meteor Soc*. https://doi.org/10.1175/BAMS-88-11-1767

Kwan KF, Samah AA (2003) A conceptual model relating the quase-biennial oscillation and the tropospheric biennial oscillation. *Int J Climatol* 23:347-362. https://doi.org/10.1002/joc.876

Lassen K, Friis-Christensen E (1995) Variability of the solar cycle length during the past five centuries and the apparent association with terrestrial climate. *J Atmos Terr Phys* 57(8):835-845. https://doi.org/10.1016/0021-9169(94)00088-6

Liu PC (1994) Wavelet spectrum analysis and ocean wind waves. In: Foufoula-Georgiou E, Kumar P, editors. *Wavelets in Geophysics*. Academic Press, San Diego, 4:151–166. https://doi.org/10.1016/B978-0-08-052087-2.50012-8

Liu Y, Liang XS, Weisberg RH (2007) Rectification of the bias in the wavelet power spectrum. *J Atmos Ocean Technol* 24:2093–2102. https://doi.org/10.1175/2007JTECHO511.1

Love JJ, Mursula K, Tsai VC, Perkins DM (2011) Are secular correlations between sunspots, geomagnetic activity, and global temperature significant? *Geophys Res Lett* 38:L21703. https://doi.org/10.1029/2011GL049380

Lundin R, Lammer H, Ribas I (2007) Planetary magnetic fields and solar forcing: Implications for

atmospheric evolution. *Space Sci Rev* 129:245–278. https://doi.org/10.1007/s11214-007-9176-4

Lübbecke JF, Rodríguez-Fonseca B, Richter I, Martín-Rey M, Losada T, Polo I, Noel S, Keenlyside NS (2018) *Equatorial atlantic variability modes, mechanisms, and global teleconnections. Wiley Interdiscip Rev Clim Change* 9(4):01-18. https://doi.org/10.1002/wcc.527

McCormack JP (2003) *The influence of the 11-year solar cycle on the quasi-biennial oscillation. Geophys Res Lett* 30(22):2162. https://doi.org/10.1029/2003GL018314

Morlet J, Arens G, Fourgeau E, Giard D (1982a) *Wave propagation and sampling theory – Part I: Complex signal and scattering in multilayered media. Geophysics* 47:203-221. https://doi.org/10.1190/1.1441328

Morlet J, Arens G, Fourgeau E, Giard D (1982b) *Wave propagation and sampling theory – Part II: Sampling theory and complex waves. Geophysics* 47:222-236. https://doi.org/10.1190/1.1441329

Pauly M, Umlauft M, Ünlü A (2018) *Resampling-based inference methods for comparing two coefficients alpha. Psychometrika* 83(1):203-222. https://doi.org/10.1007/s11336-017-9601-x

Prestes A, Klausner V, da Silva IR, Ojeda-González A, Lorensi C (2018) *Araucaria growth response to solar and climate variability in South Brazil. Ann Geophys* 36:717–729. https://doi.org/10.5194/angeo-36-717-2018

Reid GC (2000) *Solar variability and the Earth's climate: introduction and overview. Space Sci Rev* 94:1-11. https://doi.org/10.1023/A:1026797127105

Roesch A, Schmidbauer H (2014) *WaveletComp: Computational Wavelet Analysis.* R package version 1.0; [accessed February 22, 2019]. http://www.hs-stat.com/projects/WaveletComp/WaveletComp_guided_tour.pdf

Schwabe M (1843) *Die Sonne. Astron Nachr* 20:283-286. https://doi.org/10.1002/asna.18430201706

Scaife AA et al. (2018) *Tropical rainfall predictions from multiple seasonal forecast systems. Int J Climatol* 1:1-15. https://doi.org/10.1002/joc.5855

Veleda D, Montagne R, Araujo M (2012) *Cross-wavelet bias corrected by normalizing scales. J Atmos Ocean Technol* 29:1401–1408. https://doi.org/10.1175/JTECH-D-11-00140.1

Vimont DJ, Kossin JP (2007) *The Atlantic Meridional Mode and hurricane activity. Geophys Res Lett* 34,L07709. https://doi.org/10.1029/2007GL029683

Wang W, Matthes K, Tian W, Park W, Shangguan M, Ding, A (2018) *Solar impacts on decadal variability of tropopause temperature and lower stratospheric (LS) water vapour: A mechanism through ocean–atmosphere coupling. Clim Dyn.* https://doi.org/10.1007/s00382-018-4464-0

Wilson RM (1998) *A comparison of wolf's reconstructed record of annual sunspot number with Schwabe's observed record of 'clusters of spots' for the interval of 1826–1868. Solar Physics* 182:217–230. https://doi.org/10.1023/A:1005046820210

Yigit E, Knízovab PK, Georgieva K, Ward W (2016) *A review of vertical coupling in the*

atmosphere–ionosphere system: Effects of waves, sudden stratospheric warmings, space weather, and of solar activity. J Atmos Sol-Terr Phys 141:1-12. https://doi.org/10.1016/j.jastp.2016.02.011

Zhang Q, Filippi S, Gretton A, Sejdinovic D (2017) Large-scale kernel methods for independence testing. Statist Comput 27:1-18.https://doi.org/10.1007/s11222-016-9721-7

Zhang Y, Wallace JM, Battisti DS (1997) ENSO-like interdecadal variability: 1900-93. J Clim 10:1004-1020. https://doi.org/10.1175/1520-0442(1997)010<1004:ELIV>2.0.CO;2.

Numerical Simulation of the Boundary Layer Control on the NACA 0015 Airfoil Through Vortex Generators

Douglas da Silva1, Vinicius Malatesta2,*

A B S T R A C T

This paper studies the influence caused by a vortex generator (VG) on a wing section with NACA 0015 airfoil when this generator is located before and after a recirculation bubble caused by the boundary layer detachment. The study was numerically carried out and concentrated under conditions of flow with Rec = 2.38 × 105 and angles of attack AoA = 3 and 6, characterized by the fact that they undergo detachment of the boundary layer before and after the location of the VG, respectively. The use of the generator in AoA = 3 strongly influenced the reduction of the recirculation bubble, leading to a drag reduction of 1.43%. In AoA = 6 with a bubble recirculation, the effect was much lower, with no well-defined formation of longitudinal vortices, resulting in increased drag and lift at 0.33 and 0.35%, respectively.

KEYWORDS: Vortex generator; Boundary layer control; Longitudinal vortices

INTRODUCTION

Currently, there is a great effort in the aeronautical industry focused on developing means to control the flow on the aircraft, seeking to improve its aerodynamic performance with the increase of the lift and maximum reduction of the drag on the structure.

According to Schlichting (1979), in low Reynolds (Re) numbers, curved surfaces are susceptible to the detachment of the boundary layer occurring mainly in curved bodies due to pressure distribution gradients. When this gradient tends to be contrary to the flow direction (i.e. [dp/dx] > 0), the boundary layer encounters resistance to its development, extending to the point where it detaches from the surface, generating a recirculation region (low pressure), which can increase body drag.

Many airfoils operating in Reynolds number as a function of wing chord length Rec < 106 have a separation bubble at angles of attack smaller than the stall angle; just after this bubble, a turbulent boundary layer is observed (Kerho et al. 1993).

The boundary layer represents a large part of the drag of an aircraft, and its separation consists of large loss of energy (Gardarin et al. 2008). One of the solutions found to delay the occurrence of this detachment is the vortex generators (VG), which for Lin (1999) are small fins or airfoils extended in the normal direction to the surface, being arranged with a slope relative to the direction of the flow.

According to Lin et al. (1991), these vortices have a fundamental role in the control of the boundary layer, since they add momentum to the boundary layer, redirecting the high moment of external flow to regions near the surface, causing the boundary layer to overcome the resistance of the adverse pressure gradient, which in turn eliminates or retards the layer detachment point.

There are many geometries and arrangements that can be applied to the VG, from rectangular, triangular, trapezoidal, to more complex geometries. Several geometries have been studied as can be observed in the work of Lin et al. (1991), Ashill et al. (2001, 2005), Tebbiche and Boutoudj (2014), as well as revealed in the patent documents of Wheeler (1981) and Veryan (1950).

According to Manolesos and Voutsinas (2015), the use of VG is one of the simplest and most efficient boundary layer control techniques currently available, moreover, is usually the fastest and cheapest solution to control the flow (Fouatih et al. 2016). These are some of the reasons for the growing number of studies related to VG and their application in other areas besides the aeronautical sector, such as their use in wind turbine blades as observed in recent works by Zhang et al. (2016), Gao et al. (2015), Troldborg et al. (2015).

Another large field of application is particularly the automotive industry. Studies have been conducted primarily with regard to race and high-performance cars as presented by Troldborg et al. (2015), Kuya et al. (2009, 2010) who brought a focus on the use of VG with ground effect. For Booker et al. (2011), competition vehicles are also an example of the application of large-scale VG, which have a dimension much larger than the thickness of the boundary layer described by Katz and Morey (2008), where that aid diverts the wake of the flow away from intakes, ducts and other vehicle parts.

In the present work, the influence of the VG on a wing section with NACA 0015 airfoil at an angle of attack AoA = 3 in number of Reynolds $Re_c = 2.38 \times 10^5$, which, according to Robarge et al. (2004), under these conditions, the boundary layer on the airfoil undergoes a brief detachment over a distance of 0.38c and then reattach at 0.56c from the leading edge. Due to this fact, the VG was placed before this region in an attempt to reduce this phenomenon. The case in AoA = 6 and the ability of the VG to form the longitudinal vortices when the recirculation bubble falls on it is also studied, since in that condition the boundary layer after detachment reattach exactly on the VG position.

TESTS BASED ON NACA 00015 AIRFOIL

The main objective of this work is to study the interference generated by vortex generators in the flow on a wing with NACA 0015 airfoil, mainly emphasizing the variation of pressure, drag and lift due to the presence of VG in $Re_c = 2.38 \times 10^5$ and AoA = 3 and 6. The wing has chord length c = 252.3 mm, being:

$$\mathrm{Re}_c = \frac{\rho V_\infty c}{\mu} \tag{1}$$

where: V∞: flow speed, μ: dynamic viscosity and ρ: specific mass.

The vortex generator was developed and sized for a runoff at $Re_c = 2.38 \times 10^5$ and angle of attack AoA = 3, knowing that under these conditions the boundary layer undergoes a brief detachment over a distance of 0.38c and reattach at 0.56c from the edge of attack, Robarge et al. (2004). The height of the VG was

dimensioned in the same order of magnitude of the thickness of the boundary layer δ0.33c, AoA=3 = 1.1mm at the point where the generator (0.33c) is located.

The geometry is shown in Fig. 1, with the generator surface starting at 0.29c increasing linearly until it reaches VG height (h) = 1.2 mm at 0.33c and decreasing as an arc of circumference, until the distance of 0.336c.
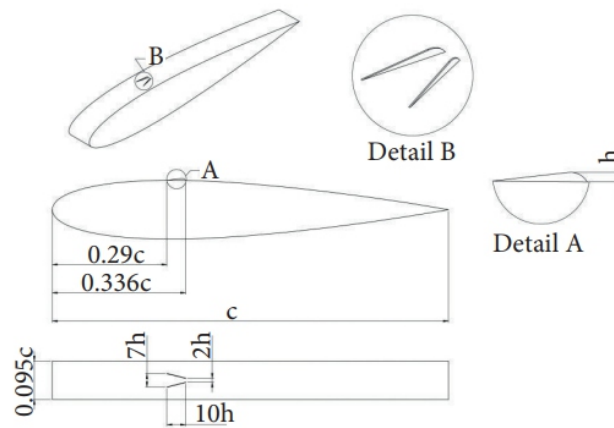

Figure 1. Sizing of vortex generator

NUMERICAL METHOD

The Navier–Stokes equations are solved using the finite element method with Altair HyperWorks CFD trading code, using the turbulence model of a Spalart–Allmaras (SA) equation.

The SA model was chosen because it presents sufficient accuracy to quickly solve the external boundary layer with adverse pressure gradient (Versteeg and Malalasekera 2007), more details about the model can be seen in the work of Spalart and Allmaras (1992).

The computational domain is represented in Fig. 2, the simulation had the studies concentrated in Rec = 2.38 × 105 in AoA = 3 and 6. Figure 2 also shows the boundary conditions used in the simulation, numbered as: Region 1 (symmetry condition), Region 2 (free flow condition, which determine the conditions of the inflow and outflow of the domain), and Region 3 (no-slip condition, on the face representing the surface of the wing)
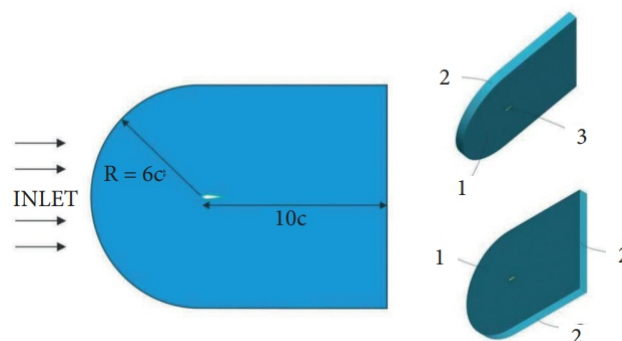
Figure 2. Computational domain and boundary conditions.

The mesh (Fig. 3) used in the boundary layer region contains prismatic volume elements, while the remainder of the domain is composed of tetrahedral volume elements.
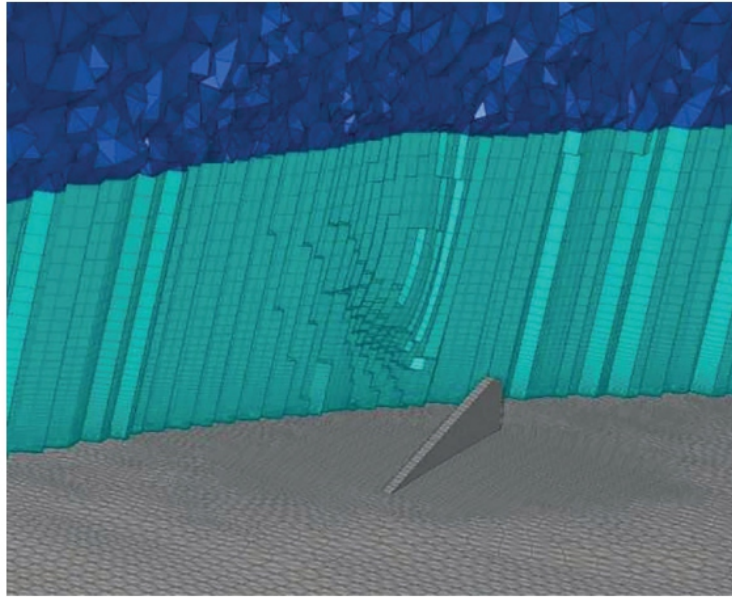

Figure 3. Illustration of the volumetric mesh near the VG.

VALIDATION

The validation of the results was performed with the airfoil without the vortex generator. Firstly, the validation of the code was performed using the wind tunnel data obtained from the work of Sheldahl and Klimas (1981), who performed numerous wind tunnel tests of various airfoil profiles, including NACA 0015 airfoil.

The validation was done with the experimental data in Rec = 3.6 × 105 because it was the experiment found closest to the conditions studied in the present work, for the validation three meshes were created: Mesh 1 = 1.7 × 106, Mesh 2 = 3.1 × 106, Mesh 3 = 5 × 106 elements, presenting good results, as shown in Fig. 4 and Fig. 5. The mesh convergence was performed for all the tests carried out, being chosen the mesh with 5 × 106 elements, due to the good convergence of the results, and a moderate computational cost (Fig. 4).
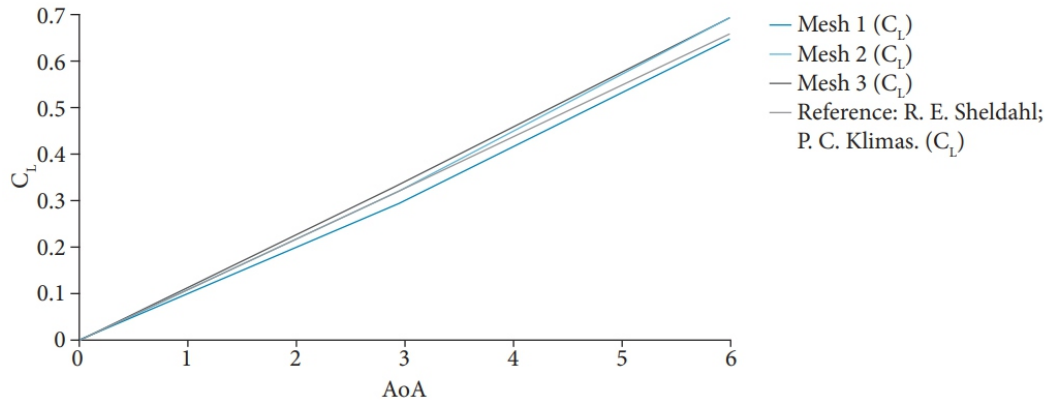
Figure 4. Lift coefficient (CL) as a function of the angle of attack comparing numerical result with the experimental data in wind tunnel.
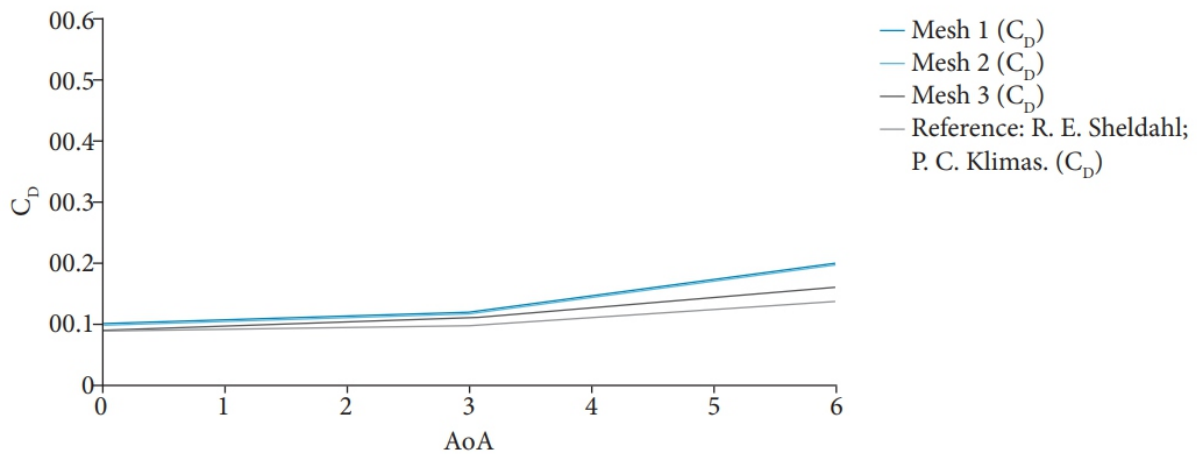
Figure 5. Drag coefficient (CD) as a function of the angle of attack comparing numerical result with the experimental data in wind tunnel.

RESULTS

In $Rec = 2.38 \times 105$ and $AoA = 3$, the emergence of the expected separation bubble was observed, whose detachment of the boundary layer occurs at $\sim 0.34c$ and immediately reattach at $\sim 0.63c$. Figure 6 shows a bluish region (low speed) extending a considerable percentage of the chord, which indicates that the fluid is being braked. According to the enlarged detail presented, it is evident that this is a region of recirculation with velocity vectors opposite to the flow.

When increasing the angle of attack for $AoA = 6$, the recirculation bubble travelling towards the leading edge can be observed, with the boundary layer detachment at $\sim 0.13c$ and reattaching at $\sim 0.33c$. Figure 7 shows the field as well as the recirculation region.
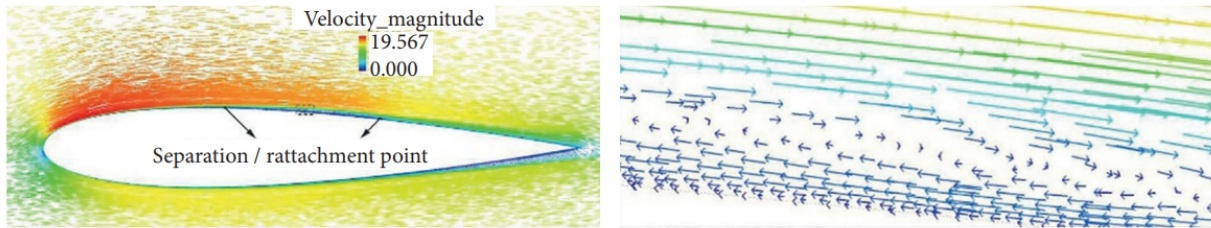
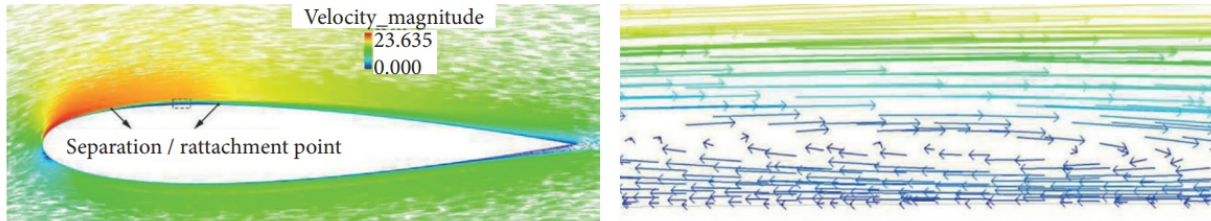**Figure 6.** Profile of the velocity field in *Rec* = 2.38 × 10⁵ and AoA = 3 with extended detail.

Figure 7. Profile of the velocity field in Rec = 2.38 × 105 and AoA = 6 with extended detail.

EFFECT ON THE SPEED PROFILE AND DETACHMENT REGIONS

The study of the influence of the VG on Rec = 2.38 × 105 was carried out based on three plans of measurement (Plan 1, Plan 2 and Plan 3), represented in Fig. 8, where wing width (S) = 24 mm.

Figure 8. Plans of pressure and speed taking.

The occurrence of well-defined counter-rotational longitudinal vortices extending over almost all extrados of the wing was observed in AoA = 3, a strong interaction of these vortices over the recirculation region was observed in the longitudinal region contained near to Plan 3 (Fig. 9).
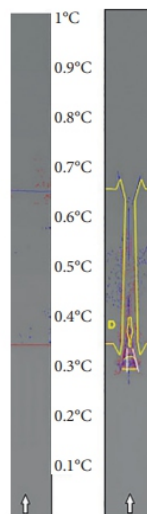
Figure 9. Representation of detachment and reattachment regions over the wing without (left) and with

Figure 9 shows a comparative between the simulation without (left) and with (right) VG, where the red and blue lines are given by the program, representing the considered points of detachment and recollection by the software, respectively. Some random lines that appear do not physically represent the actual regions of detachment and recollection are generated due to some implied numerical error loaded in the model of analysis that estimates these regions. For clearer and representative results, the simulation with VG the regions that were actually considered the region of separation are delimited by a yellow line, this line was stipulated through a careful analysis of the flow based on the velocity vectors. This yellow line makes the interaction of vortices visible by adding kinetic energy and forming a sort of boundary layer aisle attached to the surface, where it was once a single large recirculation bubble.

The numerical analysis showed that the region below the longitudinal vortices location did not show detachment due to the greater amount of kinetic energy injected in the region near the surface in that region. While on the Plan 3 where the vortices meet, there is a strong interaction between them just after the VG inducing the increase of the velocity component in the normal direction of the surface, because the vortices are counter-rotating. This eventually generates a small region of boundary layer detachment and this reattachment increase in the turbulent flow intensity, which added the action of the vortices by throwing the fluid with low kinetic energy out of the boundary layer, making the boundary layer to remain attached to the surface along the rest way (Fig. 10)

The recirculation bubble would decrease considerably near the vortices, as can be seen from Fig. 10 and 14, which show the flow velocity profile along the wing (in comparison with profile without VG, Fig. 11). The vortices are seen more clearly through Fig. 15.
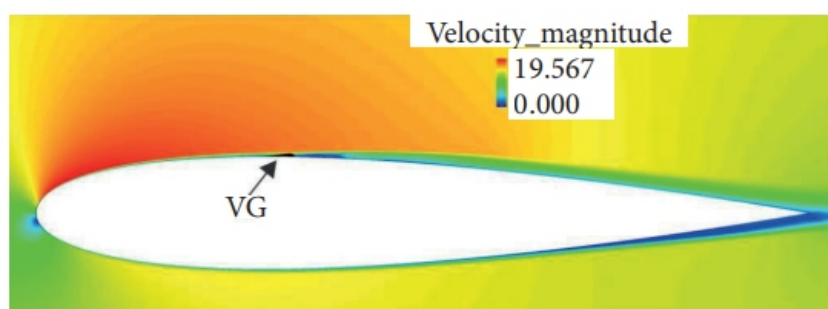

Figure 10. Velocity profile on NACA 0015 airfoil with VG in Plane 3 in Rec = 2.38 × 105 and AoA = 3.
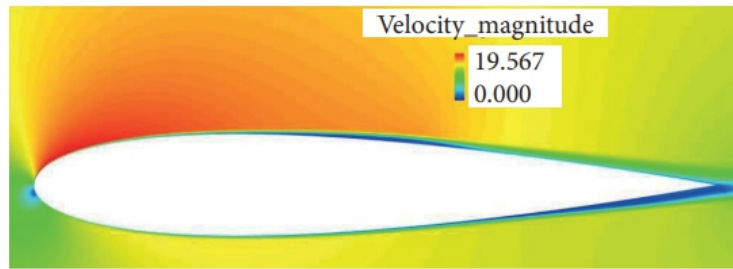
Figure 11. Velocity profile on NACA 0015 airfoil without VG in Plane 3 in $Re_c = 2.38 \times 10^5$ and AoA = 3.
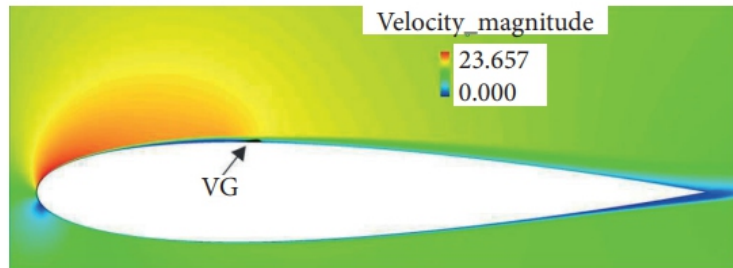

Figure 12. Velocity profile on NACA 0015 airfoil with VG in Plane 3 in $Re_c = 2.38 \times 10^5$ and AoA = 6.
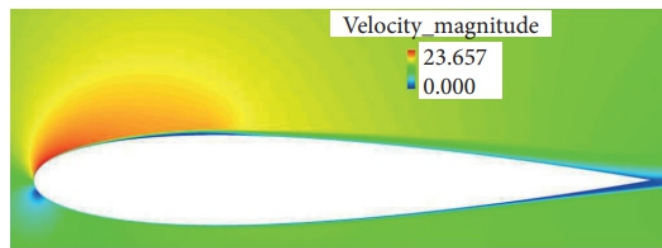

Figure 13. Velocity profile on NACA 0015 airfoil without VG in Plane 3 in $Re_c = 2.38 \times 10^5$ and AoA = 6.
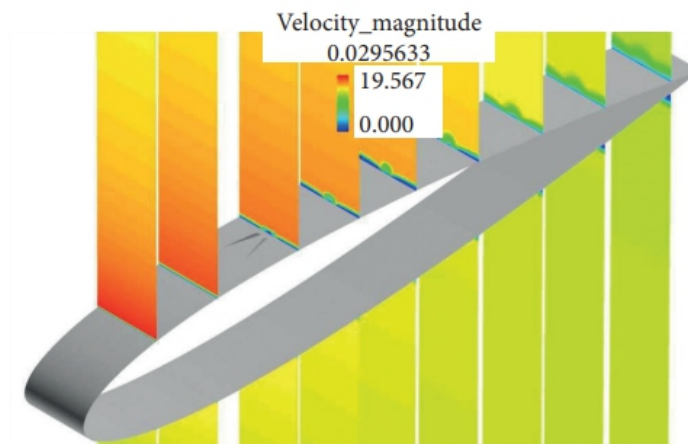

Figure 14. Perspective view of the transverse velocity profiles on the NACA 0015 airfoil with VG in $Re_c = 2.38 \times 10^5$ and AoA = 3.
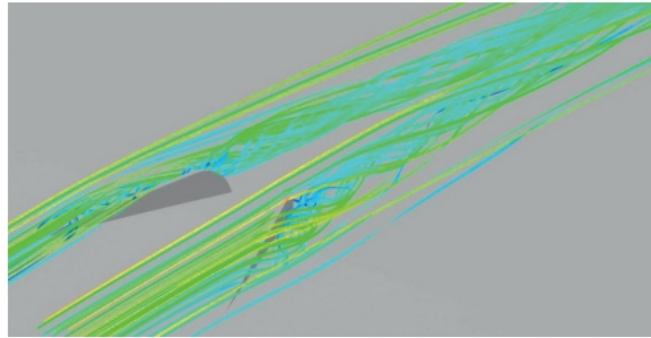
Figure 15. Perspective view of the longitudinal vortices generated by the VG in $Rec = 2.38 \times 10^5$ and AoA = 3.

The simulation in AoA = 6 showed that the recirculation bubble directly falls on the VG, which hinders the generation of vortices since the flow loses energy due to recirculation, this becomes more evident analyzing Figs. 12 and 16 (in comparison with profile without VG in Fig. 13), in which the velocity profiles are presented, in these conditions the emergence of well-defined vortex structures was not observed.
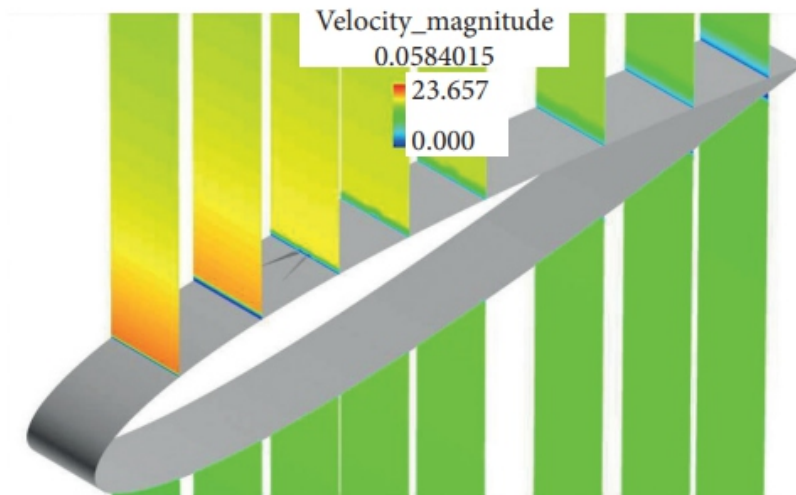

Figure 16. Perspective view of the transverse velocity profiles on the NACA 0015 airfoil with VG in $Rec = 2.38 \times 10^5$ and AoA = 6.

EFFECT ON THE PRESSURE DISTRIBUTION

The performance of the VG can also be observed in Fig. 17, where the pressure distribution is taken in Plans 1, 2 and 3 being compared to NACA 0015 airfoil
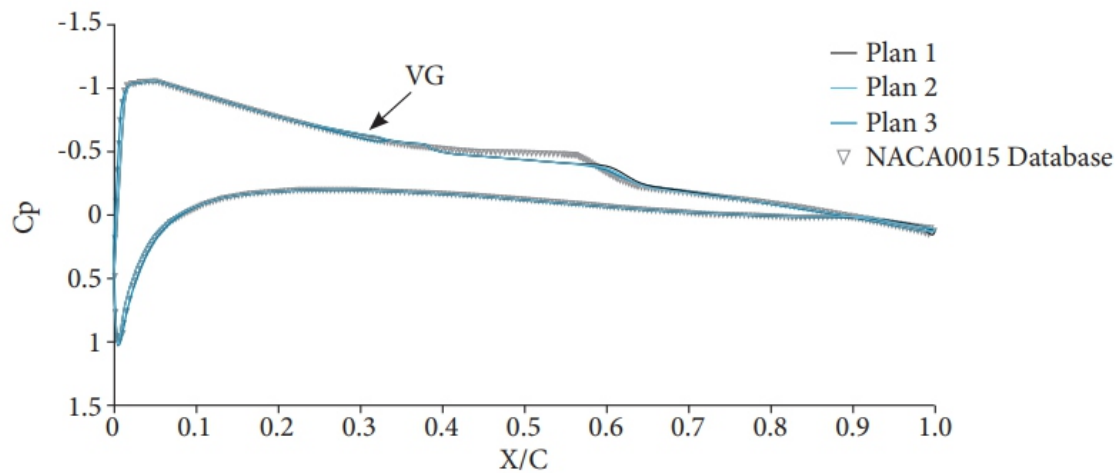

Figure 17. Pressure distribution along Plans 1, 2 and 3 for NACA 0015 airfoil with and without VG in Rec = 2.38 × 105 and AoA = 3.

Without a generator, the generator performance is evident mainly in Plane 3 (between the two surfaces of the VG). When analyzing the region downstream of the VG (after 0.29c), a pressure oscillation is observed first and a step format is identified in 0.38c; this step format indicates a sudden increase in pressure characteristic of reattached region. The reattachment point is followed by a considerable pressure increase between 0.4 and 0.58c, which is due to the fact that the vortices act on the boundary layer by removing the bubble from surface, being this recirculation region characterized by the loss of pressure (low pressure), and when removed, causes the local increase of Cp.

For AoA = 6, it was expected that the VG performance would be lower due to the emergence of the recirculation region before the generator. The pressure as expected was not much affected by the VG. Figure 18 shows that the pressure profiles with and without generator are coincident along almost any length of chord, except for the region near the VG where a slight increase of the pressure between 0.29c to 0.34c (region that contains the VG) can be observed.
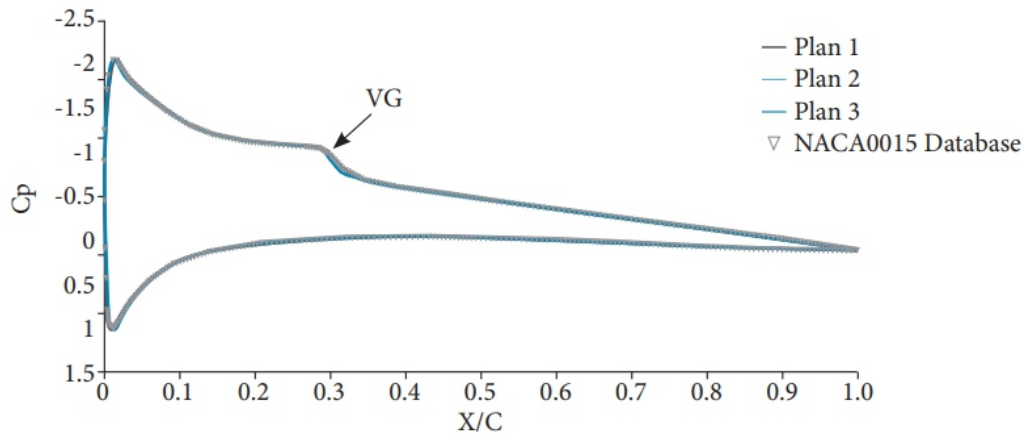
Figure 18. Pressure distribution along Plans 1, 2 and 3 for NACA 0015 airfoil with and without VG in Rec $= 2.38 \times 105$ and AoA $= 6$.

EFFECT ON AERODYNAMICS

The main focus in the study of aerodynamics is mainly the search for ways to increase lift (L) and decrease drag (D). Usually work with L/D ratio to evaluate aerodynamic performance. Table 1 shows that the behavior of the results is in accordance with the expected results. It is possible to analyze that at AoA $= 3$ there was a subtle decrease in the lift of 0.83% due to the increase of the pressure generated by the VG, where in the previous time there was a low-pressure region due to recirculation on the extrados. Another observed point analyzes that at AoA $= 3$ there was a subtle decrease in the lift of 0.83% due to the increase of the pressure generated by the VG, where in the previous time there was a low-pressure region due to recirculation on the extrados. In this case the reduction of drag is due to the action of the longitudinal vortices removing the recirculation bubble in a limited region, resulting in an L/D gain of only 0.61%, but representing improvement of the drag, due to the removal of the detachment zone, a longitudinal portion lying near Plan 3.

Table 1. Comparison between lift and drag between the wing with and without VG

AoA	NACA 0015			NACA 0015 with VG		
–	C_D	C_L	L/D	C_D	C_L	L/D
3	0.013803	0.387694	28.08828	0.013606	0.384489	28.25958
6	0.018377	0.698030	38.06767	0.018397	0.700452	38.07517

Considering the surface of the VG result in the increased of friction drag, due to the increase of the surface wet area, it is possible to observe that the reduction of the recirculation bubble was enough to compensate this drag fraction added, leading to a net drag reduction of 1.43%.

When the wing was observed in AoA $= 6$, it was noticed that the effect of the generator was very small,

due to the region of detachment being located before the VG. In those conditions, the increase of the wet area and the loss of linear moment of the fluid when finding with the fins cause the drag increase to be 0.33%; however, the small increase of 0.35% in the lift due to the new pressure distribution ends up compensating drag, generating the same value of L/D in practice.

ANALYSIS FOR NEW GEOMETRIES

This stage carried out a study character for comparison of the variation of detachment of surfaces and inversion of sense of VG are affect in lift and total drag to a condition of Rec = 2.38 × 105 and AoA = 3, where a bubble of recirculation is present and after VG. The study was performed keeping fixed the height of the VG that worked so far, that is, h = 1.2 mm. In addition, the format and the location of the new VG geometry beginning at 0.29c and ending at 0.33c were also maintained. The simulations were separated into three groups represented in Fig. 19, which was classified in the sequence.
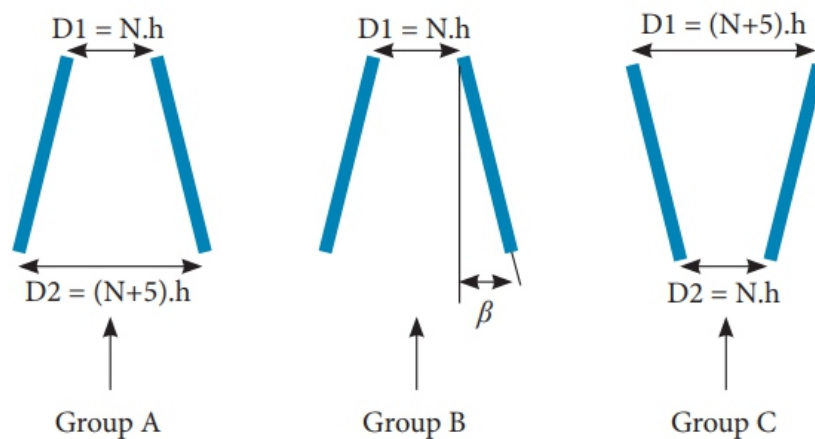

Figure 19. Parameters of VG geometry variation

The basic geometry of the VG that has been studied so far and is described in Fig. 1 was named as VG01 whose value of the β = 14.01o, N = 2, and consequently, D1 = 2 h and D2 = 7 h. It would serve as a base geometry to evaluate the effect of variation of and N.

The parameter N in group A defines proportionally the variation of the smaller (D1) and the greater distance (D2) between the surfaces of the VG, maintaining β = 14o, where N is correlated by D1 = Nh and D2 =(N+5)h. For group B, the value of β was changed, keeping a fixed value of D1 = 2 h. For group C the inverted geometry of VG01 (rotated 180o) was considered. The geometric parameters as well as the nomenclature of the developed geometries are detailed in Table 2

Table 2. Geometric parameters of VG.

Group A			
Geometry	**N**	**D1**	**D2**
VG_{A1}	0	0h	5h
VG_{A2}	4	4h	9h
VG_{A3}	6	6h	11h
Group B			
Geometry	**β**	**D1**	
VG_{B1}	19	2h	
VG_{B2}	24	2h	
Group C			
Geometry	**N**	**D1**	**D2**
VG_{C1}	2	7h	2h
VG main			
Geometry	**N**	**D1**	**D2**
VG_{O1}	2	2h	7h

Table 3 presents the results of the simulation analyzed in group A, where the increase of the drag is observed, as the surfaces move away as N increases, and the geometry of VGA1 is the one that best presents performance with less drag and lift among the other generators. The simulations of Group A indicated that the approximation of surfaces results in improved aerodynamic performance, less drag and more lift, being the best results obtained in N = 0 (VGA1) with the improvement of L/D in 2.56% while the VGA3 did not bring any benefit compared to wing without VG. Group B analysis indicates that the increase in β clearly worsens drag and lift, being VG01 with β = 14o the only geometry that showed better performance in relation to the wing without VG. Group C, in which the geometry VG01 was rotated 180o, resulted in a change in the direction of rotation of the vortices; the results show an evident loss of lift and increase of drag.

Table 3. Comparison of aerodynamic performance due to variation of geometric parameters

Group A				
Geometry	N	C_D	C_L	L/D
without VG	-	0.01380	0.38769	28.088
VG_{01}	2	0.01361	0.38449	28.259
VG_{A1}	0	0.01345	0.38742	28.806
VG_{A2}	4	0.01368	0.38470	28.125
VG_{A3}	6	0.01381	0.38416	27.816
Group B				
Geometry	β	C_D	C_L	L/D
without VG	-	0.01380	0.38769	28.088
VG_{01}	14	0.01361	0.38449	28.259
VG_{B1}	19	0.01397	0.38214	27.345
VG_{B2}	24	0.01424	0.37906	26.612
Group C				
Geometry	N	C_D	C_L	L/D
without VG	-	0.01380	0.38769	28.088
VG_{01}	2	0.01361	0.38449	28.259
VG_{C1}	2	0.01401	0.37573	26.811

CONCLUSIONS

This paper addressed the influence of a vortex generator on a wing with NACA 0015 airfoil at low angles of attack. The study was divided into two cases.

The first case characterized by the occurrence of a separation bubble shortly after the VG showed that the VG performance resulted in a significant decrease of the separation bubble, mainly in the areas near the Plan 3, leading to a small pressure gain that resulted in drag reduction by 1.43%, as well L/D gain of 0.61%.

The second case was interesting to analyze the ability of VG to form vortices when the bubble separates over it, under these conditions no well-defined vortex structures were observed, due to the fact that the recirculation zone decrease part of the linear momentum that would be used to generate the longitudinal vortices. However, even in the face of this fact, a small change in the pressure distribution close to the VG was observed compared to the database, which results in an increase of 0.35%, in contrast to the drag which also increases around 0.33%, almost without influencing the ratio L/D.

The VG is an alternative for the NACA 0015 airfoil at low angle of attack and Rec to lower the detachment region when it is located before detachment. However, for the conditions where this region happens to affect the generator, the use of VG is not strongly justified, but its presence has little influence on the final aerodynamic performance of the wing, since the increase in drag is compensated by the increase in lift.

The results presented showed that the VG is inefficient in generating the vortex structures when it is located inside a recirculation zone, in contrast when situated prior to this recirculation bubble, where it is able to considerably reduce the region of detachment. An analysis was also carried out to evaluate how the changes in some geometric parameters affected wing performance, and the following conclusions were made: drag and wing lift are improved by decreasing distance D1 and D2 (as a function of N) while maintaining $\beta = 14o$, for $\beta > 14o$ drag and lift are harmed, in addition, the rotation by 180o (inversion) of the geometry of the VG worsened drag and lift.

AUTHOR'S CONTRIBUTION Conceptualization, Silva D. and Malatesta V.; Methodology, Silva D. and Malatesta V.; Investigation, Silva D. and Malatesta V.; Writing – Original Draft, Silva D. and Malatesta V.; Writing – Review and Editing, Malatesta V.; Funding Acquisition, Malatesta V.; Resources, Malatesta V.; Supervision, Malatesta V.

REFERENCES

Ashill PR, Fulker JL, Hackett KC (2001) Research at DERA on sub boundary layer vortex generators (SBVGs). In: 39th Aerospace Sciences Meeting and Exhibit. Reno: AIAA. https://doi.org/10.2514/6.2001-887

Ashill PR, Fulker JL, Hackett KC (2005) A review of recent developments in flow control. Aeronaut J. 109(1095):205-232. https://doi.org/10.1017/S0001924000005200

Booker CD, Zhang X, Chernyshenko SI (2011) Large-scale vortex generation modeling. J Fluids Eng. 133(12):121201. https://doi.org/10.1115/1.4005314

Fouatih OM, Madale M, Imine O, Imine B (2016) Design optimization of the aerodynamic passive flow control on NACA 4415 airfoil using vortex generators. Eur J Mech B Fluids. 56:82-96. https://doi.org/10.1016/j.euromechflu.2015.11.006

Gao L, Zhang H, Liu Y, Han S (2015) Effects of vortex generators on a blunt trailing-edge airfoil for wind turbines. Renew Energy. 76:303-311. https://doi.org/10.1016/j.renene.2014.11.043

Gardarin B, Jacquin L, Geffroy P (2008) Flow separation control with vortex generator. In: 4th Flow Control Conference. Seattle: AIAA. https://doi.org/10.2514/6.2008-3773

Katz J, Morey F (2008) Aerodynamics of large-scale vortex generator in ground effect. J Fluids Eng. 130(7):071101. https://doi.org/10.1115/1.2948361

Kerho M, Hutcgerson S, Blacwelder RF, Liebeck RH (1993) Vortex generators used to control laminar separation bubbles. J Aircr. 30(3):315-319. https://doi.org/10.2514/3.46336

Kuya Y, Takeda K, Zhang X (2010) Computational investigation of a race car wing with vortex generators in ground effect. J Fluids Eng. 132(2):021102. https://doi.org/10.1115/1.4000741

Kuya Y, Takeda K, Zhang X, Beeton S, Pandaleon T (2009) Flow physics of a race car wing with vortex generators in ground effect. J Fluids Eng. 131(12):121103. https://doi.org/10.1115/1.4000423

Lin J (1999) Control of turbulent boundary-layer separation using micro-vortex generators. In: 30th Fluid Dynamics Conference. Norfolk: AIAA. https://doi.org/10.2514/6.1999-3404

Lin J, Howard F, Selby G (1991) Exploratory study of vortex-generating devices for turbulent flow separation control. In: 29th Aerospace Sciences Meeting. Reno: AIAA. https://doi.org/10.2514/6.1991-42

Manolesos M, Voutsinas SG (2015) Experimental investigation of the flow past passive vortex generators on an airfoil experiencing threedimensional separation. J Wind Eng Ind Aero. 142:130-148. https://doi.org/10.1016/j.jweia.2015.03.020

Robarge T, Stark A, Mim S-K, Khalatov A, Byerley AR (2004) Design considerations for using indented surface treatments to control boundary layer separation. In: 42nd AIAA Aerospace Sciences Meeting and Exhibit. Reno: AIAA. https://doi.org/10.2514/6.2004-425

Schilichting H (1979) Boundary-layer theory. New York: McGraw-Hill.

Sheldahl RE, Klimas PC (1981) Aerodynamic characteristics of seven symmetrical airfoil sections through 180-degree angle of attack for use in aerodynamic analysis of vertical axis wind turbines. Albuquerque: OSTI.GOV; 1981. Report No.: SAND-80-2114. https://doi.org/10.2172/6548367

Spalart PR, Allmaras SR (1992) A one-equation turbulence model for aerodynamic flows. In: 30th Aerospace Sciences Meeting and Exhibit. Reno: AIAA. https://doi.org/10.2514/6.1992-439

Tebbiche H, Boutoudj MS (2014) Optimized vortex generators in the flow separation control around a NACA 0015 profile. In: Proceedings of the 9th International Conference on Structural Dynamics. Porto: Eurodyn.

Troldborg N, Sørensen NN, Zahle F, Réthoré P-E (2015) Simulation of a MW rotor equipped with vortex generators using CFD and an actuator shape model. In: 53rd AIAA Aerospace Sciences Meeting. Kissimmee: AIAA. https://doi.org/10.2514/6.2015-1035

Versteeg HK, Malalasekera W (2007) An introduction to computational fluid dynamics: the finite volume method. 2nd ed. Edinburgh: Pearson Education.

Veryan SA, inventor. Solid boundary surface for contact with a relatively moving fluid medium. United States patent US 2800291A. 1950.

Wheeler GO, inventor; Cessna Aircraft Co. Means of maintaining attached flow of a flow medium. United States patent US 4455045A. 1981.

Wijdeven TV, Katz J (2013) Simulation of a MW rotor equipped with vortex generators using CFD and an actuator shape model. 53rd AIAA Aerospace Sciences Meeting.

Zhang L, Li X, Yang K, Xue D (2016) Effects of vortex generators on aerodynamic performance of thick wind turbine airfoils. J Wind Eng Ind Aero. 156:84-92. https://doi.org/10.1016/j.jweia.2016.07.013.

Rheological Properties of Composite Polymer Liner Based on Hydroxyl-Terminated Polybutadiene

Igor Sapozhnikov1, Victor Chernov2,*

A B S T R A C T

An experimental study to determine the dependence of the viscosity and shear stress of hydroxyl-terminated polybutadiene (HTPB) and dimeryl diisocyanate (DII) liner on curing time is presented. Viscosity and shear-stress were measured by HAAKE RheoStress 600 rheometer with parallel disks configuration at a constant temperature of 65 °C. The viscosity and shear-stress change were monitored for 8 h. Analysis of data showed that the liner viscosity and shear-stress dependency on time matched to pseudoplastic fluid model. For low shear-rates, the viscosity build-up is highest, with the logarithm of the viscosity being practically linear with time and the viscosity increases by more than two orders of magnitude for these cases. When the shear rates increase, the viscosity build-up slows down considerably with time and the viscosity is increased only by one order of magnitude.

KEYWORDS: Solid rocket motor; Shear-thinning; Curing.

INTRODUCTION

Liner for solid propellants is an elastomeric adhesive, improving mechanical properties between the insulation and the propellant (Quagliano et al. 2015). The common hydroxyl-terminated polybutadiene (HTPB) based liner is a composite matrix that consists mainly of filler powder, HTPB and various additives that determine the rheological and mechanical properties. This is a common technique that is used in many composite materials (Keller et al. 2017; Keller et al. 2018).

During the liner preparation, an isocyanate type curing agent is added to the slurry, which reacts with hydroxyl groups on the HTPB binder forming polyurethane bonds. In the hydroxyl-terminated polybutadiene dimeryl-diisocyanate (HTPB-DDI) binder, the NCO/OH ratio of 0.9–1.3 is used. Liner viscosity is increased until fully cured. The rate of viscosity buildup and the time needed for a fully cured liner may not be correctly predicted and depends on the curing agent properties and characteristics (Randall and Lee 2003).

Hydroxyl-terminated polybutadiene is cured with various isocyanates (Cunliffe et al. 1985; Coutinho et al. 1986) which differ mainly in their rate of reaction. Aliphatic isocyanates, such as hexamethylene diisocyanate (HDI) and isophorone diisocyanate (IPDI), have a slower rate of cure, compared to toluene diisocyanate (TDI) and methylene diphenyl diisocyanate (MDI), both of which are primary aromatic isocyanates (Sutton and Biblarz 2001).

Temperature has a significant role in liner viscosity buildup, which affects cure rate (Quagliano et al. 2015). Increased temperatures decrease viscosity but increase cure rate which is reflected in higher viscosities; thus, a complex dependence is usually observed. In HTPB-TDI systems the viscosity slowly

decreases for 90 min up to curing temperature of 45 °C. If the temperature increased beyond this value, the viscosity will increase sharply (Bandgar et al. 2003).

The non-Newtonian nature of the composite polymer fluid is characterized by pseudoplastic or shear thinning behavior. The common rheological models for HTBP-based polymer fluids are based on the thermochemical models derived from the reaction kinetics for isothermal curing process (Kenny et al. 1989; Kiuna et al. 2002; Liang and Chandrashekhara 2006; Chai et al. 2016; Stanko and Stommel 2018). Similar models are used to characterize rheological behavior of epoxy composited curing (Geissberger et al. 2017; Russo et al. 2019); Different models can be used to characterize rheological behavior of HTPB-based polymer. The presented approach uses generalized Newtonian fluid (GNF) constitutive equation described by Chhabra (2010) and Natan and Rahimi (2002):

$$\mathbf{T} = \eta\left(\mathbf{\Gamma}\right) \cdot \mathbf{\Gamma} \tag{1}$$

The shear stress tensor T and the non-Newtonian viscosity η are dependent on the shear rate tensor Γ. The GNF equation is generally reduced from its full tensor form to one-dimensional model involving only shear stress. The GNF constitutive equation models steady-shear flows well but does not account for thixotropic behavior. The advantages and limitations of the GNF model are discussed by Bird et al. (1987). The GNF model is most commonly used with the Ostwald–de Waele model, or commonly known as power-law (PL) model:

$$\tau = K \cdot \gamma^{n} \tag{2}$$

where: K is flow consistency constant and θ is the flow behavior constant. As can be noticed from the results, the PL model can be adopted for fluids with time dependency parameters, and the compatible form which takes those into account:

$$\tau\left(\dot{\gamma}, t\right) = K\left(t\right) \cdot \dot{\gamma}^{n(t)} \tag{3}$$

Another widely used model for non-Newtonian fluids is the Herschel–Bulkley (HB) model:

$$\eta\left(\dot{\gamma}\right) = K \cdot \dot{\gamma}^{n-1} + \frac{\tau_{y}}{\dot{\gamma}} \tag{4}$$

The HB model includes a term for the yield stress of the fluid τy. Shear stresses applied to the fluid below their yield shear stress produce no fluid flow and merely result in an elastic deformation of the fluid. The pseudoplastic fluids do not have a yield stress, nevertheless they behave nonlinearly. They flow instantaneously upon application of stress but also display shear thinning behavior. Since having a zero-yield stress, the HB model backslides to GNF model combined with the PL model, both modified for time dependency:

MATERIALS AND METHODS

The preparation of the liner was according to standard procedure. The ingredients used to prepare the liner were HTPB, filler powder and additives. At the final stage, curing agent DDI was added to the slurry liquid. The filler was silica powder. The powder consisted of spherical particles, with d50 = 7 μm. The solids loading by volume was 0.18%. Viscosity was measured using Thermo Scientific HAAKE RheoStress 600 rheometer, with parallel disk configuration and 20 mm disk diameter. The parallel disk is one of few configurations suitable for measuring the shear rate dependent viscosity of non-Newtonian fluids (Cross and Kaye 1987; Macosko 1996). It was chosen due to relative ease of sample loading.

The liner specimen was encapsulated between the two disks and held at a constant temperature of 65 °C during the experiment. Dimeryl diisocyanate has a slow cure rate compared to HTPB-TDI. Therefore, viscosity was measured at hourly intervals with the first measurement was taken an hour after the addition of curing agent. Measurement of shear stress and viscosity conducted at shear rates of 1-100 s-1, which covers the shear rates of the expected application.

RESULTS AND DISCUSSION

The measured shear stress and viscosity data are shown in Fig. 1 and 2 correspondingly. As can be expected from the curing processes, the viscosity increases with time for all shear rates. For low shear stresses, the viscosity increases by three orders of magnitude, and for high shear stresses, the viscosity increases by just one order of magnitude. The chemical reaction between the liner ingredients as the curing agent added to the slurry result in non-Newtonian behavior is manifested only after 3 h. The flow behavior constant given in Table 1 supports that conclusion. Non-Newtonian behavior does not appear for all shear rates, but rather starts at some critical shear rate. With time, the critical shear rate moves to lower values, and towards the end of the experiment the non-Newtonian behavior is exhibited for all the range of the shear rates.
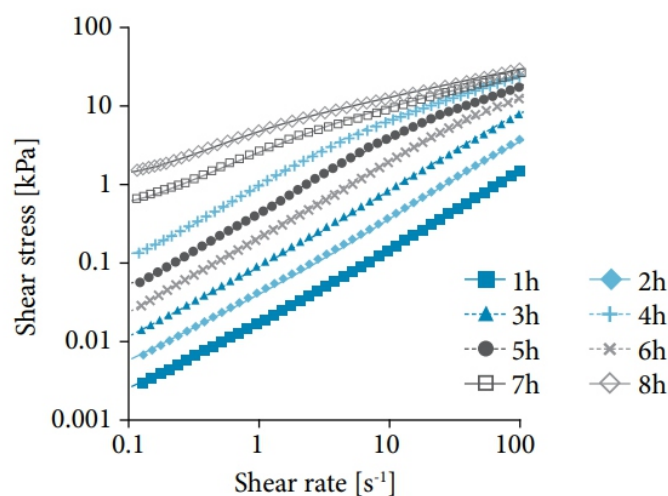

Figure 1. Variation in shear-stress of the liner with shear-rate.

The liner becomes more shear thinning with time. The power-law parameters for each time point are shown in Table 1. It can be seen that the flow behavior constant starts almost Newtonian ($n \approx 1$), but reaches $n = 0.392$ as the liner becomes fully cured. As result, the flow consistency constant is increased by more than two orders of magnitude.

Figure 3 shows a variation of the flow behavior constant n. It can be seen that the time dependence can be divided to three parts. In the first part, for $1\,h \le t \le 3\,h$, the change is mild, and curves are practically flat. The rate of change of n with time at this interval is $n = -0.0272\,h-1$. The second part is between $t = 3\,h$ and $t = 4\,h$, where a sharp decrease in n, for $n3h = 0.94$ to $n4h = 0.76$ occurs. The third part is for $t > 4h$, where there is a linear decrease at the rate $n = -0.09\,h-1$. This is a much sharper decrease rate than in the first interval.
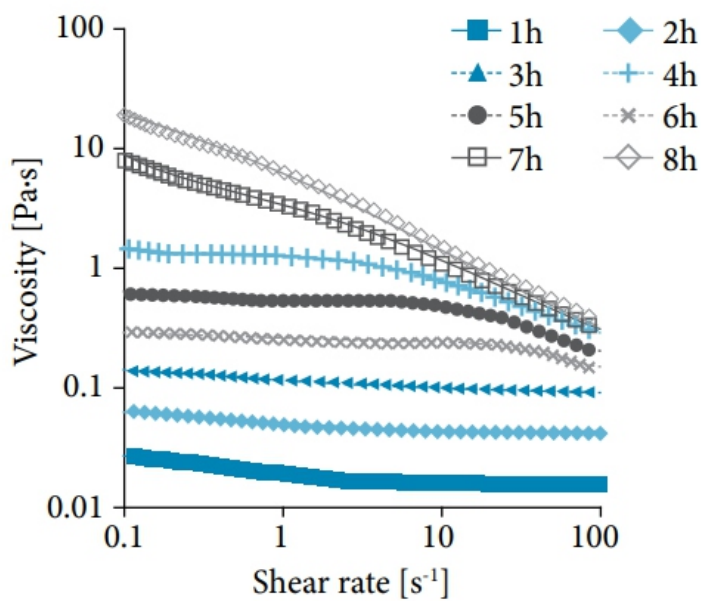

Figure 2. Variation in viscosity of the liner with shear rate.

Table 1. Values of flow consistency and flow behavior constants.

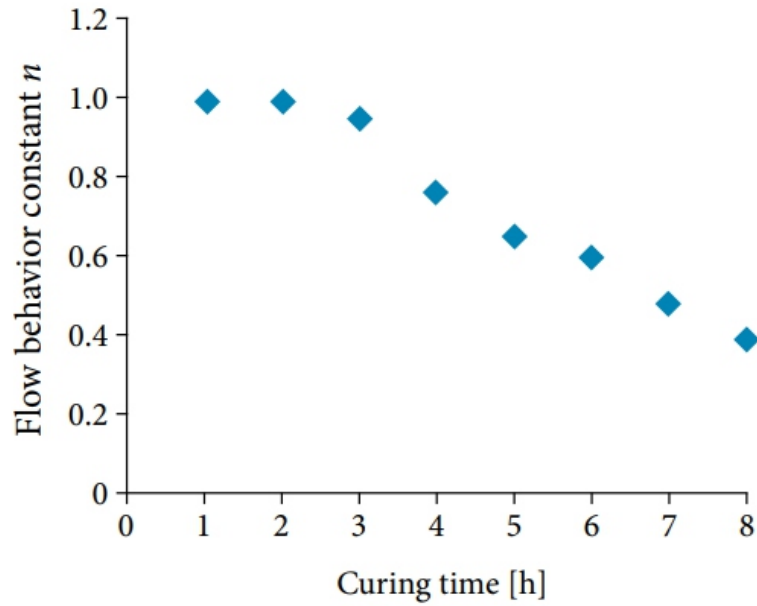| Time [h]	K [Pa·s]	n	R²
1	17	1.00	1.000
2	47	0.98	1.000
3	128	0.94	1.000
4	469	0.76	0.992
5	1094	0.65	0.992
6	1860	0.60	0.997
7	3525	0.48	0.998
8	6010	0.39	0.997

Figure 3. Variation in flow behavior constant of the liner with curing time.
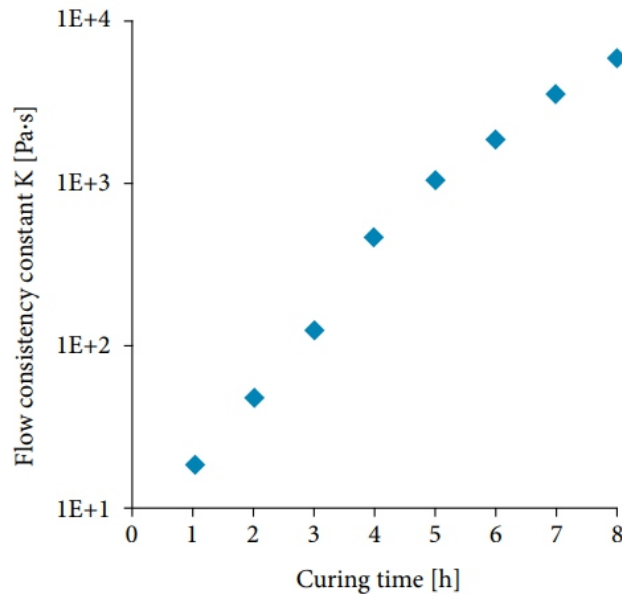
$$K(t) = 0.05356e^{0.5916t} \tag{6}$$

Figure 4. Variation in flow consistency constant of the liner with curing time

Figure 5 shows the time dependence of the viscosity for various shear rates. It can be seen that the viscosity is very sensitive to shear rates after 3 h. A look at the values indicates that for low shear rates a linear relation between log η and curing time can be easily found. For shear rates higher than single digit s-1 this relation becomes more complicated. For shear rates above 50 s-1three staged viscosity rate change is observed. Here we saw condensation of isocyanate groups with OH functionalities decrease

after a certain time. This may be explained by the reactivity of the curing agent, the rate of period and it observed as a decline in viscosity build-up rate.
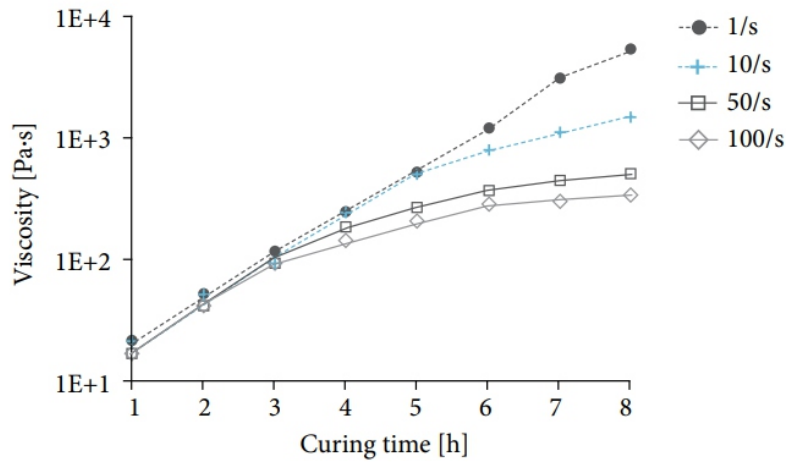

Figure 5. Variation in viscosity of the liner with time.

Elimination of multistage viscosity buildup can be done by increasing the curing temperature, as observed by Sekkar et al. (2002). Single-stage viscosity build-up occurred when the reaction conducted at 70 °C. Under this condition, it was expected that the reactivity difference narrows down to some insignificant level, resulting in the coalescence of stages. Moreover, no multistage process was observed by Sekkar et al. (2002) using hydrogenated diphenylmethane diisocyanate (HMDI) as the curing agent combined with a catalyst. Both DDI and HMDI are aliphatic isocyanates and share some similarities; therefore, the authors of this work, predict that, if the reaction is conducted without any catalyst, viscosity multistage buildup could not be noticed.

CONCLUSIONS

The core of this study was to characterize the rheological behavior of an HTPB based composite liner. A combination of GNF and power-law model provides a good description of the liner rheological behavior.

The time-dependent behavior of the liner is a complex one. At first, it behaves as almost a Newtonian fluid. Only after 3 h, the onset of non-Newtonian behavior is visible. It is also not always a gradual process, the shear-thinning changes rapidly in the beginning, and slower towards the end. The shear rate at which non-Newtonian behavior start to be seen also changes (becomes lower) with time.

Examining time development of the viscosity shows that the process is not uniform. For low shear rates, it can be seen that the viscosity changes gradually with time; however, for higher shear rates, there are two or even three different stages of viscosity buildup. It is clear that viscosity related-predictions of the liner behavior (such as flow rates and shear stresses) must take into account the expected shear rate.

Examining Fig. 2, the initial chosen range of shear rate, 1-100 s-1 for shear stress and viscosity measurements found to satisfy the chosen relations. Increasing the shear rate interval can be incorporated in future work.

Future work will include viscosity measuring in different time intervals, comparison to different measuring technique — cone and plate. Verifying temperature effect on the cure process and comparing between viscosity buildup rate that would be derived.

ACKNOWLEDGMENTS

AUTHOR'S CONTRIBUTION

Conceptualization: Sapozhnikov I.; Data curation: Sapozhnikov I. Formal analysis: Sapozhnikov I. and Chernov V.; Investigation: Sapozhnikov I.; Methodology: Sapozhnikov I. and Chernov V.; Project administration: Chernov V.; Resources: Sapozhnikov I.; Supervision: Chernov V.; Validation: Sapozhnikov I. and Chernov V.; Visualization: Chernov V.; Writing — original draft: Sapozhnikov I.; Writing — review & editing: Chernov V.

REFERENCES

Bandgar BM, Sharma KC, Mukundan T, Krishnamurthy VN (2003) Rheokinetic modeling of HTPB-TDI and HTPB-DOA-TDI systems. J Appl Polym Sci. 89(5):1331-1335. https://doi.org/10.1002/app.12254

Bird RB, Armstrong RC, Hassager O (1987) Dynamics of polymeric liquids. Hoboken: Wiley-Blackwell.

Chai T, Liu YC, Yu YW, Yuan JM, Wang JH, Guo JH (2016) Rheokinetic analysis on the curing process of HTPB-DOA-MDI binder system. IOP Conf Ser: Mater Sci Eng. 137:012069. https://doi.org/10.1088/1757-899X/137/1/012069

Chhabra RP (2010) Non-Newtonian fluids: an introduction. Rheology of complex fluids. New York: Springer. https://doi.org/10.1007/978-1-4419-6494-6_1

Coutinho FMB, Rezende LC, Quijada R (1986) Kinetic study of the reaction between hydroxylated polybutadienes and isocyanates. 1. Reaction with tolylene diisocyanate (TDI). J Polym Sci Pol Chem. 24(4):727-735. https://doi.org/10.1002/pola.1986.080240416

Cross MM, Kaye A (1987) Simple procedures for obtaining viscosity/shear rate data from a parallel disc viscometer. Polymer. 28(3):435-440. https://doi.org/10.1016/0032-3861(87)90196-0

Cunliffe AV, Davis A, Farey M, Wright J (1985) The kinetics of the reaction of isophorone di-isocyanate with mono-alcohols. Polymer. 26(2):301-306. https://doi.org/10.1016/0032-3861(85)90045-X

Geissberger R, Maldonado J, Bahamonde N, Keller A, Dransfeld C, Masania K (2017) Rheological modelling of thermoset composite processing. Compos B Eng. 124:182-189. https://doi.org/10.1016/j.compositesb.2017.05.040

Keller A, Chong HM, Taylor AC, Dransfeld C, Masania K (2017) Core-shell rubber nanoparticle reinforcement and processing of high toughness fast-curing epoxy composites. Compos Sci Technol. 147:78-88. https://doi.org/10.1016/j.compscitech.2017.05.002

Keller A, Dransfeld C, Masania K (2018) Flow and heat transfer during compression resin transfer moulding of highly reactive epoxies. Compos B Eng. 153:167-175. https://doi.org/10.1016/j.compositesb.2018.07.041

Kenny JM, Apicella A, Nicolais L (1989) A model for the thermal and chemorheological behavior of thermosets. I: Processing of epoxy-based composites. Polym Eng Sci. 29(15):973-983. https://doi.org/10.1002/pen.760291502

Kiuna N, Lawrence CJ, Fontana QPV, Lee PD, Selerland T, Spelt PDM (2002) A model for resin viscosity during cure in the resin transfer moulding process. Compos Part A Appl Sci Manuf. 33(11):1497-1503. https://doi.org/10.1016/S1359-835X(02)00177-X

Liang G, Chandrashekhara K (2006) Cure kinetics and rheology characterization of soy-based epoxy resin system. J Appl Polym.102(4):3168-3180. https://doi.org/10.1002/app.24369

Macosko CW (1996) Rheology: principles, measurements and applications. Hoboken: Wiley.

Natan B, Rahimi S (2002) The status of gel propellants in year 2000. Int J Energetic Mater Chem Propul. 5(1-6):172-194. https://doi.org/10.1615/IntJEnergeticMaterialsChemProp.v5.i1-6.200

Quagliano J, Wittemberg V, Gonzalez J, Bacigalupe A (2015) Mechanical and Rheological Properties of Polyurethane Elastomers from Hydroxy-Terminated Polybutadiene and Isophorone Diisocyanate Used as Liners for Composite Propellants. J Res Updates Polym. 4(1):50-55. https://doi.org/10.6000/1929-5995.2015.04.01.6

Randall D, Lee S (2003) The polyurethanes book. Hoboken: Wiley.

Sekkar V, Venkatachalam S, Ninan KN (2002) Rheokinetic studies on the formation of urethane networks based on hydroxyl terminated polybutadiene. Eur Polym J. 38(1):169-178. https://doi.org/10.1016/S0014-3057(01)00106-9

Stanko M, Stommel M (2018) Kinetic prediction of fast curing polyurethane resins by model-free isoconversional methods. Polymers. 10(7):698. https://doi.org/10.3390/polym10070698

Sutton GP, Biblarz O (2001) Rocket propulsion elements. Canada: John Wiley & Sons

Instructions for Authors

Essentials for Publishing in this Journal

1   Submitted articles should not have been previously published or be currently under consideration for publication elsewhere.

2   Conference papers may only be submitted if the paper has been completely re-written (taken to mean more than 50%) and the author has cleared any necessary permission with the copyright owner if it has been previously copyrighted.

3   All our articles are refereed through a double-blind process.

4   All authors must declare they have read and agreed to the content of the submitted article and must sign a declaration correspond to the originality of the article.

Submission Process

All articles for this journal must be submitted using our online submissions system. http://enrichedpub.com/ . Please use the Submit Your Article link in the Author Service area.

Manuscript Guidelines

The instructions to authors about the article preparation for publication in the Manuscripts are submitted online, through the e-Ur (Electronic editing) system, developed by **Enriched Publications Pvt. Ltd**. The article should contain the abstract with keywords, introduction, body, conclusion, references and the summary in English language (without heading and subheading enumeration). The article length should not exceed 16 pages of A4 paper format.

Title

The title should be informative. It is in both Journal's and author's best interest to use terms suitable. For indexing and word search. If there are no such terms in the title, the author is strongly advised to add a subtitle. The title should be given in English as well. The titles precede the abstract and the summary in an appropriate language.

Letterhead Title

The letterhead title is given at a top of each page for easier identification of article copies in an Electronic form in particular. It contains the author's surname and first name initial .article title, journal title and collation (year, volume, and issue, first and last page). The journal and article titles can be given in a shortened form.

Author's Name

Full name(s) of author(s) should be used. It is advisable to give the middle initial. Names are given in their original form.

Contact Details

The postal address or the e-mail address of the author (usually of the first one if there are more Authors) is given in the footnote at the bottom of the first page.

Type of Articles

Classification of articles is a duty of the editorial staff and is of special importance. Referees and the members of the editorial staff, or section editors, can propose a category, but the editor-in-chief has the sole responsibility for their classification. Journal articles are classified as follows:

Scientific articles:

1. Original scientific paper (giving the previously unpublished results of the author's own research based on management methods).

2. Survey paper (giving an original, detailed and critical view of a research problem or an area to which the author has made a contribution visible through his self-citation);

3. Short or preliminary communication (original management paper of full format but of a smaller extent or of a preliminary character);

4. Scientific critique or forum (discussion on a particular scientific topic, based exclusively on management argumentation) and commentaries. Exceptionally, in particular areas, a scientific paper in the Journal can be in a form of a monograph or a critical edition of scientific data (historical, archival, lexicographic, bibliographic, data survey, etc.) which were unknown or hardly accessible for scientific research.

Professional articles:

1. Professional paper (contribution offering experience useful for improvement of professional practice but not necessarily based on scientific methods);

2. Informative contribution (editorial, commentary, etc.);

3. Review (of a book, software, case study, scientific event, etc.)

Language

The article should be in English. The grammar and style of the article should be of good quality. The systematized text should be without abbreviations (except standard ones). All measurements must be in SI units. The sequence of formulae is denoted in Arabic numerals in parentheses on the right-hand side.

Abstract and Summary

An abstract is a concise informative presentation of the article content for fast and accurate Evaluation of its relevance. It is both in the Editorial Office's and the author's best interest for an abstract to contain terms often used for indexing and article search. The abstract describes the purpose of the study and the methods, outlines the findings and state the conclusions. A 100- to 250-Word abstract should be placed between the title and the keywords with the body text to follow. Besides an abstract are advised to have a summary in English, at the end of the article, after the Reference list. The summary should be structured and long up to 1/10 of the article length (it is more extensive than the abstract).

Keywords

Keywords are terms or phrases showing adequately the article content for indexing and search purposes. They should be allocated heaving in mind widely accepted international sources (index, dictionary or thesaurus), such as the Web of Science keyword list for science in general. The higher their usage frequency is the better. Up to 10 keywords immediately follow the abstract and the summary, in respective languages.

Acknowledgements

The name and the number of the project or programmed within which the article was realized is given in a separate note at the bottom of the first page together with the name of the institution which financially supported the project or programmed.

Tables and Illustrations

All the captions should be in the original language as well as in English, together with the texts in illustrations if possible. Tables are typed in the same style as the text and are denoted by numerals at the top. Photographs and drawings, placed appropriately in the text, should be clear, precise and suitable for reproduction. Drawings should be created in Word or Corel.

Citation in the Text

Citation in the text must be uniform. When citing references in the text, use the reference number set in square brackets from the Reference list at the end of the article.

Footnotes

Footnotes are given at the bottom of the page with the text they refer to. They can contain less relevant details, additional explanations or used sources (e.g. scientific material, manuals). They cannot replace the cited literature.

The article should be accompanied with a cover letter with the information about the author(s): surname, middle initial, first name, and citizen personal number, rank, title, e-mail address, and affiliation address, home address including municipality, phone number in the office and at home (or a mobile phone number). The cover letter should state the type of the article and tell which illustrations are original and which are not.